UNIVERSITE DU QUEBEC A MONTREAL

THESE PRESENTEE A L'UNIVERSITE DU QUEBEC A CHICOUTIMI

COMME EXIGENCE PARTIELLE

DU DOCTORAT EN RESSOURCES MINERALES

OFFERT A

L'UNIVERSITE DU QUEBEC A MONTREAL

EN VERTU D'UN PROTOCOLE D'ENTENTE AVEC

L'UNIVERSITE DU QUEBEC A CHICOUTIMI

PAR

EVELISE BOURLON

Analyse des champs de gravité et magnétique dans le Bouclier canadien à l'aide de méthodes traditionnelles et basées sur la transformée en ondelettes

Bibliothèque
Paul-Émile-Boulet

UQAC
Université du Québec
à Chicoutimi

Mise en garde/Advice

Afin de rendre accessible au plus grand nombre le résultat des travaux de recherche menés par ses étudiants gradués et dans l'esprit des règles qui régissent le dépôt et la diffusion des mémoires et thèses produits dans cette Institution, **l'Université du Québec à Chicoutimi (UQAC)** est fière de rendre accessible une version complète et gratuite de cette œuvre.

Motivated by a desire to make the results of its graduate students' research accessible to all, and in accordance with the rules governing the acceptation and diffusion of dissertations and theses in this Institution, the **Université du Québec à Chicoutimi (UQAC)** is proud to make a complete version of this work available at no cost to the reader.

L'auteur conserve néanmoins la propriété du droit d'auteur qui protège ce mémoire ou cette thèse. Ni le mémoire ou la thèse ni des extraits substantiels de ceux-ci ne peuvent être imprimés ou autrement reproduits sans son autorisation.

The author retains ownership of the copyright of this dissertation or thesis. Neither the dissertation or thesis, nor substantial extracts from it, may be printed or otherwise reproduced without the author's permission.

UNIVERSITE DU QUEBEC A MONTREAL

THESE PRESENTEE A L'UNIVERSITE DU QUEBEC A CHICOUTIMI

COMME EXIGENCE PARTIELLE

DU DOCTORAT EN RESSOURCES MINERALES

OFFERT A

L'UNIVERSITE DU QUEBEC A MONTREAL

EN VERTU D'UN PROTOCOLE D'ENTENTE AVEC

L'UNIVERSITE DU QUEBEC A CHICOUTIMI

PAR

EVELISE BOURLON

ANALYSIS OF GRAVITY AND MAGNETIC FIELDS IN THE CANADIAN SHIELD USING STANDARD AND WAVELET-BASED METHODS

Résumé

Cette thèse présente une étude géophysique du Bouclier canadien à l'aide de données gravimétriques et magnétiques. La première partie concerne les méthodes utilisées. Les outils classiques sont introduits ainsi que des méthodes de traitement de données à l'aide de la transformée en ondelettes. Une méthode de caractérisation des sources responsables des anomalies du champ est exposée ainsi qu'une méthode de calcul de l'épaisseur élastique de la lithosphère. La seconde partie de la thèse concerne les applications.

L'étude du prolongement des structures géologiques Protérozoïques de l'orogène Trans-Hudson et Archéennes de la province du Supérieur sous le couvert sédimentaire du bassin de Williston fait l'objet d'un chapitre. Nous avons produit des cartes des champs gravimétrique et magnétique afin d'effectuer une interprétation visuelle des structures géologiques. Les détails ont été réhausser à l'aide de dérivées horizontales des champs. Nous avons étudié les champs à différentes échelles grâce à la transformée en ondellettes. Une carte de la profondeur du socle magnétique a été produite en utilisant la déconvolution d'Euler. Grâce à cette étude, nous avons montré que certaines structures géologiques qui compose l'orogène transhudonien dans le nord du Manitoba et du Saskatchewan se prolongent au moins jusqu'à la frontière américaine et que les sous-provinces du Supérieur se prolongent vers l'ouest sous les sédiments dans le Manitoba. Nous nous sommes intéressé à deux structures tectoniques: une zone de contact entre deux provinces géologiques et une faille majeure. Nous avons déterminé leurs positions et avons caractérisé leurs extensions verticales et leurs pendages.

Le chapitre suivant traite du calcul de l'épaisseur élastique dans l'est du Bouclier canadien. Nous avons calculé cette épaisseur avec une méthode traditionelle. Nous avons montré que la lithosphère au Québec et au Labrador est très rigide. Nous avons développé une méthode utilisant la transformée en ondelettes afin d'étudier l'anisotropie de ce paramètre. Cette méthode a montré que la rigidité est très anisotrope dans la province du Supérieur et beaucoup plus isotrope dans la province de Grenville.

Dans le dernier chapitre, nous présentons l'étude des champs de gravité et magnétique dans la Baie d'Ungava. Ce travail s'inscrit dans le cadre du programme LITHOPROBE ECSOOT (Eastern Canadian Shield Onshore-Offshore Transect). Nous avons établi des cartes de champs de potentiel en compilant des données de différentes origines: données de terrain et satellitaires pour le champ gravimétrique, données aéroportées et marines pour le champ magnétique. L'interprétation de ces

cartes nous a permit de conclure qu'une petite partie de la province du Supérieur se trouvait à l'est de l'orogène du Nouveau-Québec au Labrador et que certaines structures géologiques présentes au Labrador traversent la Baie d'Ungava jusqu'à la Terre de Baffin. Ce chapitre a fait l'objet d'un article publié dans le volume de synthèse du projet ECSOOT dans le Journal Canadien des Sciences de la Terre.

Mots clefs: Bouclier canadien, géophysique, gravimétrie, magnétique, ondelettes, déconvolution d'Euler, Fourier, épaisseur élastique, orogène transhudsonien, province du Supérieur.

Abstract

This thesis presents a geophysical study of the Canadian Shield using gravity and magnetic data. The first part is about the methodology. Standard methods and wavelet-based methods are presented. A method to characterize the causative sources of the field anomalies is described. A wavelet method to compute the elastic thickness of the lithosphere is presented. The second part concerns the applications on geophysical data from the Canadian Shield.

A study of the continuation of the Proterozoic Trans-Hudson orogen and the Archean eastern Superior province features under the sedimentary cover of the Williston basin in Central Canada is the subject of a chapter. We produce maps of gravity and magnetic fields for a visual interpretation of the geological structures. Details were enhanced by the way of horizontal derivatives of fields. We studied fields at different scales with the wavelet transform. A depth to magnetic basement map has been produced using Euler's deconvolution. We have shown that some structures of the Trans-Hudson orogen in northern Manitoba and Saskatchewan extend at least as far south as the U.S. border and that the Superior subprovinces extend westward under the sedimentary cover in Manitoba. We looked at two tectonic structures: a contact between two geological provinces and a major fault. We have determined their positions and we have characterized their vertical extensions and their dips.

The following chapter concerns elastic thickness calculation in eastern Canadian Shield. We calculated this thickness with standard methods and we have shown that the lithosphere in Quebec and Labrador is very strong. We developed a method based on wavelet transform to study the anisotropy of this parameter. This method has shown that the rigidity is highly anisotropic in the Superior province whereas it tends to be more isotropic in the Grenville province.

In the last chapter, we present a study of the gravity and magnetic fields in Ungava Bay. We have mapped potential fields from a compilation of data of different origins: land and satellite data for the gravity field and airborne and shipborne for the magnetic field. The interpretation of these maps leads to the conclusion that a small part of the Superior province was rifted away to the east of the New-Quebec orogen and that several geological structures seen in Labrador extend across the Ungava Bay to Baffin Island. This chapter has been published in a synthesis volume of the ECSOOT (Eastern Canadian Shield Onshore-Offshore Transect) project in the Canadian Journal of Earth Sciences.

Keywords: Canadian Shield, geophysics, gravimetry, magnetics, wavelet transform, Euler's deconvolution, Fourier transform, elastic thickness, Trans-Hudson orogen, Superior province.

Remerciements

Je suis arrivée à Montréal, un soir d'hiver, avec pour tout bagage un sac-à-dos et un "sleeping bag". La nuit tombait, Montréal était sous la glace et je ne connaissais personne. Aujourd'hui, cette thèse est déposée, je vis au Canada et le québécois m'est plus familier que le patois de mon Ardenne natale. Entre temps, il y a eu beaucoup de rencontres, des personnes que j'ai appréciées, aimées, ou qui sont tout simplement passées. Je voudrais les remercier ici, dans le désordre évidemment.

Je vais commencer par *Jean-Claude Mareschal*, pas seulement parce qu'il est mon directeur de thèse. Je lui dois ma venue à Montréal en ce premier jour de la crise du verglas... Il m'a laissé une grande liberté de manoeuvre dans mes recherches tout en étant présent à chaque fois que j'en ai eu besoin, que ce soit pour me donner des idées quand je tournais en rond, que pour me rassurer quand la confiance me manquait. Il a aussi et surtout été très patient. Je le remercie également pour son apport à la cohérence de ce mémoire. Merci beaucoup. *Hélène Gaonac'h* est également à l'origine de cette thèse. Je la remercie de m'avoir laissée libre de mon orientation. Hélène m'a fait decouvrir le monde des objets fractals et la statistique et leurs applications dans les divers domaines des sciences de la Terre. J'ai beaucoup appris. Je lui dois aussi d'avoir fait vivre le dialogue entre les étudiants de tous les labos du GEOTOP en organisant les premiers "Cirque du GEOTOP". Merci Hélène. Je ne sais pas comment remercier ces deux personnes autrement qu'en leur promettant d'agir comme eux avec des étudiants dans ma situation, si un jour l'occasion m'en est donnée.

Je n'oublie pas tous ceux dont l'entousiasme et la motivation font vivre ce drôle de navire qu'est le GEOTOP. Cette thèse existe grâce à eux. Lire un papier ou écrire un programme sont des actes individuels mais ils sont souvent précédés d'interpellations dans un couloir, de débats informels autour de quelques bières, ou de discussions en séminaire. Merci à *Alexandre* pour ses innombrables coups de pouce et ses encouragements permanents. Merci à *Chantal* pour sa bonne humeur, ses blagues dix fois par jour par courriel, et tous les Noël passés ensemble. Merci à *Christian* pour la relecture attentive de plusieurs parties de ce manuscrit. Je n'oublie pas *Roxanne, Pascal* et *Jean-François*, merci pour la bonne ambiance dans le labo de géophysique. Merci à *Hamid* et *Li* qui m'ont accueillie dans ce labo et qui m'ont fait une petite place dans leur famille. Il y a aussi *Hélène I., Youcef, Laurence, Rodolphe, André, Pierrot, Ehouman, Anasse, Edwige, Ratiba, Nawal, Sandrine, Taoufic, Maylis, Stéphanie,* et je dois en oublier... Merci à tous pour votre gentillesse.

Je dois remercier aussi *Isabelle et Céline* qui m'ont bien aidée avec tous les pa-

piers lorsque je suis arrivée, ainsi que *Louise* et *Josée* qui ont ensuite pris la relève. Je n'oublie pas non plus tous les moments de détente à discuter de tout et de rien avec *Bassam, Maryse, Eloi* et *Raynald.*

Je tiens aussi à remercier chaleureusement les membres de mon jury: *Clément Gariépy, Walter Roest* et *Hugo Beltrami.* Leurs commentaires ont énormément amélioré mon manuscrit.

Merci à tous mes professeurs, ils m'ont donné l'envie d'apprendre et de découvrir. Merci surtout à *Madame Vanotti*, professeur de sciences naturelles au Collège d'Attigny. C'est elle qui ma donné le goût de la géologie avec ses sorties sur le terrain et ses travaux pratiques.

Finalement, je remercie infiniment du fond du coeur *Papa* et *Maman*, mon petit frère *Cadet* et ma petite soeur *Fanny*, ainsi que *Paul, Simone,* et *Marguerite*, et tout le reste de ma famille pour qui je n'ai pas été aussi présente que j'aurais aimé l'être durant la réalisation de ce travail. Leur soutien a été précieux et leur présence vitale, même à distance, parfois par caméra interposée, dans les moments de solitude. Merci à *Estelle, Julie, Maxime* et *Antoine* pour tous leurs dessins.

Maintenant, bonne lecture, et que ce mémoire puisse vous apprendre quelque chose !

Contents

List of Figures

General introduction

Potential field anomalies reflect the effect of geological structures at all scales. They vary with the distance from the measurement point to the source. Gravimetric anomalies are due to variations in thickness and composition of the lithosphere (mostly the crust). Bouguer anomalies vary from -300 mGals on land to +300 mGals over oceans. Magnetic anomalies depend on the distribution of magnetic minerals in the part of the crust and mantle below the Curie temperature. Metamorphism and alteration influence the magnetization. The amplitude of the magnetic field anomalies decreases with depth of the sources faster than that of the gravity field. Magnetic methods are therefore more sensitive to shallow structures than gravity. There are two types of magnetization: induced magnetization by the Earth magnetic field and the remnant magnetization from past field. On land, it is assumed that induced magnetization prevails. Marine magnetic anomalies come largely from remnant magnetization.

The analysis of potential fields is useful to obtain information about subsurface structures. Density or magnetization contrasts may be identified from the pattern of potential field anomalies. These patterns reveal discontinuities for example related to the grain aspect or the lineation trends of the studied terrain. Several techniques are available from visual inspection of colored map of fields or directional derivatives of fields to inversion of data in 2 or 3 dimensions to obtain some information on the source distribution. Regardless of the method used, the solution of the inverse problem is non-unique. An infinity of source distributions can explain the measured surface field. The number of solutions can be reduced by adding *a priori* information on the sources and their distribution (for example shape of the source, density or magnetization contrast or smoothness of the distribution). In this thesis, we have studied the potential field anomalies in the Canadian Shield with standard methods such as vertical and horizontal derivatives, Fourier filtering, Euler's deconvolution and Fourier coherence analysis. The continuous wavelet transform was used to complement these methods.

Wavelets are a family of functions deduced from a mother-wavelet by dilatation, translation and rotation. They were developed for high resolution seismic signal

analysis in the early 1980's by *J.Morlet* with *P. Goupillaud* and *A. Grossmann* in the context of hydrocarbon exploration. The mathematical fundations of the method were later later studied and developed by *Y.Meyer, I. Dauberchies, S. Mallat, P.G. Lemarié, C.K. Chui, M. Holschneider, J.P. Antoine* and *R. Murenzi*, among others.

Wavelets have become a significant research approach because of their large range of applications. In mathematics, they have been used to simplify some demonstrations because some wavelet families form a basis for several functional spaces [e.g. *Meyer,* 1993]. Because wavelets are well localized in space and frequency, wavelet transforms are used in a wide range of applications in signal processing. As the Fourier transform, the wavelet transform yields the frequency content of a function, but it keeps the event localized. Wavelet analysis consists in the decomposition of a signal on a basis of functions obtained by dilating and translating a wavelet called analyzing or mother-wavelet. The main characteristic of this analyzing wavelet is that it is localized, *i.e.* it is zero or almost zero outside a given interval.

There are two main approaches to wavelet theory: the continuous wavelet transform and the discrete wavelet transform (or orthogonal wavelet transform). In geophysics, in addition to the seismic applications, the continuous transform permits

fine analysis of atmospheric turbulent signals [*Arneodo et al.,* 1995], time variations of the Earth's magnetic field [*Alexandrescu et al.,* 1995] or seafloor bathymetry maps [*Little*, 1994]. The discrete transform, using orthogonal wavelets, is used mostly for signal and image compression (for example FBI fingerprints database), for noise filtering, and for the solution of partial differential equations. The wavelets are useful to represent signals and to extract information from the signals.

Much effort has been aimed at improving some spectral methods used in geophysics using the wavelet transform. In the first part of this thesis, we describe the methodology used. Wavelet theory will be briefly presented in **chapter 1** where we will discuss the Fourier transform and its limitations and define wavelets and their properties. The continuous wavelet transform will be explained and some wavelet functions will be presented. Some advantages and inconveniences of wavelet transform as well as the choice of the most appropriate wavelet to use will be discussed. In **chapter 2**, we discuss the identification and localization of potential fields sources and we introduce the Poisson wavelet defined by *Moreau et al.* [1997]. Euler's deconvolution is presented in that chapter. In **chapter 3**, the wavelet transform is used for multiscale analysis of gravity and magnetic images. Our objective is to enhance and detect some structural features for the interpretation of data set by visual inspection.

In **chapter 4**, we will use the wavelet transform to study the spectral content of gravity and topography data and determine the elastic thickness and loading of the lithosphere.

The second part of this thesis concerns the geophysical applications of the methods previously described. The study area includes most of the Canadian Shield between the Rae subprovince to the west and the Nain subprovince to the east. These Archean cratons are separated by extended Paleoproterozoic orogenic belts. The Trans-Hudson orogen marks the northern and western margin of the Superior province. The eastern part of the study area includes the New Quebec orogen, the southeastern Churchill province, the Torngat and the Nain craton in Labrador.

In **chapter 5**, we analyse the extensions of the Trans-Hudson orogen and the Western Superior beneath the sedimentary cover of the Williston basin and the Interior platform. We have interpreted shaded colored map of the gravity and magnetic anomalies. We have computed the depth to magnetic basement using Euler's deconvolution. Finally, we have used wavelet-based multiscale derivatives to make enhanced map of structures beneath the sedimentary cover. **Chapter 7** concerns the estimation of elastic thickness of the Eastern Canadian Shield. Because of the

property of localization of wavelet transform, we calculate more local estimates of elastic thickness than with Fourier transforms. We show the great spatial variations and the anisotropy of this lithospheric parameter. **Chapter 8** presents an example of the use of potential fields anomalies to geological interpretation. Classical methods of filtering and derivation were used to continue onshore structures onto the Ungava Bay in northern Quebec. This study has been published in a special number of the *Canadian Journal of Earth Sciences* concerning the synthesis of the Lithoprobe ECSOOT transect (Eastern Canadian Shield Onshore-Offshore Transect).

Notations

$\hat{f}$ is the Fourier transform of a function f

$\mathcal{W}_f$ is the wavelet transform of a function f

$\bar{f}$ is the complex conjugate of f

$\langle\ \rangle$ indicates smoothing or averaging

$\star$ is the convolution operator

ψ generally denotes the wavelet function

a is used most of the time to designate the scale parameter

b is used most of the time to designate the translation parameter

ω is used for frequency, or wavenumber

λ is the Fourier wavelength

$\mathbf{r}$ is a position vector, bold font is used for vector designation

x is the space variable

t is the time variable

D is the rigidity

E is Young's modulus

G is Newton's gravitational constant

ν is Poisson's ratio

T_e denotes the elastic thickness of the lithosphere

Part I

Methodology

Chapter 1

Introduction to wavelet theory

1.1 Introduction

Wavelet transforms belong to a class of methods known as time-frequency decompositions. They generate information about both the frequency content of a signal and its variation with time. Wavelet analysis was introduced in geophysics in the early 1980s for seismic signal analysis in the context of petroleum exploration [*Morlet et al.*, 1982a, b]. It was formalized by *Grossmann and Morlet* in 1984. It is now used in many fields for detection of singularities, signal compression, noise reduction and many other applications. Wavelets permit the decomposition of functions on a basis which is localized in time and frequency taking the advantages of the Fourier

transform but without its lack of localization in time.

In the following, we will restrict ourselves to the one-dimensional case for simplicity but all the definitions and properties can be generalized to the two-dimensional case.

1.1.1 The Heisenberg uncertainty principle

A major interest in time-frequency analysis is to simultaneously determine the energy content of a signal in a narrow time interval and frequency bandwidth. However, the Heisenberg uncertainty principle implies that a gain in time localization causes a loss in frequency localization and vice versa. Simultaneous localizations in time and in frequency are mutually exclusive. The product of time resolution Δt with frequency resolution Δf ("the Heisenberg box") is lower bounded, we have $\Delta t \times \Delta f \geq 1/4\pi$.

1.1.2 Fourier transforms

The Fourier transform consists of decomposing a function on the basis formed by the periodic functions $e^{i\omega t}$ where ω is the frequency and t is the time variable. It is a privileged tool for analysing the frequency content of stationary processes. The

Fourier transform $\hat{f}(\omega)$ of a function $f(t)$ is given by

$$\hat{f}(\omega) = \int_{-\infty}^{+\infty} e^{-i\omega t} f(t) dt \tag{1.1}$$

In general, the original time function can be reconstructed using the inverse Fourier transform

$$f(t) = \frac{1}{2\pi} \int_{-\infty}^{+\infty} e^{i\omega t} \hat{f}(\omega) d\omega \tag{1.2}$$

Fourier spectral analysis is a fundamental tool to study stationary signals, *i.e.* signals which have time invariant statistical properties. However, in transforming to the frequency domain, time information is lost. For example, the power spectrum of a signal composed of two successive sinusoids is not much different from the power spectrum of a signal resulting from the sum of these two sinusoids. The information on the difference between these two signals is contained in the phase and in the Fourier coefficients other than those of the two modes of the sinusoids. Most of the time, in presence of noise, this information will not be available. If available, its interpretation is not obvious, particularly for more complicated signals such as signals with a time varying frequency content. The Fourier and the time representations contain the same information since the Fourier transform pairs permits to go from one domain to the other. However, in each domain, only one kind of information is explicit. In these two domains, the Heisenberg boxes are of infinite area (Fig.1.1 (a) and (b)).

1.1.3 The windowed Fourier transform

To improve time localization but keeping frequency localization, a windowed Fourier transform can be used. This method was refined by *Gabor* [1946] and is called the short time Fourier analysis. It is given by

$$\hat{f}(\omega, b) = \int_{-\infty}^{+\infty} \bar{h}(t-b)e^{-i\omega t} f(t)dt \tag{1.3}$$

where h is an appropriate window centered on the origin. The bar indicates the complex conjugate. $\hat{f}(\omega, b)$ represents the frequency content of f around the position b and the frequency ω. The function h is localized in time and defined on a compact support, *i.e.* it is zero outside a closed and bounded set. Figure 1.1 (c) represents the paving of the time-frequency plane used for short time Fourier analysis. Usually, we choose a Gaussian window. It is not defined on a compact support but decreases rapidly when $|t| \to \infty$. The Gaussian functions, $f(t) = e^{-\pi(at)^2}$, satisfy the Heisenberg principle with $\Delta t \times \Delta f = 1/4\pi$.

The short time Fourier transform provides a time-frequency representation of functions. The drawback is that the size of the window is fixed. Thus this representation is not suited for functions which contain features wider than the window.

1.1.4 The concept of wavelet

The next logical step was to use the short time Fourier transform with variable-sized windows. Instead of fixing the time and the frequency resolution, one can let both resolutions vary in the time-frequency plane. This can be done without violating the Heisenberg principle by fixing the ratio of Δf over f. This is the basic idea of the wavelet theory. Analysis is performed by decomposing the signal on a basis of functions that are localized in time and frequency. These functions are the wavelets. The wavelet basis is a set of dilated and translated copies of one function, the mother-wavelet. The signal is expressed as a linear combination of the wavelet. The complex coefficients of this combination are the wavelet coefficients. We use wide wavelets to represent the low frequencies of a signal. For shorter periods, a good spatial localization is obtained with a narrow wavelet. There will always be wavelets at the right place and having the best-suited size to represent signal variation. However, because of Heisenberg's uncertainty principle, we can only improve spatial resolution at a cost: an increased uncertainty in the frequency localization. Figure 1.1(d) is a time-frequency plane decomposition using wavelet basis. Note that the paving does not need to be dyadic.

1.2 The wavelet: definition and properties

As indicated by its name, a wavelet is a small wave. It means that it is a function oscillating on a limited time range. Outside a given interval, it takes the value of zero or almost zero. It is localized in time and frequency. This property of localization depends on the admissibility condition [*Grossmann and Morlet*, 1984] which is written as

$$C_\psi = \int_{-\infty}^{+\infty} \frac{|\hat{\psi}(\omega)|^2}{|\omega|} d\omega < \infty \tag{1.4}$$

where $\hat{\psi}$ is the Fourier transform of an admissible function, ψ is called the analyzing or mother wavelet. This leads to another property: the wavelet is null at the origin in Fourier domain, $\int_{-\infty}^{+\infty} \psi(t)\, dt = 0 \Rightarrow \hat{\psi}(0) = 0$. It means that it has zero-mean.

From the mother-wavelet, we can construct a family of wavelets. They are obtained by dilatation and translation of the mother-wavelet:

$$\psi_{a,b}(t) = \frac{1}{a}\, \psi\left(\frac{1}{a}\,(t-b)\right) \tag{1.5}$$

The Fourier transform of the daughter-wavelet is

$$\hat{\psi}_{a,b}(\omega) = e^{-i\omega b}\, \hat{\psi}(a\,\omega) \tag{1.6}$$

a is the scale factor. If $a > 1$, the wavelet is wider and contains lower frequencies than its mother. And if $a < 1$, the wavelet is narrower and contains higher frequencies

than its mother. The translation parameter b results in a phase change in Fourier domain.

An important property of the wavelet is the number n of its null moments:

$$\int_{-\infty}^{+\infty} t^k \, \psi(t) \, dt \; = \; 0, \quad \forall \; 0 \leq k < n \tag{1.7}$$

The nullity of the wavelet moments allows the analysis of the local regularity of a signal.

1.3 The continuous wavelet transform: Definition

There are two major approaches to wavelet transforms: the continuous wavelet transform and the discrete wavelet transform. The continuous wavelet transform is done on a continuous range of dilatations and translations. The discrete transform uses a dyadic set of dilatations and translations and it can be an orthogonal transformation. In this study we use only the continuous wavelet transform for its redundancy. Redundancy can be an advantage because it allows a fine analysis of the signal. However it implies a great computational cost and large sets of coefficients to be manipulated. The continuous wavelet transform is not orthogonal but that is not restraining; we do not want an efficient transformation but just extract some

information.

By analogy with the Fourier transform which decomposes signals into linear combinations of sine and cosine waves, the continuous wavelet transform (CWT) analyzes signals as linear combinations of wavelets. The CWT of a function f, which is assumed to be of finite energy, is given by

$$\mathcal{W}_f(a,b) = \frac{1}{\sqrt{C_\psi}} \int_{-\infty}^{+\infty} \bar{\psi}_{a,b}(t)\, f(t)\, dt \tag{1.8}$$

$\mathcal{W}_f(a,b)$ is the wavelet coefficient. For large a, the wavelets are wide and the representation of the function by its wavelet coefficients contains the main features of the function without the details as if we were looking at this function from a distance. On the other hand, the small scales correspond to the details of the signal, a zooming on the function. This type of analysis is useful to study the regularity of functions or fractal structures.

Wavelet transforms have several properties:

- there is no loss of information from the function to its transform;
- the transform is a linear operation;
- the transform is covariant by translation and dilatation.

In Eq.(1.8), we expressed the wavelet transform as a correlation function (just replace $\psi_{a,b}$ by its definition, Eq.(1.5)). By changing $\bar{\psi}(t)$ into $\tilde{\psi}(t) = \bar{\psi}(-t)$, we obtain a second formula for the CWT but as a convolution

$$\mathcal{W}_f(a,b) = \frac{1}{\sqrt{C_\psi}} \int_{-\infty}^{+\infty} \bar{\psi}\left(\frac{t-b}{a}\right) f(t) \frac{dt}{a} \tag{1.9}$$

$$= \frac{1}{\sqrt{C_\psi}} \int_{-\infty}^{+\infty} \tilde{\psi}\left(\frac{b-t}{a}\right) f(t) \frac{dt}{a} \tag{1.10}$$

If the wavelet is real and symmetric, $\tilde{\psi} = \psi$, the two definitions coincide. By introducing the dilatation operator $\mathcal{D}_a$ such that $\mathcal{D}_a s(t) = a^{-1} s(a^{-1}t)$, the wavelet transform can be written as a set of convolutions indexed by a

$$\mathcal{W}_f(a,b) = \frac{1}{\sqrt{C_\psi}} (\mathcal{D}_a \tilde{\psi} * f)(b) \tag{1.11}$$

where the convolution is defined as

$$(\tilde{\psi} * f)(t) = \int_{-\infty}^{+\infty} \tilde{\psi}(t-u) f(u) du = (f * \tilde{\psi})(t) \tag{1.12}$$

1.4 Some wavelet functions

Many functions satisfy the admissibility condition. Other properties such as symmetry or regularity may be introduced depending on the application. We present here two wavelets used for the continuous transform.

1.4.1 The Morlet wavelet

The Morlet wavelet is a complex wavelet (Figure 1.2). It was introduced by Morlet in seismic signal analysis and it is widely used. It is a Gaussian modulated plane wave and is defined in one-dimension by:

$$\psi(t) = \pi^{-1/4} \left(e^{-i\omega_0 t} - e^{-{\omega_0}^2/2} \right) e^{-t^2/2} \tag{1.13}$$

ω_0 is the central frequency of the wavelet and is generally taken ≥ 5 so that the second term of equation 1.13 is negligible and the admissibility condition (Equation 1.4) is satisfied [*Murenzi*, 1990]. On the representation of the Fourier transform of the wavelet (Figure 1.2), we can notice that the peak in $\hat{\psi}(\omega)$ does not occur at frequency a^{-1} (a is the scale parameter). *Meyers et al.* [1993] give a method to derive analytically the relationship between the equivalent Fourier period and the wavelet scale. It consists in calculating the wavelet transform of a sine function of known frequency and finding the scale at which the wavelet power spectrum reaches its maximum (the wavelet power spectrum is defined further in this chapter). For the Morlet wavelet, the scale is related to the Fourier period T [*Torrence and Compo,* 1998] by

$$\frac{4\pi a}{\omega_0 + \sqrt{2 + {\omega_0}^2}} = T \tag{1.14}$$

The Fourier transform of the Morlet wavelet is:

$$\hat{\psi}(\omega) = \pi^{-1/4} \left(e^{-(\omega-\omega_0)^2/2} - e^{-({\omega_0}^2+\omega^2)} \right) \tag{1.15}$$

The use of this wavelet allows a good compromise between time and frequency localization. The Morlet wavelet is complex, it allows phase and argument analysis.

1.4.2 The Mexican Hat wavelet

The Gaussian function is not an admissible wavelet but all its derivatives are admissible. The Mexican Hat wavelet is its second derivative (Figure 1.3). In 2D, its shape is that of a Mexican hat. It is a real-valued wavelet and can be written as

$$\psi(t) = \frac{2}{\sqrt{3}\pi^{1/4}} (1 - t^2) e^{-t^2/2} \tag{1.16}$$

Its Fourier transform is given by

$$\hat{\psi}(\omega) = \frac{2}{\sqrt{3}\pi^{1/4}} \omega^2 e^{-\omega^2/2} \tag{1.17}$$

The scale/wavelength relationship was derived by *Torrence and Compo* [1998]

$$\frac{2\pi a}{\sqrt{3/2}} = T \tag{1.18}$$

This wavelet is also well localized in space and frequency. Since it is a derivative, the Mexican Hat is a good tool for detecting signal discontinuities.

1.4.3 The choice of a wavelet

There is no universal wavelet that can be used in all cases. The selection depends on the studied problem. For border detection, for example, a symmetric wavelet gives large coefficients at each sides of the transition and an antisymmetric wavelet gives large coefficients at the center of the transition [*Hagelberg and Gamage*, 1994]. It is better to use an irregular wavelet such as the simple Haar wavelet when the signal presents sharp variations, and a regular wavelet for smoother signal. The spectral properties of a wavelet may be considered when we need localization in frequency domain. We will see in the next chapter that wavelet can be constructed to specific applications. For instance, *Moreau et al.* [1997] and *Hornby et al.* [1999] have introduced a class of wavelets based on the Poisson semi-group to study potential fields.

1.5 Wavelet spectral analysis

1.5.1 Local wavelet power spectrum and cross spectrum

Given two functions h and g, we can define their local wavelet power spectra and local cross wavelet spectrum as [*Liu*, 1994]:

$$\mathcal{W}_{hh}(a,b) = \frac{1}{C_\psi}|\mathcal{W}_h(a,b)|^2,\ \mathcal{W}_{gg}(a,b) = \frac{1}{C_\psi}|\mathcal{W}_g(a,b)|^2 \tag{1.19}$$

$$\mathcal{W}_{hg}(a,b) = \frac{1}{C_\psi}\mathcal{W}_h(a,b)\mathcal{W}_g^*(a,b). \tag{1.20}$$

The representation of $\mathcal{W}_{hh}(a,b)$ for all a and b is called a scalogram [*Flandrin*, 1988]. The representation of $\mathcal{W}_{hg}(a,b)$ is in analogy a cross scalogram. A scalogram provide an image of the caracteristics of a process in the space-scale plane.

1.5.2 Global wavelet power spectrum

Averaging over all the local wavelet spectra in time gives the global wavelet spectrum:

$$E_h(a) = \frac{1}{N+1}\sum_{i=1}^{N+1}\mathcal{W}_{hh}(a,b_i) \tag{1.21}$$

where i is the index of the discretized time and N is the number of time step.

We can also average in scale to examine the fluctuations in power over a band of

scale.

1.6 Example of continuous wavelet transforms

This example (Figure 1.4) is to illustrate time-frequency analysis with wavelet transform. We consider two signals (units are normalyzed by time units): a signal (a) with a frequency $\omega = 8$ on its first half part and $\omega = 16$ for the second half and another signal (b) with the two frequencies superposed over the entire duration. Morlet wavelet is the analyzing wavelet with $\omega_0 = 5$. We present the scalogram for each signals in (c) and (d). We see clearly the frequency composition of the two signals along the time axis. Plots (e) and (g) are the global wavelet spectra of signals. Plots (f) and (h) are the Fourier power spectra. In these four plots, the x-axis is the frequency axis and the y-axis is the amplitude of spectra. Frequency peaks are thinner in Fourier plots so frequencies are better determined. This is an illustration of Heisenberg's principle, wavelet transforms have a lesser frequency resolution than the global Fourier transform. Images (i) and (j) are a representation of the phase of the wavelet coefficients. We can count the number of cycle.

1.7 Edges detection

We now consider in this chapter 2D images of potential fields. Points of sharp variations represent often the most important features in image. Several automated procedures for potential field data interpretation have been proposed: analysis of symmetrical and asymetrical anomaly components by *Naudy* [1971], the horizontal gradient methods used by *Cordell and Grauch* [1985] later automated by *Blackely and Simpson* [1986], and the 3D Euler deconvolution technique of *Reid et al.* [1990]. Wavelet analysis has been used in the last decade in the field of image processing, mainly as an alternative to Fourier analysis. Under the assumption that geological bodies are sharply bounded and compact, the location of edges in potential field maps corresponds approximately to the location of the source boundaries.

Multiscale edge mapping is a process of mapping edges in potential field data at various spatial scales. In horizontal plane, these edges forms "strings" which are closely related to the lines commonly drawn in 2D visual analysis of potential field maps. *Mallat and Zhong* [1992] show that wavelet transform is a well-suited tool for detecting multiscale boundaries in images.

1.7.1 Multiscale derivative analysis

Hornby et al. [1999] use wavelet transform for multiscale edge mapping of potential fields. Following *Moreau* [1995], they use Poisson's wavelets. They showed that, with appropriate wavelets, the potential field and its spatial derivatives can be treated as the wavelet transform of the source distribution. On profiles, the local maxima of the wavelet transform correspond to the edges of the sources. They applied their method to aeromagnetic data in Australia. The fine scale edges map the magnetic grain of the terrains while coarse scale edges map the margins of plutons.

The methodology we used consists of calculating the 2D continuous wavelet transform of the field. We used the isotropic second order real Poisson wavelet built by rotating the 1D wavelet along its symmetry axis. Images of the transform field can be drawn at different scales and are interpreted by visual inspection.

1.7.2 Local spectra analysis

Bergeron et al. [1999] used Gaussian wavelet transform to look at seismic velocity anomalies (SVA). They defined two parameters from the local spectra of the anomalies: the local maximum of amplitude of the local power spectrum about a local point, E_{max}, and the associated local horizontal wavenumber k_{max}. They showed

that much sharper feature can be discerned in E_{max} map than in the original SVA map. It better delineates tectonic boundary. The k_{max} delineates regions with sharp velocity contrasts. It shows some sharp variations under Iceland that are not visible in SVA.

Simons and Hager [1997] employed wavelet method, but on spherical harmonic representation, to study local spectra of gravity and topography data under Canada and obtain information about the Pleistocene deglaciation and the resulting rebound.

Figure 1.1: Representation of the time-frequency plane paving using (a) time analysis, (b) Fourier transform, (c) short time Fourier transform and (d) wavelet transform.

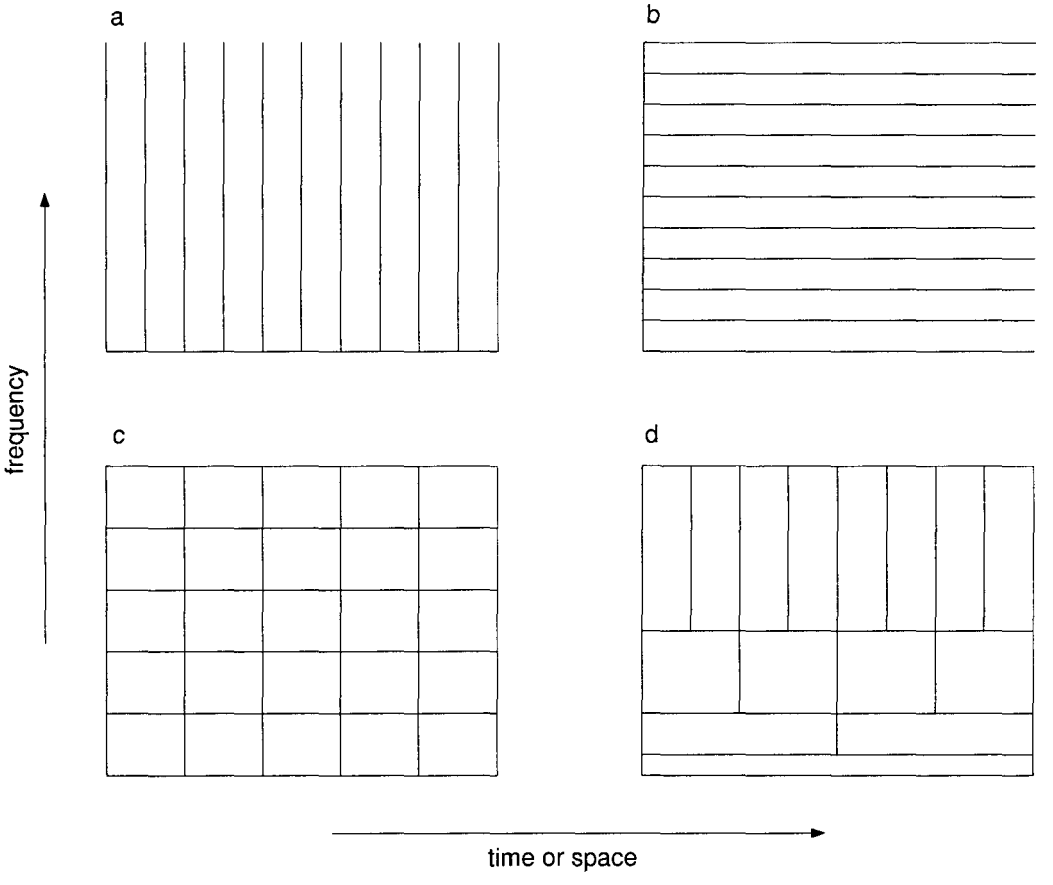
a
b
c
d
frequency
time or space

Figure 1.2: (top) Real (solid line) and imaginary (dashed line) part of Morlet wavelet ($\omega_0 = 5$), and (bottom) its Fourier transform.

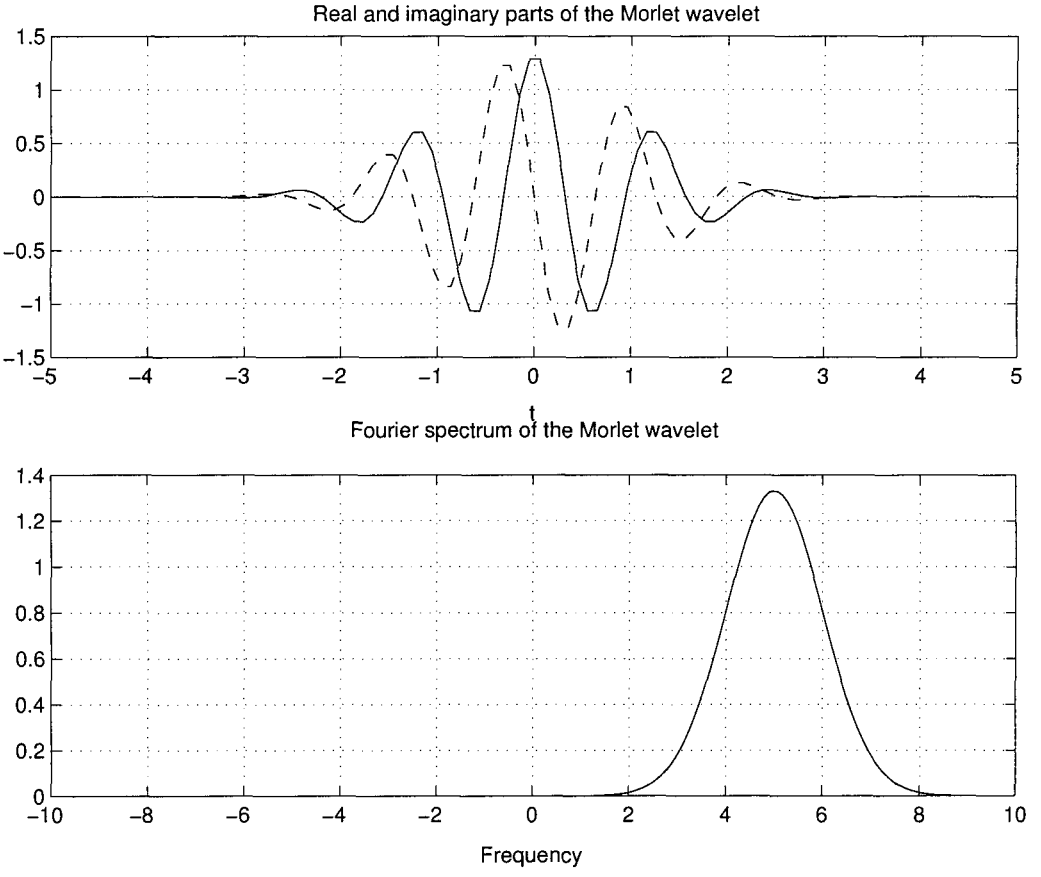
Real and imaginary parts of the Morlet wavelet
1.5
1
0.5
0
−0.5
−1
−1.5
−5
−4
−3
−2
−1
0
1
2
3
4
5
t
Fourier spectrum of the Morlet wavelet
1.4
1.2
1
0.8
0.6
0.4
0.2
0
−10
−8
−6
−4
−2
0
2
4
6
8
10
Frequency

Figure 1.3: (top) The Mexican Hat wavelet, and (bottom) its Fourier transform.

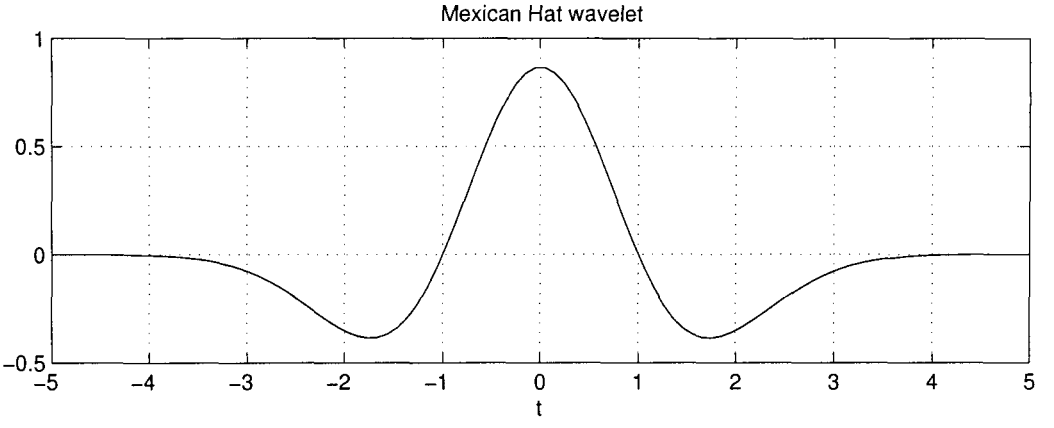
Mexican Hat wavelet
1
0.5
0
−0.5
−5
−4
−3
−2
−1
0
1
2
3
4
5
t

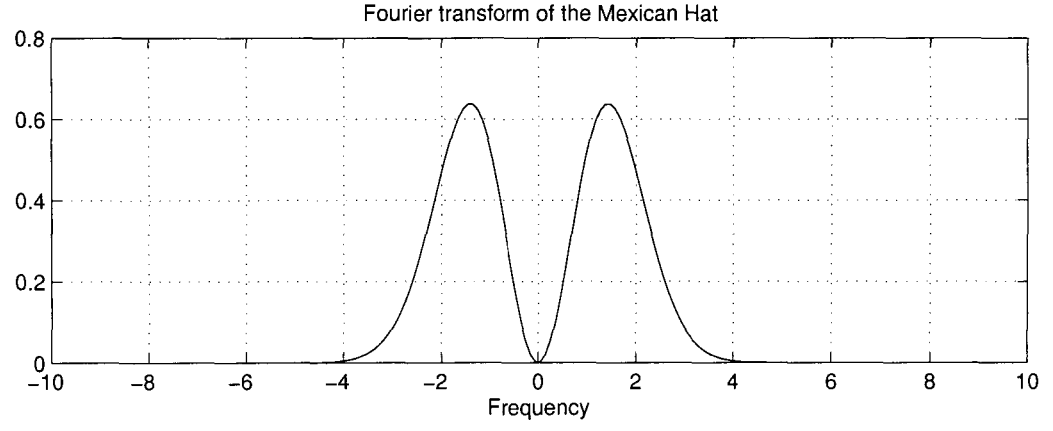
Fourier transform of the Mexican Hat
0.8
0.6
0.4
0.2
0
−10
−8
−6
−4
−2
0
2
4
6
8
10
Frequency

Figure 1.4: Fourier and wavelet analysis of two signals. (a) and (b), the x-axis is the time axis and the y-axis is the signal amplitude axis. (c) and (d), the x-axis is is the time axis and the y-axis is the frequency axis. Blue color are for small values and red for the highest values. (e) to (h), the x-axis is the frequency axis and the y-axis is the power spectrum. (e) and (g) represent global wavlet power spectra of signals a and b; (f) and (h), the Fourier power spectra. (i) and (j), time is the x-axis and frequency, the y-axis. Blue color represent a phase of $-\pi$ and the red color a phase of $+\pi$.

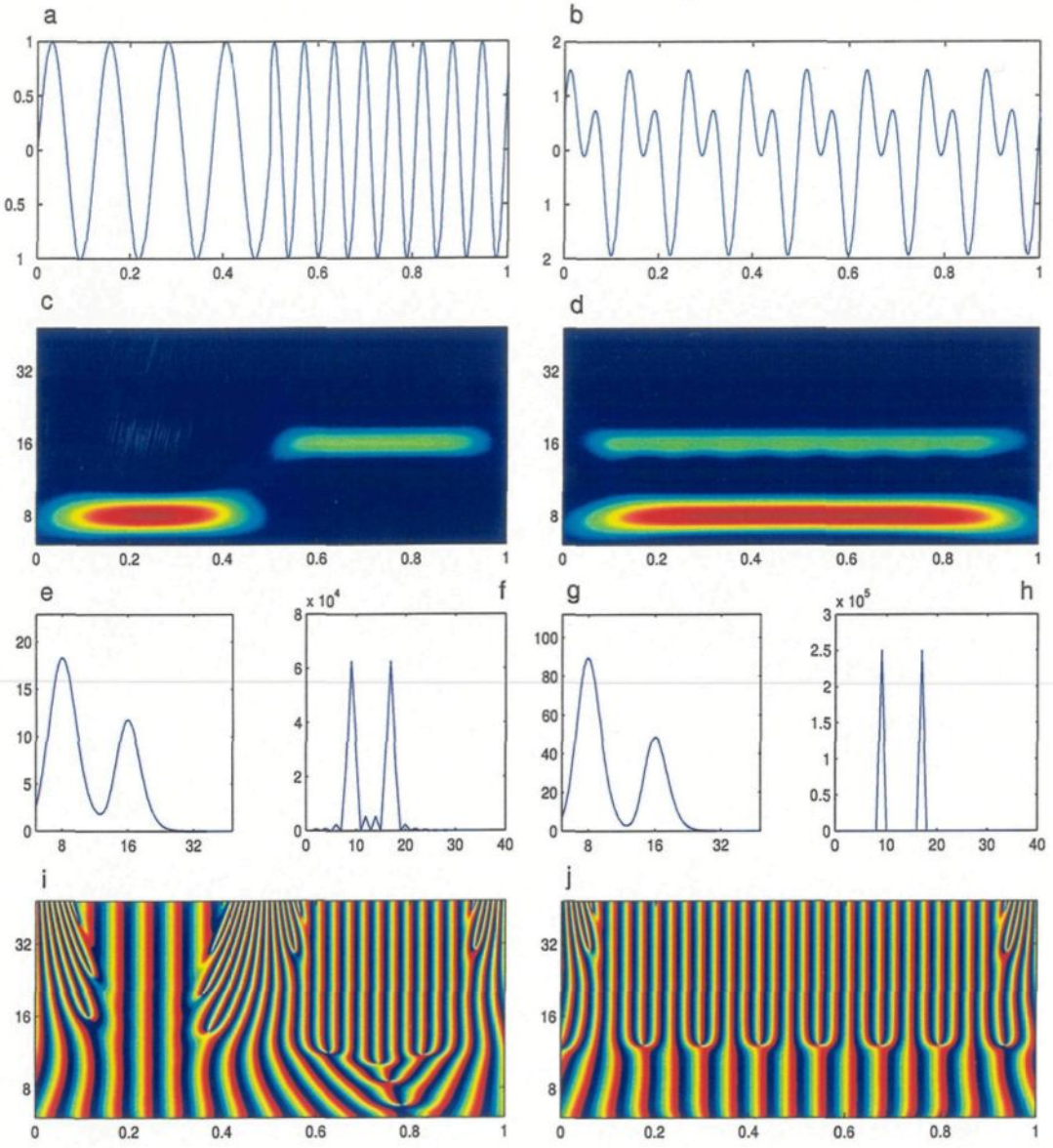
a
b
c
d
e
f
x 10^4
g
h
x 10^5
i
j

Chapter 2

Identification of potential fields sources

2.1 Introduction

One objective of many geophysical studies is to obtain structural images of the substratum from measurements at the surface. Different methods have been developed to determine the depth and the shape of the sources of potential fields anomalies. Some methods assume the shape of the sources as simple geometric forms such as spheres, horizontal or vertical cylinders. Other methods proceed by iterative inversion of model parameters [e.g. *Tanner*, 1967]. They work best when density and some

depth information are available (from seismic profiles for example). For gravity, the field produced by the model is calculated and compared to the data. The parameters of the model are modified until the difference between observed and calculated fields becomes sufficiently small. These are direct methods. Inverse methods determine the properties of the sources directly from the measured field. The inverse problem in potential field data inversion is ill-posed. This ill-posedness is characterized by (1) the non-uniqueness of the solution: even if the potential field is precisely known, an infinity of solutions solve the problem; and (2) the instability of the solution: any insignificant change in the potential field, due to noise or outliers, would result in a completely different solution. The solution is stabilized by introducing some *a priori* information on the sources and their distribution (shape of the source, density or magnetization contrast or smoothness of the distribution for example).

We will present in this chapter a method of interpretation of potential fields data combining image processing and inversion techniques. From the homogeneity of fields originated from point sources and the continuation of harmonic functions, *Moreau et al* [1997] have developed a new method of analysis of potential fields. Because of the scaling properties of the field of a multipolar source, the use of wavelet permits to reduce the number of solutions of the inverse problem. *Moreau et al* [1997]

have constructed a wavelet function based on upward continuation operator. This operator transforms an harmonic field from one surface to another. *Moreau et al* [1997] have shown that the variations of wavelet coefficients with scale reflect the homogeneity order of the source and that the source location can be derived easily through a simple geometric interpretation. The dilatation in the wavelet domain correspond to the upward level in the space domain. *Sailhac et al.* [2000] have used this approach for magnetic anomaly interpretation and *Martelet et al.* [2001] for gravity profile analysis. In this chapter, we will briefly recall the definition of the upward continuation operator and the principle of Euler's deconvolution. Then, a new class of wavelets will be introduced and some synthetic cases will be illustrated.

2.2 Some definitions

2.2.1 Upward continuation

Upward continuation is the transformation of a potential field defined on a surface to its value on another surface (usually farther from the sources). This can be done because outside the sources, potential fields satisfy Laplace's equation. The transformation attenuates the anomalies from shallow sources more than those from deeper ones. Upward continuation is used to look at the field at different scales and to

enhance deep sources at the expense of shallow ones. Downward continuation does the opposite. In space, the effect of upward continuation is defined by a convolution. In a cartesian coordinate system where the (x, y) plane is the horizontal plane and the z-axis is vertical and positive upwards, the upward continuation filter which transforms the field from level z_1 to level $z_2 = z_1 + z$ is given by

$$P_z(x, y) = \frac{1}{\pi} \frac{z}{x^2 + y^2 + z^2} \tag{2.1}$$

The field f upward continued from z_1 to z_2 is

$$f_{z_2}(x, y) = (f_{z_1} * P_z)(x, y), \quad z_2 > z_1 \tag{2.2}$$

The Fourier transform of this operator is

$$\hat{P}_z(\omega_x, \omega_y) = e^{-z\sqrt{\omega_x^2 + \omega_y^2}}, \quad z > 0 \tag{2.3}$$

where ω_x and ω_y are the x and y components of the wavevector.

2.2.2 Euler deconvolution

The Euler deconvolution is a method for estimating the depth of the source of a potential field anomaly. This technique is based on Euler's equation of homogeneity

which defines the structural index corresponding to the homogeneity order (or degree) of the source. Assuming the type of source (its order) we can deduce its depth. *Thompson* [1982] and *Reid et al.* [1990] have used this approach for magnetic data.

A function $f(x, y, z)$ is homogeneous with degree n if $f(ax, ay, az) = a^n f(x, y, z)$. This relation is equivalent to Euler's equation:

$$\mathbf{r} \cdot \nabla f = nf \tag{2.4}$$

where $\mathbf{r}$ is the position vector (x, y, z). When f is a potential field, the exponent n depends on the source and the type of field. It is related to the structural index or attenuation rate N, by $N = -n$ for gravity and $N = -(n + 1)$ for magnetics. As the potential fields of isolated homogeneous sources are functions of the derivatives of $1/|\mathbf{r}|$, they satisfy Euler's equation with their own characteristic integer value n. By considering that f is the potential field due to a single homogeneous source located in (x_0, y_0, z_0) and that the observation location is (x, y, z), we can write

$$\left[\frac{\partial}{\partial x}f(x,y,z) \;\; \frac{\partial}{\partial y}f(x,y,z) \;\; \frac{\partial}{\partial z}f(x,y,z)\right] \begin{bmatrix} x - x_0 \\ y - y_0 \\ z - z_0 \end{bmatrix} = nf(x,y,z) \tag{2.5}$$

From the field measured on the plane $z = 0$, we must determine the unknowns x_0, y_0, z_0 and n. We obtain as many equations as required by writing this equation for various locations. The gradients may be measured or computed from the data using equivalent source transformation [*Emilia*, 1973] or wavenumber domain filtering. Standard algorithms generally assume a value of structural index in order to determine the location of the source (x_0, y_0, z_0). When the source is not a point source, this position locate a point between the top of the source and its center of mass.

In the case of the gravity field, from the expressions for the specific anomalies (given for example in *Telford et al.*, 1990), we find that:

- $n = -2$ for a sphere of uniform density (point mass);
- $n = -1$ for an infinite horizontal cylinder (line mass);
- $n = 0$ for a step.

The Poisson's relation states that for the same causative body with a uniform magnetization and uniform density, the magnetic potential at any point is propor-

tional to the component of the gravity in the direction of magnetization:

$$\mathbf{H} = \frac{k\, H_e}{G\rho} \frac{\partial}{\partial \alpha}(\mathbf{g}) \tag{2.6}$$

where $\mathbf{H}$ is the magnetic anomaly, $\mathbf{g}$ the gravity anomaly, k the magnetic susceptibility, H_e the magnetic field intensity, G the universal gravitational constant, ρ the density and α the direction of magnetization. The Poisson's relation implies the following structural indexes for the magnetics:

- a uniformly magnetized sphere (point dipole) is of order $n = -3$;
- a vertical infinite cylinder (monopole) or a thin horizontal cylinder (line of dipoles) are $n = -2$;
- an infinite thin vertical dike (line of poles) is $n = -1$.

The homogeneity order is not necessarily an integer: *Moreau* [1995] shows that the order of the gravity field of a thin sheet varies with its vertical dimension from -0.625 if it is infinite to -1 (infinite line case). Since the Euler deconvolution method requires the numerical evaluation of horizontal and vertical derivatives from the data, this method is very sensible to noise. Moreover, this works only for isolated sources. The superposition of two sources is no more an homogeneous source.

2.3 The Poisson wavelet

2.3.1 Wavelet transform and homogeneous functions

Because the continuous wavelet transform is a linear operator, the transform of a n-homogeneous function is a n-homogeneous function [*Moreau et al.*, 1997]. Considering an homogeneous function $s(t)$ of degree n, the wavelet transform will satisfy [*Holshneider*, 1995]

$$\mathcal{W}_s(\alpha a, \alpha b) = \alpha^n \mathcal{W}_s(a, b) \tag{2.7}$$

Then the wavelet transform of an homogeneous function is completely determined by one "voice" (*i.e.* the set of wavelet coefficients corresponding to one scale) and we have

$$\mathcal{W}_s(a, b) = a^n \mathcal{W}_s(1, b/a) \tag{2.8}$$

This explains the cone-like structure of the wavelet transform pointing toward the homogeneity center. Moreover, the values of the transform at the maximum for each voice ($\partial_b \mathcal{W}_s(a, b) = 0$) follow a power law with exponent related to the degree of homogeneity of the source. We present on Figure 2.1 an example of Dirac ($n = -1$) and Heaviside ($n = 0$) distributions. We have used the real Poisson wavelet of order $\gamma = 1$ which will be presented in the next section. In this case, the exponent of

the power law is equal to the degree of homogeneity of the analyzed function. The location and the homogeneity order of both functions are exactly recovered.

Since we use the maxima coefficient ridges, this method is very robust even in the presence of noise. The use of several scales permits in some cases to distinguish superposed sources (by attributing a part of the maxima ridge to one source and another part to the other).

2.3.2 Homogeneous sources characterization with the Poisson wavelet

The Poisson wavelet is based on the upward continuation operator. Details of this wavelet and its construction and the harmonic extension as a wavelet transform are presented by *Moreau et al* [1997]. *Hornby et al* [1998] present a similar analysis for potential fields. The wavelet ψ^γ is obtained from the derivative of order γ of the upward continuation operator. Two real wavelets can be considered: the "horizontal" and the "vertical" wavelets ψ_x^γ and ψ_z^γ which correspond to the $(\gamma - 1)$ derivatives of the horizontal and vertical derivatives of the upward continuation operator respectively . We can compose a complex wavelet ψ_c^γ with these two wavelets [*Moreau*,

1995]

$$\psi_x^\gamma = \partial_x^{\gamma-1}\partial_x P_z(x) = \partial_x^\gamma P_z(x) \tag{2.9}$$

$$\psi_z^\gamma = \partial_x^{\gamma-1}\partial_z P_z(x) \tag{2.10}$$

$$\psi_c^\gamma = \psi_x^\gamma - i\psi_z^\gamma \tag{2.11}$$

where $P_z(x)$ is the upward continuation filter which transform the field from the level z_1 to the level $z_2 = z_1 + z$, $P_z(x) = \frac{1}{\pi}\frac{z}{z^2+x^2}$. The complex wavelet transform of the potential field f is

$$\mathcal{W}_{c,\gamma}^f(x,a) = \mathcal{W}_{x,\gamma}^f(x,a) - i\mathcal{W}_{z,\gamma}^f(x,a) \tag{2.12}$$

The norm of the ($\gamma = 1$) complex wavelet transform is [*Martelet et al.*, 2001]

$$|\mathcal{W}_{c,1}^f(x,a)| = a^2 \times \sqrt{(\partial_x f(x,z+a))^2 + (\partial_z f(x,z+a))^2} \tag{2.13}$$

It is related to the analytic signal computed above the level of measurement. The norm of the 1-D analytic signal applied to the field is [*Nabighian*, 1972]

$$|A(x+iz)| = \sqrt{(\partial_x f(x,z))^2 + (\partial_z f(x,z))^2} \tag{2.14}$$

Nabighian [1972] used the analytic signal to resolve magnetic anomalies due to polygonal cross-section structures and to perform reduction to the pole. The analytic

signal is also used as input in Euler's deconvolution [*Reid et al.*, 1999].

Horizontal and vertical wavelets of order $\gamma = 1$ are shown on Figure 2.2 with their Fourier transforms.

2.3.3 Properties of the Poisson wavelet transform

For homogeneous functions, two voices of the wavelet transform corresponding to scales a and a' are related by

$$\mathcal{W}(a,b) = \left(\frac{a}{a'}\right)^{\gamma} \left(\frac{a'+z_0}{a+z_0}\right)^{-\beta} \mathcal{W}\left(a', b\,\frac{a'+z_0}{a+z_0}\right) \tag{2.15}$$

where z_0 is the depth of the source (defined positive downwards, scales are positives upwards)[*Moreau et al.*, 1999]. γ is the order of the wavelet and β is an exponent depending on the homogeneity order of the field, $\beta = -(\gamma - n)$. This formula shows that n and z_0 can be estimated from only two voices of the transform. The estimation can be improved with several voices. On a representation of the modulus of the wavelet coefficient on the time-scale plane, the cone-like structure converges at the scale $a = -z_0$. On a log-log scale, $|\mathcal{W}_a|$ does no longer vary linearly with a as in Figure 2.1. A change of coordinate and a scaling are necessary to recover the linear variation. The plot of $\log\left(|\mathcal{W}_a|/a^{\gamma}\right)$ as a function of $\log\left(a+z_0\right)$ is a line with a slope

of β. This method is equivalent to Euler deconvolution. The advantage is that the structural index is determined from the data and does not have to be obtained by trial and error as in Euler deconvolution. This result holds for any of ψ_x, ψ_z or ψ_c wavelet. For the gravity field of point sources, real wavelets are sufficient. We need complex wavelets to determine the inclination of a dipole source in magnetics or the inclination of extended sources in gravity. This inclination is obtained from the argument of the wavelet coefficients. *Moreau* [1995] has shown that for a dipole of inclination I, the argument of the wavelet coefficients along the maxima ridge is constant and equal to $I + \pi[2\pi]$ for the complex wavelet of order $\gamma = 1$. *Sailhac et al.* [2000] give some relations between the phase of the wavelet coefficients and the apparent inclination of the sources for local and extended multipoles.

2.4 Isolated homogeneous sources analysis

2.4.1 Synthetic example in gravity

We consider a two dimensional example (*i.e.* the sources are infinite in an horizontal direction). We define the coordinate system in the plane perpendicular to that dimension with x horizontal and z positive downwards. We locate the source at $x = 0$ and $z = z_0$ and we add white Gaussian noise to the signal. The vertical

component of the field g due to this horizontal line mass can be written as

$$g_z(x,z) = G\rho \frac{2(z_o - z)}{x^2 + (z - z_0)^2} \tag{2.16}$$

where G is Newton's gravitational constant and ρ is the linear density. Euler's equation for this type of sources is

$$x\frac{\partial g_z}{\partial x} + (z - z_0)\frac{\partial g_z}{\partial z} = -g_z(x,z) \tag{2.17}$$

It implies that the homogeneity order of a horizontal line mass is $n = -1$.

Figure 2.3 presents the field and the analysis with the real first order($\gamma = 1$) Poisson wavelet. We can observe that the coefficients corresponding to large scales are less affected by noise than those at smaller scales. The wavelet transform of a Gaussian white noise is also a Gaussian white noise. It can be shown that the variation of the amplitude of the wavelet coefficients associated with the noise vary with scale as $a^{-1/2}$ [*Moreau*, 1995]. The noise creates additionnal lines of extrema. For both presented cases, we find a linear relation between scales and wavelet coefficients on a loglog plot. The slope $\beta = -2$ gives the order of the source, $n = \beta + \gamma = -1$. Even with strong noise, the location and the order are well recovered.

2.4.2 Synthetic example in magnetics

We now consider the magnetic field of an infinite horizontal line of dipoles with the same coordinates as before. For a magnetic sources, we need to determine not only the depth but also the inclination of the dipole. In $z = 0$ and assuming that y is parallel to the declination, the magnetic total field anomaly is

$$A(x) = -2\,\frac{2\,x\,z_0\,\cos I + (x^2 - z_0^2)\,\sin I}{(x^2 + z_0^2)^2} \tag{2.18}$$

The homogeneity order of such a source is $n = -2$. This example is presented in figure 2.4. Since we have only one maxima ridge, we recover only the horizontal location of the source. We can increase the number of ridges with wavelets of higher order γ. The loglog plot of amplitude *vs.* scale yields the order of the source. With $\beta = -3$, the order $n = \beta + \gamma = -2$. Figure 2.5 (f) is the argument calculated along the maxima ridge of the complex coefficient modulus. It seems to converge to the inclination I of the dipole.

2.5 Extended sources

By linearity the wavelet transform of the field originating from an extended source is the sum of the wavelet transforms of the effect of each point source constituting

this extended source [*Moreau*, 1995].

2.5.1 Gravimetric synthetic cases

We now consider the gravimetric anomaly for an inclined step in the same coordinate system as before. Considering an inclined step defined by its upper and lower corner (x_1, z_1) and (x_2, z_2), the gravimetric anomaly can be written as

$$\begin{aligned} g_z(x, z=0) &= 2z_2 \arctan\left(\frac{x_2 - x}{z_2}\right) - 2z_1 \arctan\left(\frac{x_1 - x}{z_1}\right) \\ &+ 2(z_2 - z_1)\frac{(x - x_1)z_2 - (x - x_2)z_1}{(x_2 - x_1)^2 + (z_2 - z_1)^2} \ln\left(\frac{r_1}{r_2}\right) \\ &- 2(x_2 - x_1)\frac{(x - x_1)z_2 - (x - x_2)z_1}{(x_2 - x_1)^2 + (z_2 - z_1)^2} \cdots \\ &\cdots \left(\arctan\left(\frac{x_2 - x}{z_2}\right) - \arctan\left(\frac{x_1 - x}{z_1}\right)\right) \end{aligned} \tag{2.19}$$

where r_1 and r_2 are the norms of the position vectors (x_1, z_1) and (x_2, z_2). We have studied this example with the first-order complex Poisson wavelet. Figure 2.5 presents this example.

Modulus maxima lines intercept near the center of the step. In fact, these lines are no longer straight. For low dilatations, they are curved toward the upper edge of the step. However, these low dilatations are often polluted with noise in real data so this localization is not available. The homogeneity order of the source is

obtained from a loglog plot of $\log(|\mathcal{W}_a|/a^\gamma)$ as a function of $\log(a+z_0)$. We have $n = \beta + \gamma = -1 + 1 = 0$. We plot on figure 2.5(f) the phase taken along the maxima ridges versus the scale, this gives the inclination of the step.

2.6 Last Remark

We use the ratio of wavelet coefficients at two differents scales to compute the position and the order of the source. Another method may be considered. We can use the ratio of the coefficients from the transform with two different orders of wavelet. Hence, the order of wavelet disappear:

$$\frac{\mathcal{W}_{\psi^{\gamma+1}}(a,b)}{\mathcal{W}_{\psi^\gamma}(a,b)} = \left(\frac{a}{a'}\right)\left(\frac{a'+z_0}{a+z_0}\right)\frac{\mathcal{W}_{\psi^{\gamma+1}}\left(a', b\,\frac{a'+z_0}{a+z_0}\right)}{\mathcal{W}_{\psi^\gamma}\left(a', b\,\frac{a'+z_0}{a+z_0}\right)} \tag{2.20}$$

where $\mathcal{W}_{\psi^\gamma}$ and $\mathcal{W}_{\psi^{\gamma+1}}$ denote wavelet coefficients from the transform with the wavelet of order γ and $\gamma+1$. This equation can be compared to the equation (2.15). The depth of the source of the potential field is obtained from (2.20) as:

$$z_0 = \frac{Qa - a'}{1 - Q} \tag{2.21}$$

where

$$Q = \left(\frac{a'}{a}\right)\frac{\mathcal{W}_{\psi^{\gamma+1}}(a,b)}{\mathcal{W}_{\psi^\gamma}(a,b)}\frac{\mathcal{W}_{\psi^\gamma}\left(a', b\,\frac{a'+z_0}{a+z_0}\right)}{\mathcal{W}_{\psi^{\gamma+1}}\left(a', b\,\frac{a'+z_0}{a+z_0}\right)}. \tag{2.22}$$

The index can be determined as descussed earlier. For each dilation we can compute the structural index and depth. These parameters should be constant while varying the dilation for a monopole source. Otherwise, the source should be an extended or multipolar source. I have not tested this procedure enough to show significant results. An advantage over the method proposed by *Moreau et al.* [1997] is that from now on we do not have to use a trial and error process to estimate the depth.

Figure 2.1: Dirac and Heaviside functions analysis. (a) and (c) are the wavelet transform coefficients of Dirac and Heaviside, respectively. Maxima lines are superposed in white. (b) and (d) show the scaling relation between the scale and the coefficients along maxima ridge. The slope β is related to the homogeneity order.

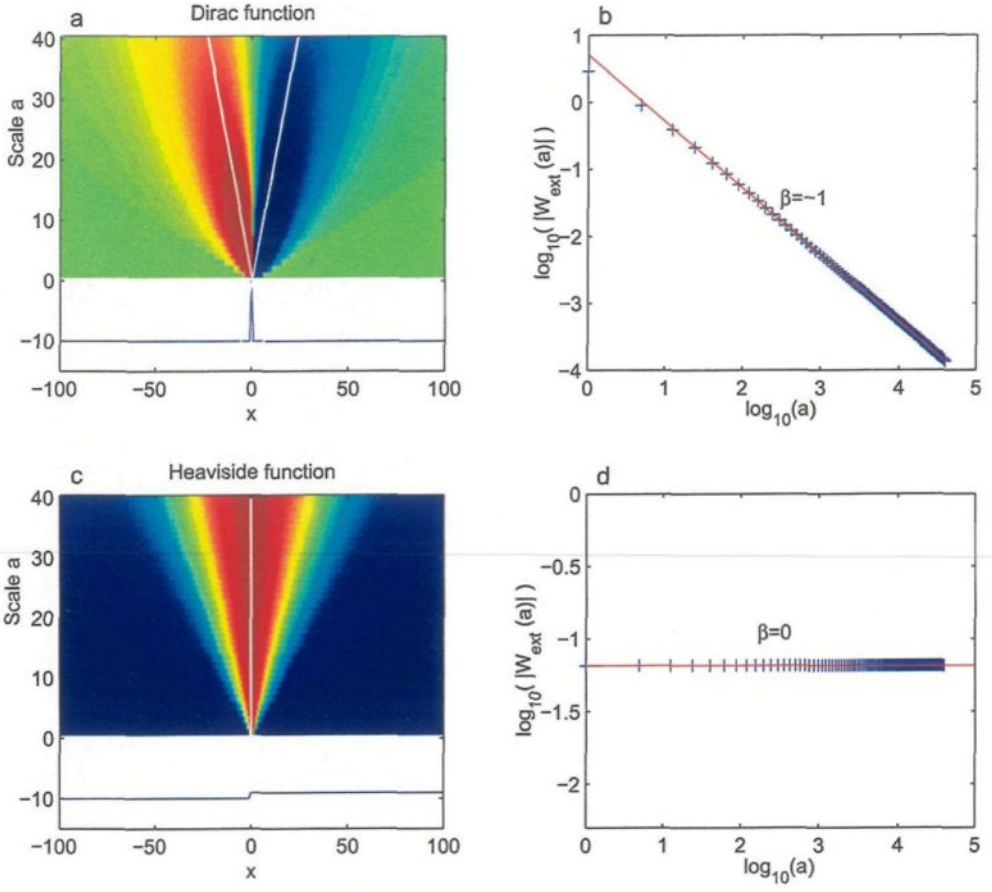
a
Dirac function
Scale a
x
b
β=−1
log10(|Wext (a)|)
log10(a)
c
Heaviside function
Scale a
x
d
β=0
log10(|Wext (a)|)
log10(a)

Figure 2.2: Horizontal (a) and vertical (c) Poisson wavelet for $\gamma = 1$ and their Fourier transform (b and d). For the horizontal wavelet, the real part of its Fourier transform is null, it is the same for the imaginary part of the Fourier transform of the vertical wavelet (because of their symmetry).

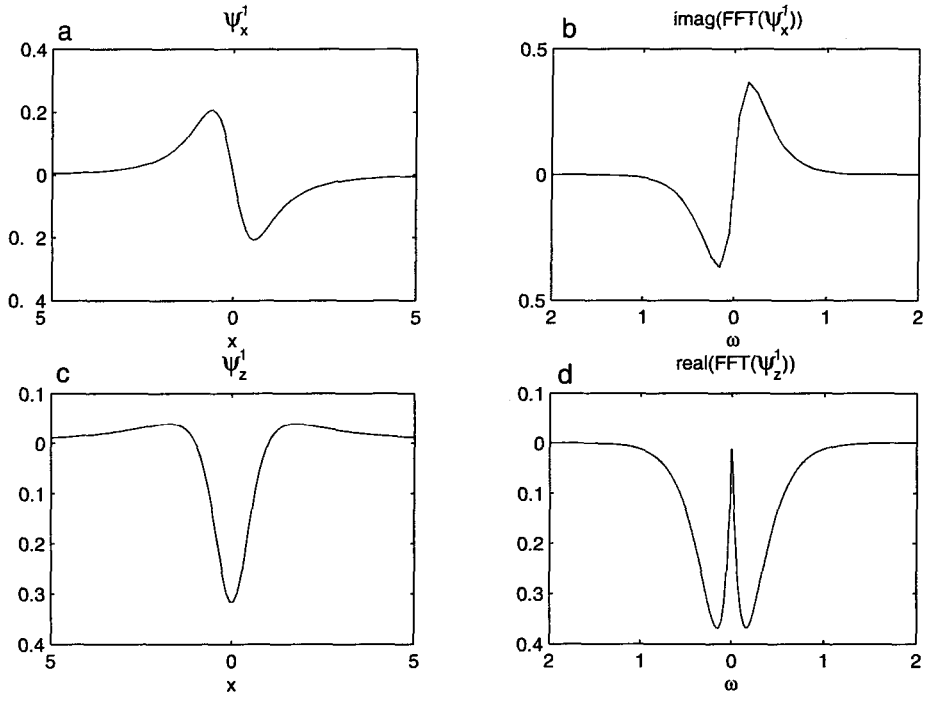
a
ψ_x^1
0.4
0.2
0
0. 2
0. 4
5
0
5
x
b
imag(FFT(ψ_x^1))
0.5
0
0.5
2
1
0
1
2
ω
c
ψ_z^1
0.1
0
0.1
0.2
0.3
0.4
5
0
5
x
d
real(FFT(ψ_z^1))
0.1
0
0.1
0.2
0.3
0.4
2
1
0
1
2
ω

Figure 2.3: Wavelet transform of the gravity field in the case of an infinite line. The position of the source is indicated by a red open square on (a) and (d). All length units (horizontal distance, depth and scales) are normalized by the depth z_0. For the top three figures, we have added a white noise with a maximum amplitude of 25% of the variance of the signal. For the bottom figures, the noise is 100% of the variance. (b) and (e) show the analyzed signal. We have used the real first order ($\gamma = 1$) Poisson wavelet. (a) and (d) show the wavelet coefficients. The maxima ridges related to the source are outlined in white. Blue lines are the linear best fit lines of the maxima ridges continued in the negative scales domain. We use all scales on figure (a) and scales $a > 20$ on (d) to do this fit. These lines cross exactly at the location of the source. Plots (c) and (f) show the scaling relationship between scales and maxima coefficients.

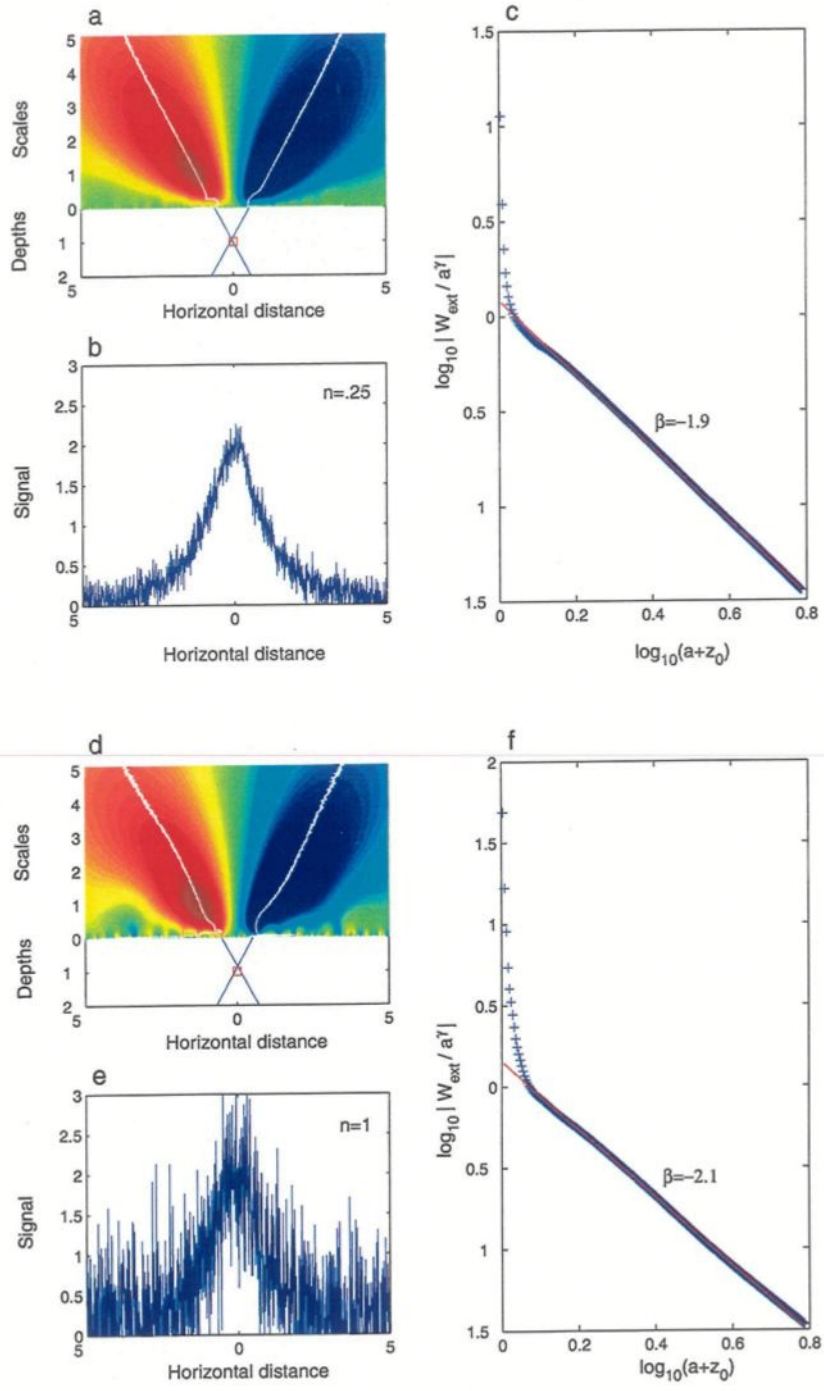
a
Scales
Depths
Horizontal distance
b
Signal
n=.25
Horizontal distance
c
log10 | Wext / aγ |
β=−1.9
log10(a+z0)
d
Scales
Depths
Horizontal distance
e
Signal
n=1
Horizontal distance
f
log10 | Wext / aγ |
β=−2.1
log10(a+z0)

Figure 2.4: Wavelet transform of the magnetic field in the case of an infinite line of dipoles with an inclination $I = 30°$. (a) is the analyzed signal, (b) is the wavelet coefficients calculated with the real ($\gamma = 1$) Poisson wavelet. The maxima ridges (drawn in white) intercept at the location of the source. (c) and (e) are the modulus and the argument of the wavelet coefficients obtained with the complex ($\gamma = 1$) Poisson wavelet.

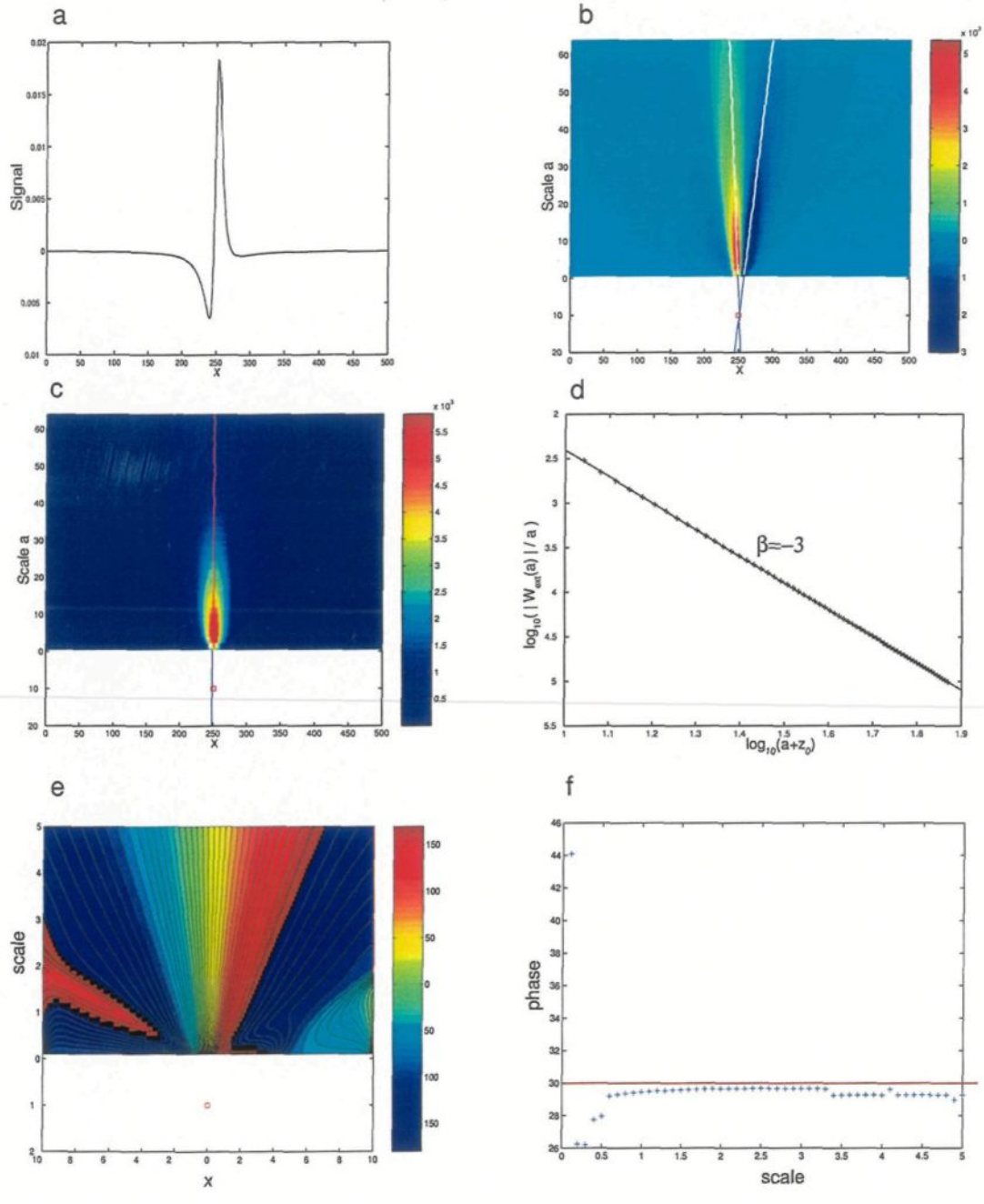
a
Signal
x
b
Scale a
x
c
Scale a
x
d
β=−3
log10(| Wψ(a) | / a)
log10(a+z0)
e
scale
x
f
phase
scale

Figure 2.5: Wavelet transform of the gravity field in the case an inclined step. (a) presents the gravimetric anomaly. The real part of the wavelet transform coefficients is shown in (b). The norm of the complex wavelet transform coefficient is shown in (c). (d) is the loglog representation of the maximum coefficients *vs.* scales leading to the homogeneity order of the source. (e) shows the phase of the wavelet ceofficients. (f) represents the phase taken along the maxima ridges versus the scale.

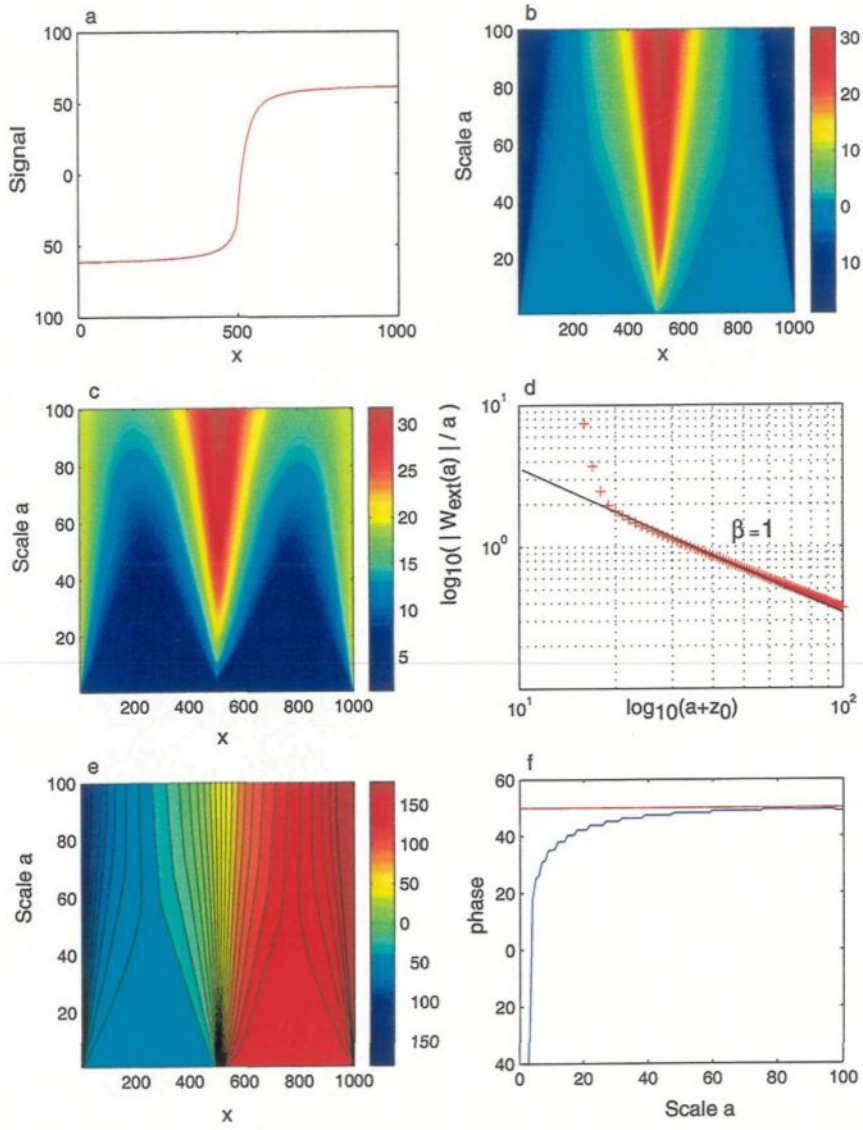
a
Signal
x
b
Scale a
x
c
Scale a
x
d
log10(| Wext(a) | / a)
β = 1
log10(a+z0)
e
Scale a
x
f
phase
Scale a

Chapter 3

Lithospheric elastic thickness estimation

3.1 Introduction

Isostasy implies that the Earth is in hydrostatic equilibrium beneath the compensation depth. Pratt's isostatic model proposes that the topography is compensated by lateral variations of the density of the crust whereas the Airy's model considers lateral variations of crustal thickness. Flexural isostasy extends the idea of isostasy and provides a physical mechanism that explains how it is achieved. Gravitational equilibrium over geological times ($> 10^4$ years) is reached by the flexure of the litho-

sphere under loads. The lithosphere can be modeled as a thin elastic plate overlaying an inviscid fluid (asthenosphere) loaded at the surface and on horizontal planes (density interfaces). For a thin elastic plate, the response depends on the elastic thickness T_e which is a measure of the "strength" of the plate. The elastic thickness T_e of the lithosphere corresponds to the thickness of an equivalent elastic plate which would bend in the same way under applied loads.

Elastic plate flexure is governed by the fourth-order partial differential equation [*Turcotte and Schubert*, 1982]

$$\nabla^2 . (D\nabla^2\tilde{w}) + p\nabla^2\tilde{w} = q \tag{3.1}$$

where $\tilde{w}$ is the vertical deflection of the plate, p is the horizontal force per unit length and q is the vertical force per unit area imposed to the plate. The flexural response of the plate depends on a single parameter, the rigidity D (in N m). This rigidity is related to *Te* by:

$$D = \frac{ET_e^3}{12(1-\nu^2)} \tag{3.2}$$

where E is Young's modulus and ν Poisson's ratio.

Oceanic and continental lithosphere are loaded by seamounts or mountain ranges

formed by continental collision. Airy's model corresponds to a zero rigidity plate (full compensation). The stronger the lithosphere, the wider the topography it can support. Small objects are not compensated because the lithosphere is strong enough to support the load. Wide loads (compared to the elastic thickness) are balanced by deflection of the lithosphere. Correlation of Bouguer gravity anomalies with topography is thus wavelength dependent. The transition wavelength from compensated to uncompensated topography is used to estimate the lithospheric rigidity. For the oceanic lithosphere, the elastic thickness depends on its thermal age. It coincides with the depth to the base of the mechanical lithosphere (450 or 600 °C isotherm)[*Watts*, 1978]. T_e increases from the ridge to older sea floor.

For continental regions, several factors control T_e: it depends of the thermal state, the composition and the thickness of the lithosphere and on the stress distribution [*Burov and Diament*, 1995]. T_e varies widely, 5 to more than 100 km and has large spatial variations [e.g. *Bechtel et al.*, 1990; *Pilkington*, 1991; *Wang and Mareschal*, 1999 for the North American continent].

Forward modelling of gravity data and spectral techniques are used to estimate *Te*. Forward modelling is done on profiles and gives T_e variations along it. Spectral

methods provide an average estimate of T_e for a region. The T_e can be estimated from the admittance or from the coherence between Bouguer or free air gravity anomaly and topography (Figure 3.1). Admittance methods assume that the loading is at the surface or that it is internal but they cannot discriminate between the two loads. Continental admittance studies in the US [*Dorman and Lewis*, 1970] and in Australia [*McNutt and Parker*, 1978] suggest that the continents are weak (low elastic thickness). No clear relation with the thermal state or the age of the continental lithosphere was derived from these studies. For continental lithosphere, *Forsyth* [1985] has shown that T_e is underestimeted if bottom or interior loading contribute to the flexure when using a surface load model. Admittance functions from bottom loading models and those from top loading models have noticeable differences. Coherence allows the decomposition of the load into surface and internal parts [*Forsyth*, 1985]. Application of the coherence method to the North American lithosphere shows that it has a high strength core (with T_e greater than hundred kilometers) with lower values around [*Bechtel et al.*, 1990]. *Lowry and Smith* [1994] obtained a range of 20 to 80 km for T_e in the Western US. However, *McKenzie and Fairhead* [1997] used coherence method with free air gravity rather than Bouguer gravity and obtained smaller values for T_e for continental lithosphere in several areas. They argued that the effective elastic thickness of continental lithosphere never exceeds 25 km except for the Himalayan

foredeep.

There are many ways to estimate coherence. Standard Fourier methods are commonly used but have poor spatial resolution. *Lowry and Smith* [1994] develop a maximum entropy based coherence method from the maximum entropy spectrum estimation (MESE) algorithm of *Lim and Malik* [1981]. This method led to a better spatial resolution because low wavenumber are better resolved. This can be done because maximum entropy spectra can be estimated outside the wavenumber range of the Fourier transform. This "extrapolation" is based on an assumption on the data (minimum correlation). It gives a good approximation of coherence even if the transitional wavelengths are of similar size to the width of the data window. It allows the use of smaller grids than with standard Fourier method and improves the spatial resolution. *Simons et al.* [2000] introduced the use of multitaper spectral analysis for anisotropy studies. Wavelets method were proposed by *Stark and Stewart* [1997]. Fourier and wavelets methods are presented in this chapter.

3.2 Coherence method to estimate the elastic thickness

The rigidity of the lithosphere can be estimated by comparing observed and predicted coherence between Bouguer gravity data and topography. The coherence between two functions is obtained from their spectra F and G as:

$$\gamma^2 = \frac{|\langle \bar{F}G \rangle|^2}{\langle \bar{F}F \rangle \langle \bar{G}G \rangle} \tag{3.3}$$

where $\langle\rangle$ denotes band averaging. This is done to avoid the coherence to be one. The coherence function measures the consistency of the phase relationship between two signals. It is a positive number between 0 and 1 that depends on the fraction of the gravity field that can be related by a linear transfer function to the topography. Coherence estimation is presented in the next section.

Predicted coherence is obtained following the method proposed by *Forsyth* [1985]. For a given flexural rigidity the initial amplitudes of topography H_I and subsurface load interface W_I are solved from the observed Fourier components of topography H and Bouguer anomaly W [eqs.(20) and (21), *Forsyth*, 1985]

$$H_I = \left(H + W\frac{\Delta\rho}{\rho_0\phi}\right)\left(\frac{\rho_0 + \Delta\rho\xi}{\Delta\rho}\right)\left(\frac{\phi}{\phi\xi - 1}\right) \tag{3.4}$$

$$W_I = \left(W + H\frac{\rho_0}{\Delta\rho\xi}\right)\left(\frac{\Delta\rho + \rho_0\phi}{\rho_0}\right)\left(\frac{\xi}{\phi\xi - 1}\right) \tag{3.5}$$

where

$$\xi = 1 + Dk^4/\Delta\rho g \tag{3.6}$$

$$\phi = 1 + Dk^4/\rho_0 g \tag{3.7}$$

H is the Fourier transform of the amplitude of the surface topography. W is the Fourier transform of the amplitude of the Moho relief which is obtained from upward continuation of the Bouguer anomaly. ρ_0 is the density of the load and $\Delta\rho$ is the density contrast at the compensation interface (generally the crust-mantle interface). H_I and W_I are solved and unique except when $D = 0$ or in Airy case ($\phi\xi - 1 = 0$).

The initial loads are then decomposed using the desired rigidity D into components H_T and W_T due to surface loading and H_B and W_B due to subsurface loading (Figure 3.2) [eqs.(16) and (17), *Forsyth*, 1985]:

$$H_I = H_T - W_T \tag{3.8}$$

$$W_I = W_B - H_B \tag{3.9}$$

If surface and subsurface loadings have a random phase (i.e. they are uncorrelated),

the coherence will be [eq.(25), *Forsyth*, 1985]:

$$\gamma^2 = \frac{\langle H_T W_T + H_B W_B \rangle^2}{\langle H_T^2 + H_B^2 \rangle \langle W_T^2 + W_B^2 \rangle} \tag{3.10}$$

where $\langle\rangle$ is an average over wavenumber bands. Predicted coherence is estimated for several values of T_e and compared to the observed coherence to find the best fit.

The observed coherence is defined as [*McKenzie and Bowin*, 1976]

$$\gamma_{obs}^2 = \frac{C^2}{E_0 \cdot E_1} \tag{3.11}$$

where C^2 is the complex cross spectrum and E_0 and E_1 are respectively the power of topography and Bouguer gravity.

3.3 Coherence Estimation

3.3.1 Fourier method

Coherence calculation requires estimations of spectral properties of signals (in our case, gravity and topography). The periodogram is one spectral estimator. It is the squared magnitude of the coefficients of the Fourier transform of the signal. Before applying the Fourier transform, we can apply mirroring or windowing on the signal. This improves the estimation of the periodogram. On the other hand, this

adds wrong information in the signal. To avoid the coherence being unity, we have to average the numerator and denominator of equation (3.11). In this thesis, we choose to average the periodogram on annuli of wavenumber bands. Doing that, we loose the azimuthal information. There are other ways to average estimates. This can be done by using several estimates computed for overlapping sections of the signal [*Welch*, 1967]. Ensemble averaging can also be used. Several realisations of the same process are needed. *Watts* [1978] used this method to study isostasy in oceanic areas.

3.3.2 Wavelets Method

Here we chose to use wavelet-based methods because of their ability to give information both in space and frequency domain. The mother wavelet used is the Morlet's wavelet [*Morlet et al.*, 1982] because of its well defined scale/Fourier period relationship [*Torrence and Compo*, 1998]. We used a wavelet with a central frequency $\omega_0 = 5$ (equation 1.13) for this study. Our tests have shown that coherence is independent of the value of this parameter.

Given two functions h and g, in the same way as with Fourier transform, we can

define the coherence function by:

$$\gamma^2(a,b) = \frac{|\langle a^{-1}\mathcal{W}_{hg}(a,b)\rangle|^2}{\langle a^{-1}\mathcal{W}_{hh}(a,b)\rangle\langle a^{-1}\mathcal{W}_{gg}(a,b)\rangle} \tag{3.12}$$

where $\langle\rangle$ is for averaging or smoothing (without averaging, the numerator and denominator in equation 3.12 would be the same and coherence would always be 1). Because of the definition of the Morlet's wavelet, we first tried to smooth spectra in the space dimension by a Gaussian window as wide as the dilated wavelet at each scale. But finally we decided to average spectra on a space interval without windowing. It does not change much the coherence curve and it is faster. To avoid coherence always being 1, *Liu* [1994] considered separately the real and imaginary parts of the coherence. *Torrence and Webster* [1999] applied smoothing on spectra in both time and scale space.

Figure 3.1: Admittance and coherence theoritical curves between gravity anomaly and topography. (a) Bouguer admittance, (b) Bouguer coherence, (c) free air admittance, and (d) free air coherence for a model that consists of a crust of 35 km thickness with a density varying from 2600 kg m^{-3} at the surface to 3125 kg m^{-3} at its base, overlying a mantle of density of 3300 kg m^{-3}. The elastic response is calculated with $T_e = 50$ km and several values of load ratio f: $f = 0$, solid line, $f = 1$, dashed line, $f = 2$, dash-dotted line, and $f = 4$, dotted line. We see that Bouguer coherence is the less affected by the load ratio.

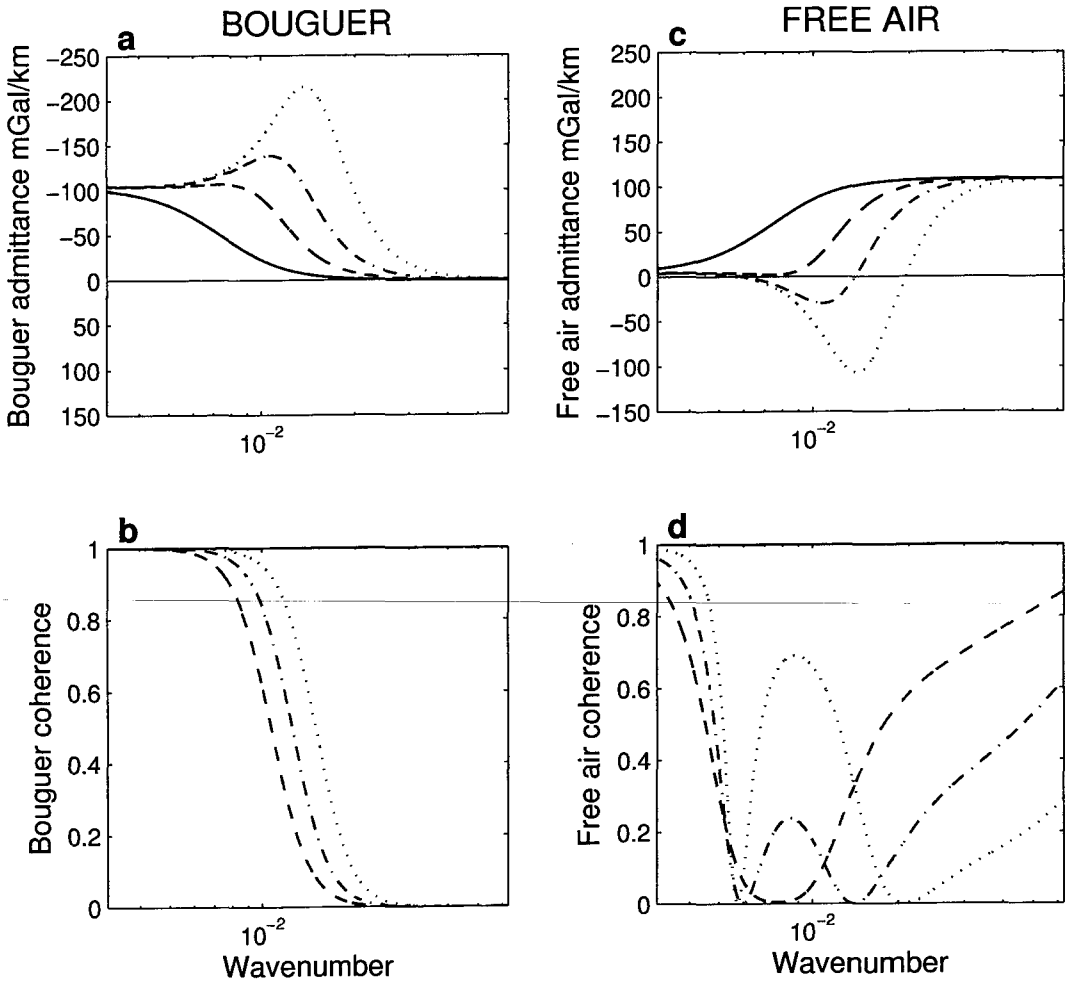
BOUGUER
FREE AIR
a
b
c
d
Bouguer admittance mGal/km
Free air admittance mGal/km
Bouguer coherence
Free air coherence
Wavenumber
Wavenumber
10^{-2}
10^{-2}
10^{-2}
10^{-2}
−250
−200
−150
−100
−50
0
50
100
150
250
200
150
100
50
0
−50
−100
−150
1
0.8
0.6
0.4
0.2
0

Figure 3.2: Illustration of the response of an elastic plate to sinusoidal loads (modified from *Forsyth* [1985]). Dotted areas representsthe crust and shaded areas, the mantle. H_I is the amplitude of the initial topographic load placed on the surface of the plate. This leads to surface relief with amplitude H_T and Moho relief with amplitude W_T. W_I is the amplitude of the initial load on the Moho. It results in surface relief with amplitude H_B and Moho relief with amplitude W_B. The results of both loads is H and B.

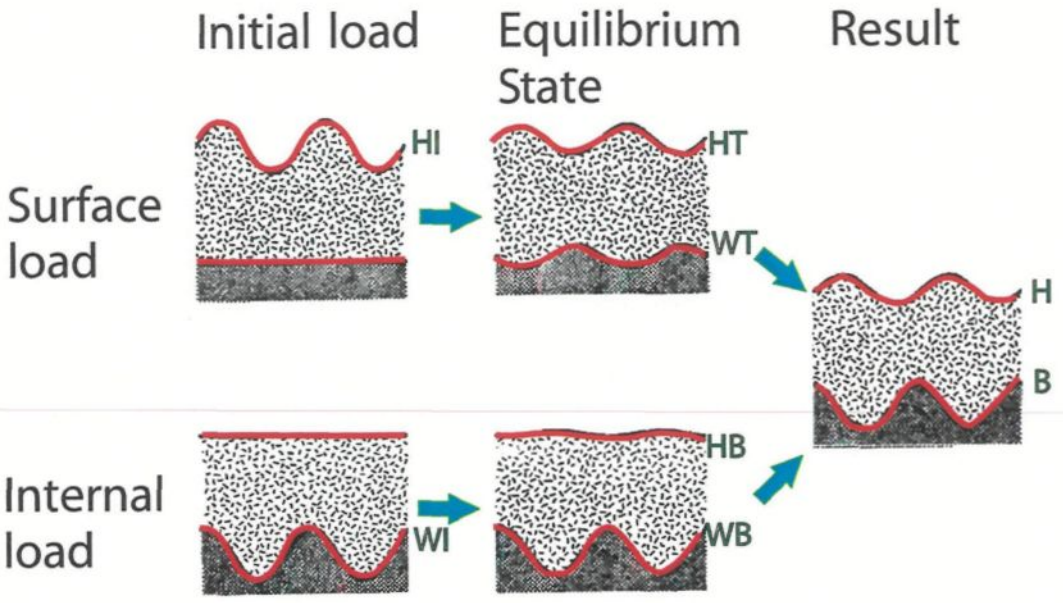
Initial load
Equilibrium State
Result
Surface load
HI
HT
WT
H
B
Internal load
WI
HB
WB

Part II

Applications

Chapter 4

Mapping of the Precambrian basement beneath the Williston sedimentary basin

4.1 Introduction

Within North America, the Trans-Hudson orogen (THO) is the only fully preserved Paleoproterozoic belt [*Hoffmann*, 1981]. It extends from South Dakota through Manitoba, Saskatchewan and Hudson Bay to the Cape Smith Belt in Northern Quebec. North of N54.5° , it exposes a complete orogenic section characterized by a

zone of juvenile (1.9-1.8 Ga) rocks sandwiched between reworked Archean continental blocks (Superior craton to the southeast and Hearne craton to the north-west). To the south, the juvenile crust is thrustover the smaller Sask craton [*Lewry and Stauffer*, 1990; *Lucas et al.*, 1993; *Ashton et al.*, 1994].

We used gravity and magnetic anomaly data to map the basement under the sedimentary cover of the Williston basin. We made a direct interpretation of the data using color-coded and shaded map of magnetics and gravity. Complementary work was done using wavelet based methods to calculate multiscale derivatives and local spectra which better outline features than standard derivatives. We also computed depth to magnetic basement using the Euler method as described by *Thompson* [1982]. The method of source characterization presented in chapter 2 has been used to study the gravity anomalies over the Churchill-Superior boundary zone and the Tabbernor fault .

4.2 Geological framework

Exposed basement structures in central Canada are shown on the geologic map (Figure 4.1). From west to east, we have the Rae and the Hearne provinces, the Rein-

deer tectonic zone, which is the main part of the THO, and the Churchill-Superior boundary zone. They are separated by major structural breaks and are divided into smaller units.

The Rae province is exposed north and south of the Athabasca basin. The southern part consists mainly of Archean ($>$ 2.5 Ga) felsic to mafic rocks intruded by younger granites ($\approx$ 1.8 Ga) and mafic dykes. The northern part is composed of several cratonic blocks made up of Archean rocks separated by shear zones. The Hearne province (the former Cree Lake zone) comprises the Virgin River, Mudjatik and Wollaston granitoid domains.

The Reindeer tectonic zone [*Stauffer*, 1984] is a 400km wide collage of early Proterozoic arc volcanics, plutons and sediments: (1) the Rottenstone domain comprises the andean-type 1.8 Ga Wathaman batholith [*Meyer et al.*, 1992] and the Rottenstone migmatite belt; (2) the La Ronge domain is composed of metavocanic and metasedimentary belts (La Ronge and Lynn Lake); (3) the Glennie domain is made up of early Proterozoic greenstone belts in granitoid terrain; (4) the Flin Flon domain includes the Flin Flon - Snow Lake belt and the former Hanson block which are made up of arc volcanic and plutonic rocks and (5) the Kisseynew Gneiss domain.

The Sask craton, an Archean microcontinental block, is exposed in windows under the former Hanson block in the central part of the juvenile Reindeer zone and may extend southward in North Dakota [*Baird et al.*, 1996].

Three major breaks separate these elements. The Snowbird tectonic zone separates the Rae and the Hearne provinces. This structure may be a Paleoproterozoic collisional suture [*Hoffman*, 1990] or a transcurrent fault of Paleozoic [*Lewry and Sibbald*, 1980; *Lewry and Collerson*, 1990] or Archean age [*Hanmer et al.*, 1994]. The question is still debated. The Needle Falls shear zone has been traced between the Wathaman batholith and the Wollaston domain. The Tabbernor fault zone forms the boundary between the Glennie and the Kisseynew domains.

The Churchill-Superior boundary is a narrow zone made of continental margin deposit and/or reworked basement along the margin of the Superior craton. Based on lithologic assemblages, structrural trends and metamorphism grade, the Superior province has been divided into several subprovinces, broadly east-west trending [*Card and Ciesielski*, 1986]. The elongated form of these subprovinces suggests that the Superior craton was formed by crustal accretion in a convergent plate setting. Oceanic crust, insular arcs, sedimentary prisms and continental fragments would have been

assembled from north to south on the North American cratonic core. The borders of the subprovinces are sutures that separated independant tectonic units until the final assembly at 2.7 Ga. The Western Superior is the part of the craton that lies to the southwest of the Hudson Bay. From the south, it consists of the volcano-plutonic Wawa suprovince, the metasedimentary Quetico subprovince, the Wabigoon, Winnipeg River and Bird River plutonic and volcanoplutonic subprovinces, the metasedimentary English River subprovince, the Uchi, Berens and Sachigo plutonic and volcanoplutonic subprovinces and the high grade gneisses Pikwitonei subprovince. In many places, limits of subprovinces are placed along faults. The Sydney Lake fault forms part of the Uchi-English River boundary.

4.3 Geophysical data

The magnetic and gravity data were provided by the Geological Survey of Canada (GSC; online at `http://gdcinfo.agg.nrcan.gc.ca/misc/can_grids_e.html`).

Most aeromagnetic data were acquired at an altitude of 305 m mean terrain clearance and the standard flight-line spacing is 800 m. More detailed surveys were conducted with a < 400 m flight-line spacing over the N55° margin of the Phanero-

zoic basin.

For the gravity set, the data spacing ranges from less than 1 km to over 20 km, with an average spacing between 5 and 10 km. All measurements were reduced to the International Gravity Standardization Network 1971 (IGSN71) datum. Theoretical gravity values were calculated from the Geodetic Reference System 1967 (GRS67) gravity formula. Bouguer anomalies were calculated using a vertical gravity gradient of 0.3086 mGal/m and a crustal density of 2 670 kg/m^3. We complete the gravity set below the Canada-US boundary with the gravity data from the Decade of North American Geology database.

Both grid were placed on a 2' ($\approx$ 4 km) grid. Colour shaded relief maps are shown in figures 4.2 and 4.3.

4.4 Potential fields maps

4.4.1 Bouguer gravity map

The Superior province is characterized by an east-west fabric truncated by the north-south fabric of to the Trans-Hudson orogen. The Bouguer gravity map is dom-

inated by the high-low pair of anomalies (≈30 mGal) associated with the Churchill-Superior boundary zone which is marked gravity high.The signature of the edge of the Superior province follows the same direction to N51° . But south of this latitude, the anomaly weakens and changes direction. It continues to the US border at least.

In the Superior province, the Winnipeg River and the core of the Berens plutonic subprovinces are also outlined by high anomaly as well as the metasedimentary English River subprovince. The greenstone-plutonic Uchi and Wabigoon subprovinces contain the lowest gravity values of the Western Superior province. These subprovinces can be traced under the Williston basin. We shall try to find the better way to outline their pattern.

In the Reinder tectonic zone of the TransHudon orogen, the central part of the metasedimentary Kisseynew domain shows high gravity values (>-35 mGal). The Wollaston domain is characterized by lower values (-60 mGal). It extends as far south as N52° . The edges of the Glennie domain seems to be marked by low values of gravity. These low values border a region which can be extended also to N52° . The Flin Flon domain is characterized by short wavelength gravity. That continue as far south as N53° .

4.4.2 Aeromagnetic map

The magnetic map has much higher resolution the gravity map. The domains described on the gravity map are well visible. The extent of subprovinces interpreted on the gravity map is confirmed on the aeromagnetic map. The major breaks of the Trans-Hudson orogen are marked by linear anomalies. The Needle Falls shear zone between the Wollaston domain and the Wathaman batholith extends southward to N53° where it meets the Archean Medicine Hat province (situated in the lower left corner of the map). The Wathaman batholith is characterized by a magnetic high. *Hoffman* [1988] does not recognize this structure further south than N54° but the width of the aeromagnetic anomaly does not change. This batholith lies possibly under the Wollaston domain in the south. The Tabbernor fault which separates the Glennie domain from the Kisseynew domain is marked by a steep magnetic gradient zone. That extends southward to the US border. The Snowbird tectonic zone between the Hearne and the Rae cratons is a pronounced thin band of high values which extends to the north across the Athabasca Basin. The Superior boundary zone is marked by a magnetic anomaly high and a broad low.

The North American Central Plains (NACP) conductivity anomaly [*Jones and Savage*, 1986] has no evident signature in the aeromagnetics nor in the gravity. It

may be represented by a gravity high of 40 mGal in the South. It seems to follows the Tabbernor fault in the south and the Needle Falls shear zone north of N52° .

4.4.3 Wavelet transform maps

Figure 4.4 shows the wavelet transform of the gravity field. It has been done with the 2D second order Poisson wavelet and at a scale of 20 km. We have examined several wavelet transform maps at different scales from 12 km to 120 km. The extrema observed on these maps can be interpreted as the position of the edge of geological features. The Trans-Hudson orogen is characterized by a serie of north-south lineaments of extrema. It is separated from the Superior province by a band made up of high-low bands of values. In the Superior, trends are mostly east-west. Beneath the sedimentary cover, lineaments correspond to extension of subprovinces boundaries defined previously. It allows to refine our interpretation of the magnetic and gravity maps. Lineaments in the Trans-Hudson can be followed beyond the latitude of N52° .

4.5 Depth to magnetic basement

Magnetization contrasts within basement rocks are much larger than in the mostly non magnetic sediments. Density does not vary so dramatically and magnetics is

more sensitive to shallow sources while gravity integrates shallow and deep sources. Distinct magnetic anomalies are usually produced by distinct source bodies, while gravity anomalies integrate several density variations. The depths to basement (the source of magnetic anomalies) is usually obtained from magnetic data inversion.

We used the magnetic data set to determined the depth to the top of the magnetic sources using Euler's deconvolution [*Thomson*, 1982]. We extract north-south profiles at 12' spacing from N49° to N59° , between longitudes W110° and W95° , and east-west profiles at 6' from W110° to W95° between latitudes N49° and N55° . All profiles were resampled at 1 km interval. We reduced the data to the pole using the same field, inclination and declination values for all profiles. We solved Euler's equation for a structural index of 0.5 which is used for describes contacts [*Reid et al.*, 1990]. "Bad" solutions were rejected on the basis of the distance between two successive sources criterium. After several trials, we choose a maximum horizontal distance of 20 km between two sources. Depths should be less than 30 km and positive. We used a window of 150 km which is perhaps too large. We choose this width to reduce the number of solutions and to include broad anomalies arising from deep sources. Solutions were filtered by block averaging using the L2 norm to avoid aliasing short wavelengths and interpolated using ajustable curvature surface gridding algorithm

[*Smith and Wessel*, 1990]. We present the data in the form of a color contour plot in figure 4.5.

On the map of the depth to the magnetic basement (Figure 4.5), the most prominent feature is a step along the meridian of W103° . That corresponds to the Tabbernor fault. Solutions of Euler equation give depths near 30km for this feature to the south. This is in agreement with the interpretation of seismic profiles of CO-CORP [*Nelson et al.*, 1993] and LITHOPROBE [*Lucas et al.*, 1994]. The Tabbernor fault can be followed to the north across the Wathaman batholith and the Wollaston domain. This was not clear on the potential fields maps. Steep gradients also mark the Snowbird tectonic zone. As on the potential fields maps, it seems to end at a latitude of N52° . Basement beneath the Flin Flon domain extends southward. The maximum depths to basement is found beneath the NACP conductivity anomaly.

4.6 Wavelet study of the Churchill-Superior boundary zone and the Tabbernor fault

The wavelet methods presented in Chapter 2 are applied here to gravity to find the nature (*i.e.* structural index), the depth and the inclination of two structural

discontinuities: the Superior-Churchill boundary zone and the Tabbernor fault. We used east-west gravity profiles between N50° and N54° . Between these two latitudes, these breaks are the features presenting the higher wavelet coefficients (Figures 4.6 a and b). We test several values of depth z_o to find the best linear fit between the wavelet coefficients and the scale in a log-log plot (Figure 4.6 h). The CSBZ is characterized by z_o varying between 18 km to 35 km, an index N=1 to 2 and phase (corresponds to the inclination of the structure in the case of N=1) varying from 50° for the large scales to 10° for the smaller scales in the west direction. The Tabbernor fault is N=0.5 to 1.5, $z_0 = 8$ to 27 km and a constant phase of 50° in the West direction. Index N=0 correspond to a step and N=1 to a thin vertical sheet. Both can be used to described a contact or a fault.

4.7 Conclusions

Figure 4.7 shows our interpretation of the different maps we have presented above. The main conclusions are:

- The belts of the Superior province extend westward. They are truncated by the Churchill-Superior boundary .

- The Thomson belt which marks the Churchill-Superior boundary is traced as

far south as N48° (and may extend southward).

- The Flin Flon domain can be followed all along the Thomson belt.
- The Hanson block, the Glennie domain, the La Ronge domain and the Wollaston domain continue southward to N52° . They are truncated by a feature corresponding to a magnetic low (may be related to the Medicine Hat craton).

Figure 4.1: Generalized geology of the Western Superior province and the Trans-Hudson Orogen, modified after *Card and Ciesielski* [1985] and *Hoffman* [1988]. Black lines mark the limits of the major subprovinces. Discontinuous lines mark the northeastern edge of the Interior platform basin and the Southwestern limit of the Hudson Bay basin. Thin black lines are national boundaries and major lakes.

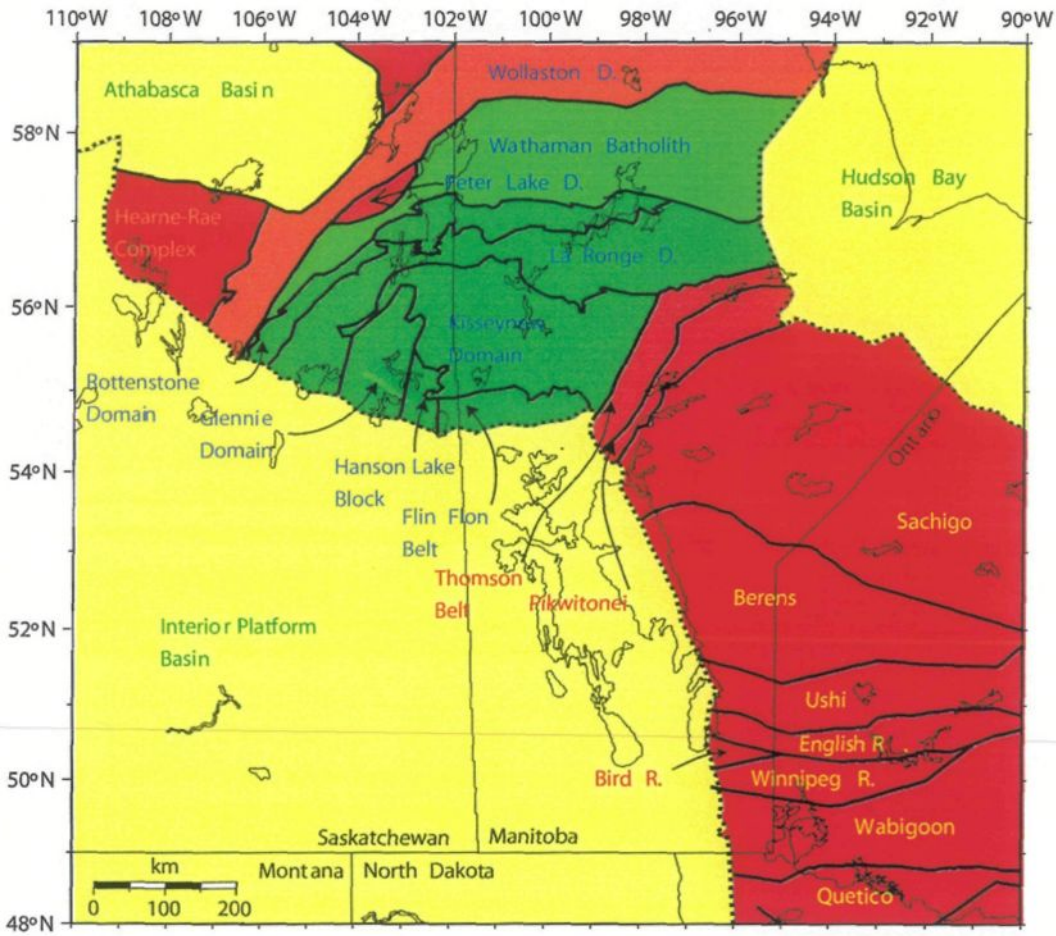
110°W
108°W
106°W
104°W
102°W
100°W
98°W
96°W
94°W
92°W
90°W
58°N
56°N
54°N
52°N
50°N
48°N
Athabasca Basin
Wollaston D.
Wathaman Batholith
Peter Lake D.
Hearne-Rae Complex
La Ronge D.
Kisseynew Domain
Hudson Bay Basin
Bottenstone Domain
Glennie Domain
Hanson Lake Block
Flin Flon Belt
Thomson Belt
Rikwitonei
Ontario
Sachigo
Berens
Interior Platform Basin
Ushi
English R.
Bird R.
Winnipeg R.
Wabigoon
Quetico
Saskatchewan
Manitoba
Montana
North Dakota
km
0
100
200
Sedimentary cover
Lower Proterozoic continental margin magmatic arc
Juvenile island arc rocks and metasements of TransHudson Orogen
Lower Proterozoic metavolcanic-metasediment arc rocks
Zones of reactivated Archean crust
Archean Provinces

Figure 4.2: Bouguer gravity map based on GSC and DNAG data. Colors were adjusted to better display tectonics features. The map is illuminated from the north. Boundaries are the same as on figure 4.1.

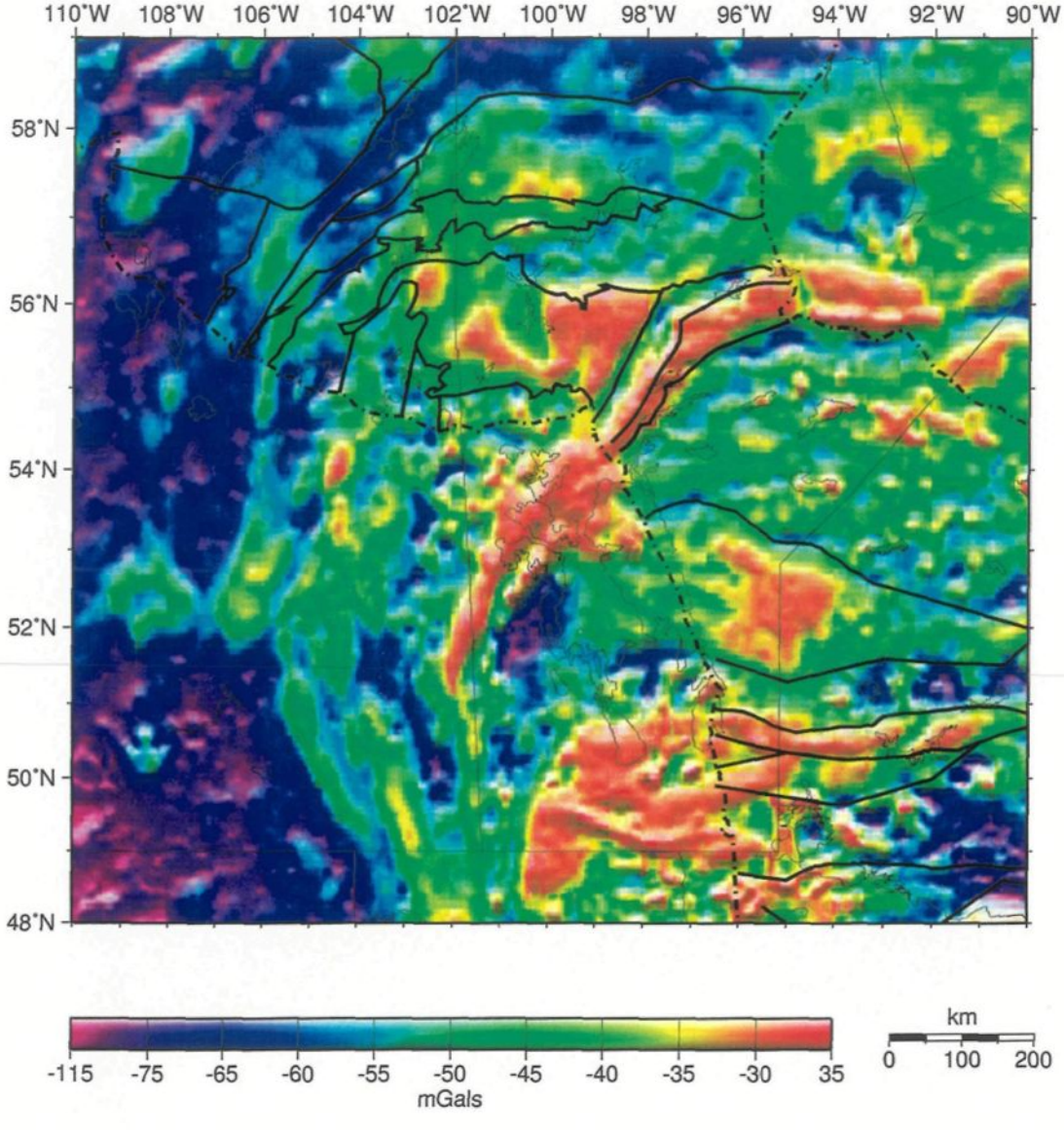
110°W
108°W
106°W
104°W
102°W
100°W
98°W
96°W
94°W
92°W
90°W
58°N
56°N
54°N
52°N
50°N
48°N
-115
-75
-65
-60
-55
-50
-45
-40
-35
-30
35
mGals
km
0
100
200

Figure 4.3: Total magnetic field map based on aeromagnetic data from the GSC. A variable color scaling was used to better display the main geological features. Boundaries are the same as on figure 4.1.

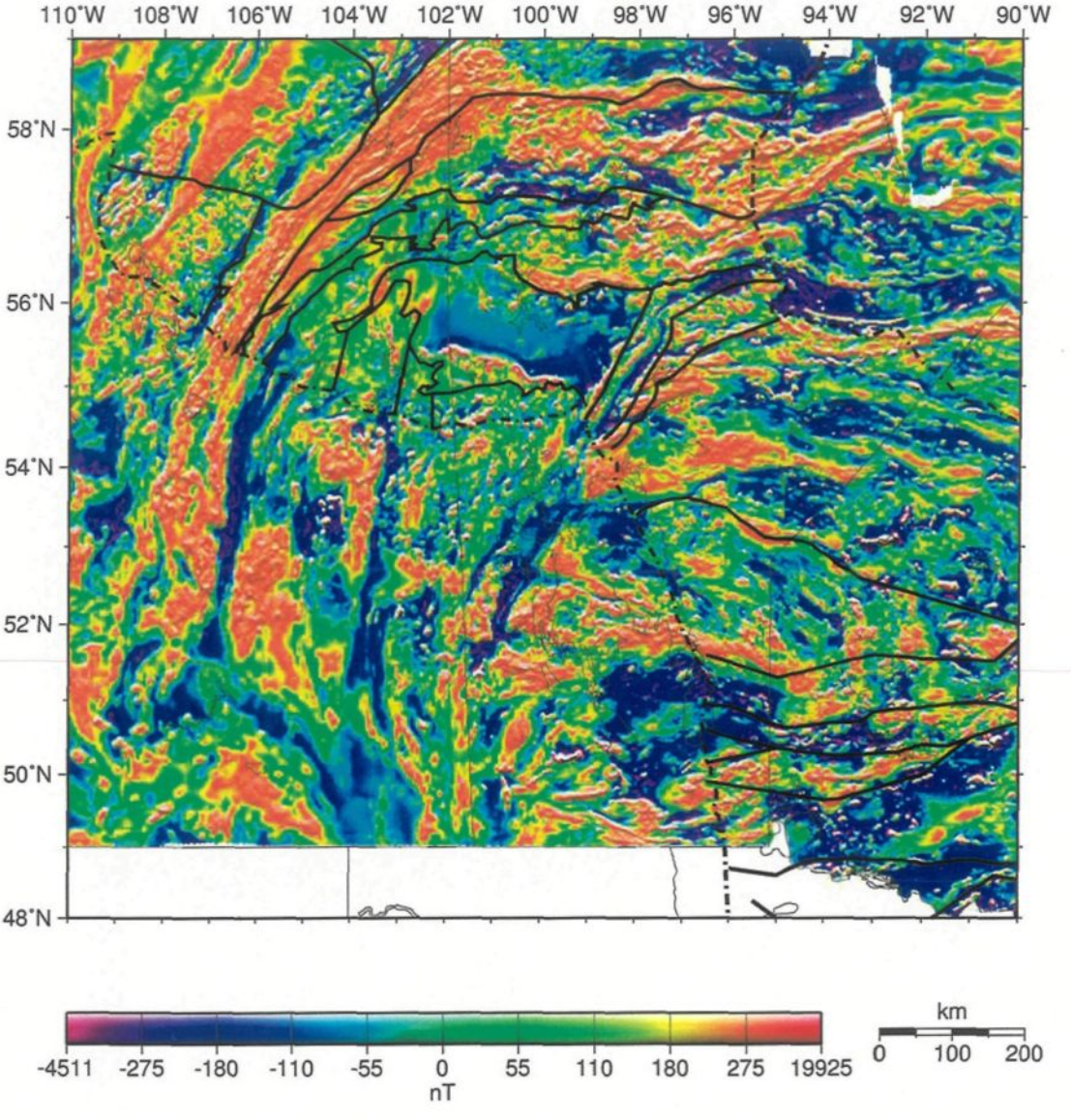
110°W
108°W
106°W
104°W
102°W
100°W
98°W
96°W
94°W
92°W
90°W
58°N
56°N
54°N
52°N
50°N
48°N
-4511
-275
-180
-110
-55
0
55
110
180
275
19925
nT
km
0
100
200

Figure 4.4: Wavelet transform of the gravity field at a scale of 20 km. The 2D second order Poisson wavelet was used. This kind of image can be interpreted as a vertical derivative map.

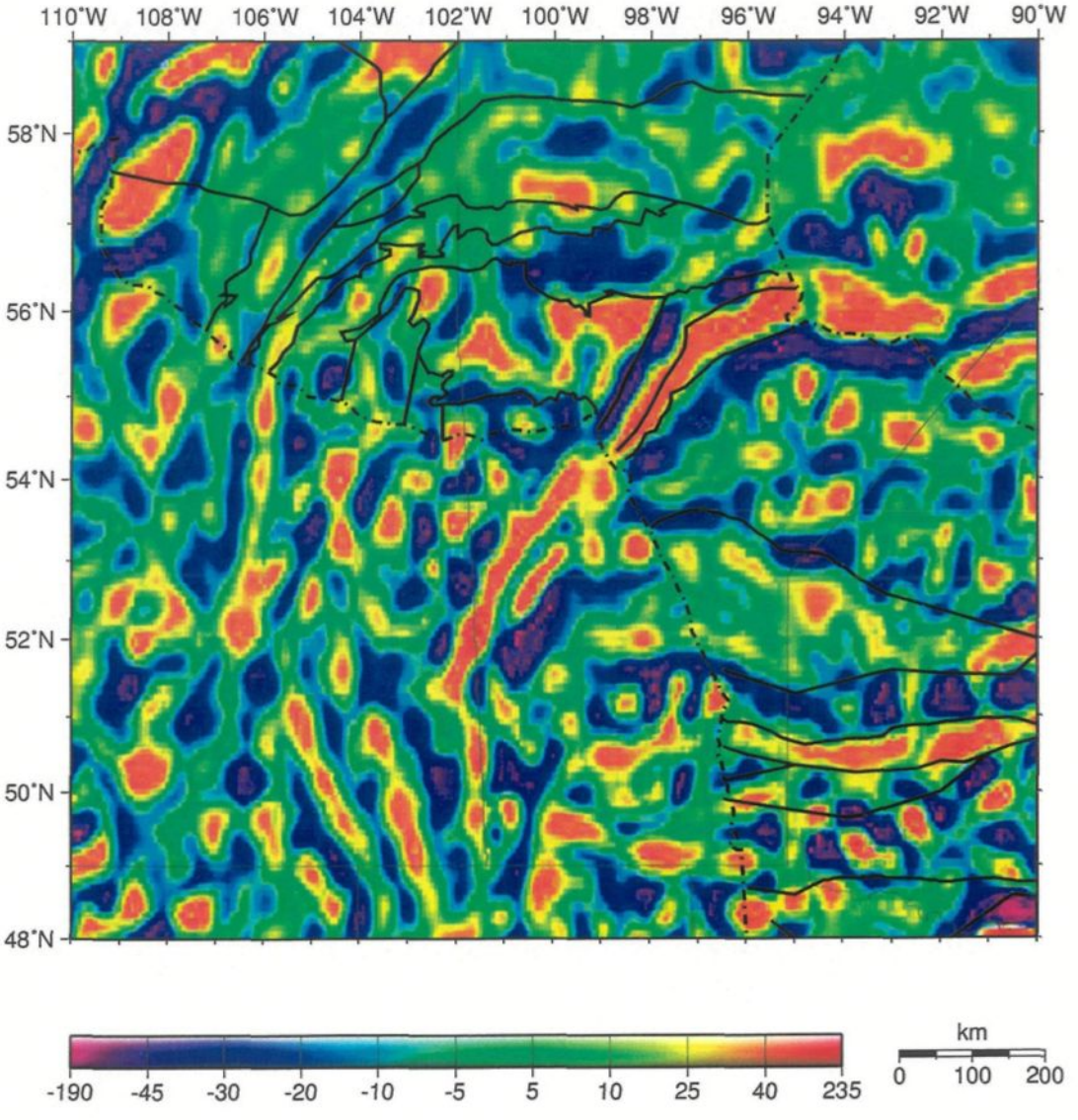
110°W
108°W
106°W
104°W
102°W
100°W
98°W
96°W
94°W
92°W
90°W
58°N
56°N
54°N
52°N
50°N
48°N
-190
-45
-30
-20
-10
-5
5
10
25
40
235
km
0
100
200

Figure 4.5: Depth to magnetic basement obtained by using Euler's method with a structural index of 0.5. Boundaries are the same as on figure 4.1.

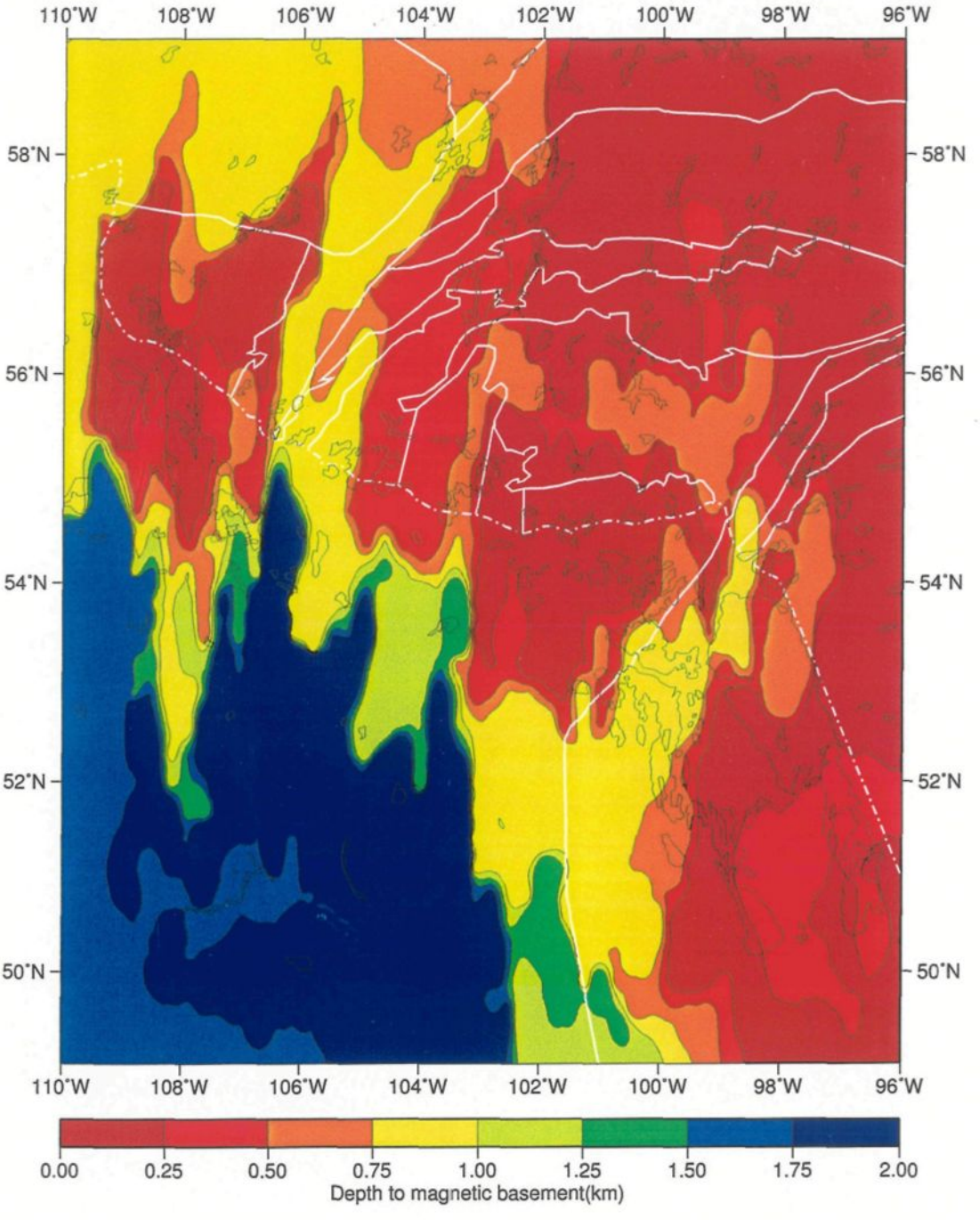
110°W
108°W
106°W
104°W
102°W
100°W
98°W
96°W
58°N
56°N
54°N
52°N
50°N
0.00
0.25
0.50
0.75
1.00
1.25
1.50
1.75
2.00
Depth to magnetic basement(km)

Figure 4.6: Wavelet analysis of gravity profile. (a) and (b) represent the real part and the phase of the wavelet coefficients The white lines represent the maxima ridge for 2 main features A and B. (c) is the gravity anomalie. (d) and (c) represent the phase of the cefficient taken along the maxima ridge. (f) shows the maximum coefficients. (g), (h) and (i) show the methods used to get the depth and the order of the source of the gravity anomaly.

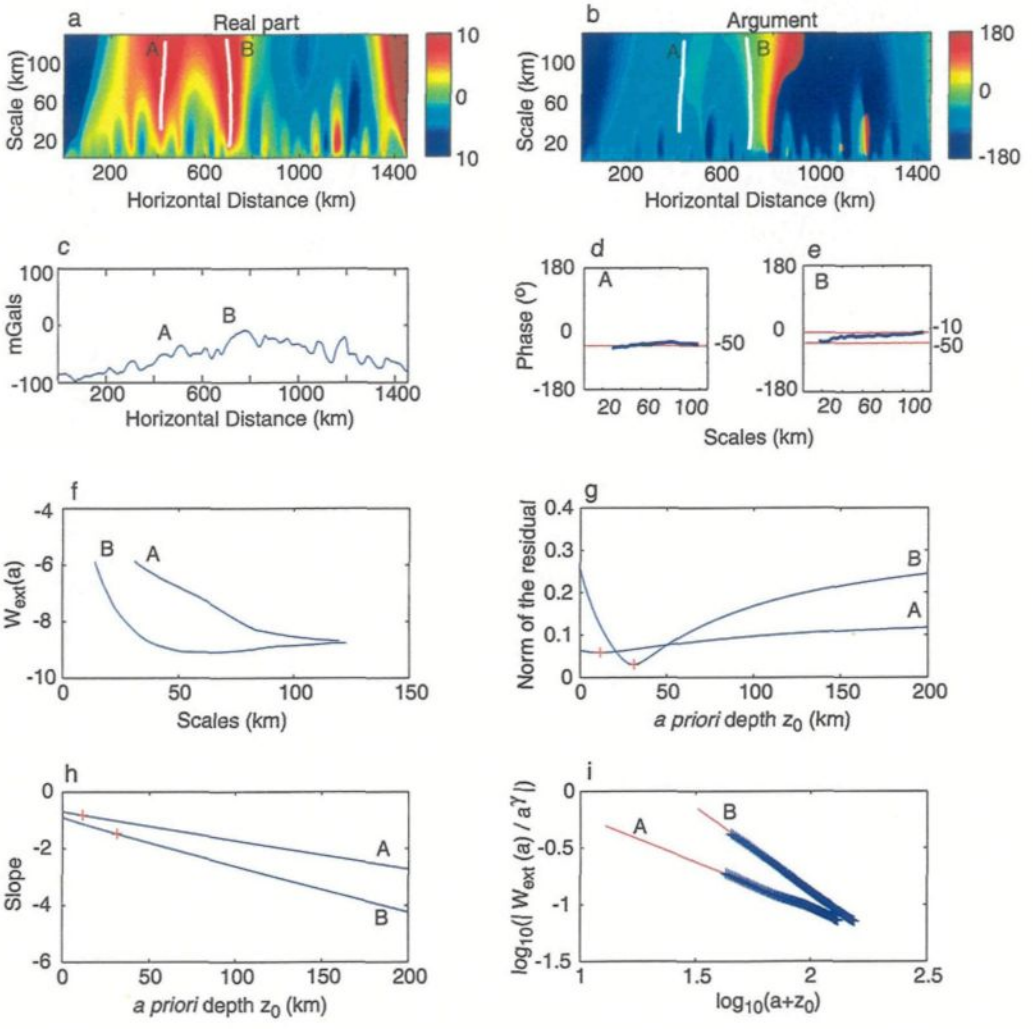
a
Real part
Scale (km)
100
60
20
A
B
10
0
10
200
600
1000
1400
Horizontal Distance (km)
b
Argument
Scale (km)
100
60
20
A
B
180
0
-180
200
600
1000
1400
Horizontal Distance (km)
c
mGals
100
0
-100
A
B
200
600
1000
1400
Horizontal Distance (km)
d
Phase (°)
180
0
-180
A
-50
20 60 100
e
180
0
-180
B
-10
-50
20 60 100
Scales (km)
f
$W_{ext}(a)$
-4
-6
-8
-10
B
A
0
50
100
150
Scales (km)
g
Norm of the residual
0.4
0.3
0.2
0.1
0
B
A
0
50
100
150
200
a priori depth z_0 (km)
h
Slope
0
-2
-4
-6
A
B
0
50
100
150
200
a priori depth z_0 (km)
i
$\log_{10}(|W_{ext}(a) / a^{\gamma}|)$
0
-0.5
-1
-1.5
A
B
1
1.5
2
2.5
$\log_{10}(a+z_0)$

Figure 4.7: Geological map of our interpretation of the potential field data beneath the sedimentary cover. The exposed geology is shown in solid color. The color coding for the geology is the same as in Figure 4.1. Our interpretation is draw in red with colored hatches: red for Archean cratons and green for the Trans-Hudson orogen.

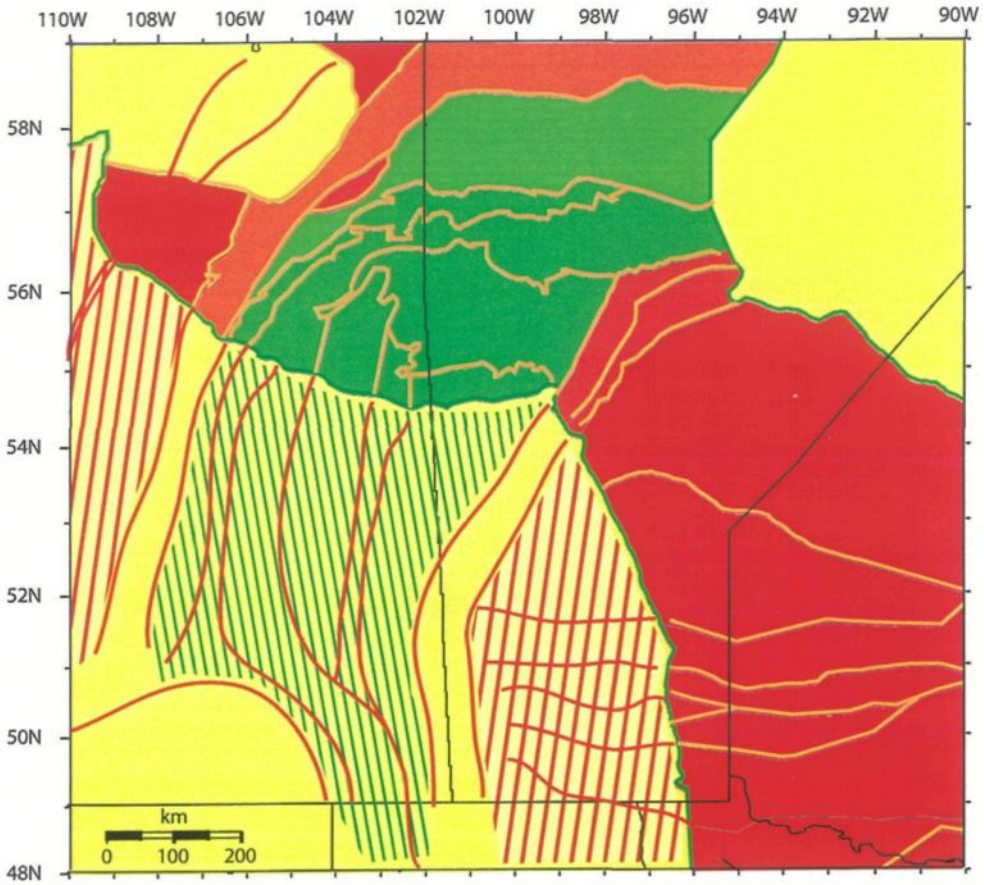
110W
108W
106W
104W
102W
100W
98W
96W
94W
92W
90W
58N
56N
54N
52N
50N
48N
km
0
100
200

Chapter 5

Elastic thickness estimation in the Eastern Canadian Shield

5.1 Geological setting and data

The study area is the eastern part of the Canadian shield between Hudson Bay and the sea of Labrador (Figure 6.1 in the next chapter). In the eastern Shield, the Superior province to the west and the Nain province to the east are separated by the southeastern Churchill province. It consists of a Core zone, mainly made of reworked Archean material, sandwiched between the New Quebec orogen to the west and the Torngat orogen to the east. To the south, the Grenville front truncates the Supe-

rior and Churchill provinces and markes the boundary with the N-E trending Late-Proterozoic Grenville province. In the south-eastern Churchill province, the main tectonic features and shear zones are NE-SW to N-S oriented. In the north-eastern part of the Superior province, most of the faults trend NW-SE. To the south, there are also faults parallel to the Grenville front, *i.e.* NE-SW. The geological structures trend mostly N-S in the southeastern Churchill province. South of the La Grande River (N54°), the subprovinces of the eastern Superior are elongated in the E-W direction.

Most of the gravity data used in this study were provided by the Geological Survey of Canada (GSC). Over Ungava Bay and Atlantic Coast, we have used satellite-derived free air gravity data from NASA and the European Space Agency (ESA) to complete the marine gravity coverage. Free air data were converted to Bouguer gravity using bathymetric data and a uniform density contrast of 1640 kg m^{-3} between rock and water. The spatial resolution of satellite data is about 20 km. On land, the average distance between measurement points varies between 10 and 20 km. The gravity data used for this study are presented in Figure 6.3 (next chapter).

The bathymetry data used originate from the *Smith and Sandwell* [1995] 2 minutes grid based on data from satellite altimetry and ship depth sounding. The topography

data are from the the U.S. Geological Survey's EROS Data Center (30-arc seconds data). Onshore and offshore data were merged together using subroutines that reduce spatial aliasing [*Wessel and Smith*, 1995]. Figure 5.1 presents the elevation data.

Both gravity and elevation data sets were projected on a kilometric grid using a sinusoidal projection with a common sampling interval of 4 km.

We have to specify several parameters for elastic thickness T_e estimation (Equations 3.2, 3.4–3.7) We assume a Young's modulus $E = 1 \times 10^{11}$ Pa, a Poisson's ratio $\nu = 0.25$. The density increases from 2780 kg m^{-3} at surface to 3350 kg m^{-3} in the mantle. These values correspond to the P-wave velocities in the crust determined for the northeastern Canadian shield [*Funck and Louden*, 1998]. We assume a constant Moho depth of 40 km for the whole area. From seismic data, it appears that this depth varies from 35 km to 45 km in eastern Canada [*Mooney and Braille*, 1989].

5.2 Estimating coherence with Fourier transform

Mapping variations in elastic thickness requires the division of the study area into subregions. We extracted subgrids of 128 × 128 points. They cover 508 × 508 km^2

area. This size corresponds to one half of the width of the data set (oceanic areas excluded) and one fourth of its heigth. We chose this size after several trials. We have to compromize between the number of subgrids we can extract and the wavelengths we need to get the transition from compensated to uncompensated topography. All grids have the same orientation in our map projection. The distance between the subgrid centers is about 128 km. No attention was given to the geological setting in disposing centers. We have tried to include as little oceanic areas as possible. We used the coherence method as described in Chapter 3 because coherence curves are not affected much by the load, contrarily to the admittance curves. We assume equal surface and subsurface loads (*ie* $f = 1$) to compute the predicted coherence.

Figure 5.2 shows the elastic thickness map. It includes *Pilkington*'s [1991] T_e values. He used the FFT method but over larger areas. Over the whole area except the shore, we obtain high T_e values generally larger than 50 km. Elastic thickness variations fit more or less the regional geologic pattern. It may be related to the presence of faults or major geological boundaries and to crustal composition variations. The Superior craton is characterized by high values of T_e (more than 70 km) as previously documented by *Wang and Mareschal* [1999]. The south-eastern Churchill province has T_e values of $\approx$ 50 km. The Grenville front is marked by relatively small

T_e values ($\approx$ 30 to 50 km) on its northern side. There is no clear geographic trend relating T_e to the distance of the edge of the craton. The presence of both high and low values of T_e near the shore line may be an artifact of the presence of both oceanic and continental data.

5.3 One dimensional coherence from wavelet transform

We analyzed 1D-profiles to determine global wavelet coherence on several profiles across the area and compared it with Fourier coherence. Global wavelet coherence curves are smoother than Fourier coherence curves because of the averaging method. We averaged coherence curves from profiles with different azimuths (from 0° to 170° with a step of 10°). We defined an azimuth-average transition wavenumber for a coherence of 0.6. This wavenumber corresponds to the flexure of the theoritical coherence curve and to the maximum of the admittance curve in the case of internal loading. The azimuth-average transition wavenumber between coherent and incoherent gravity and topography, which is related of the flexural rigidity, is presented on Figure 5.3. The area is characterized by low values of transition wavenumbers related to high values of T_e. The resulting pattern is different from that obtained with FFT

method. The Grenville province seems to be more rigid than the Superior province, which shows low values near the Richmond Gulf. It coincides with the positive satellite magnetic anomaly of Ungava peninsula. The source of this anomaly has been associated with the Richmond Gulf aulacogen [*Chandler and Schwarz*, 1980]. The south-eastern Churchill subprovince is relatively weak compared to the other parts of the area. A weaker zone is also noticeable north to the Grenville front.

Rose diagrams of the transition wavelength are shown in Figure 5.4. In the Grenville province, the pattern is more isotropic than in other regions. There may be a light trend of the weakness directions perpendicular to the Grenville front to the west and a NNE trend to the east. South of N56° , the Superior province is characterized by NE elongated roses. The north-eastern Superior province show EW to NE elongated roses. These directions of anisotropy in the Superior are difficult to interpret. They are aligned with the faults and the boundary between subprovinces. They are perpendicular to the Tasiat-Allemand structural zone in the north and Témiscamie-Corvette structural zone in the south. These structural zones were defined by *Hocq et al.* [1994] and *Moorhead et al.* [2000]. They are locally defined by faults, aeromagnetic lineations or graben shaped sedimentary basins. On the transition wavelength map, the Tasiat-Allemand structural zone corresponds to a weaker

lithosphere.

5.4 Conclusions

The main conclusion is that the elastic thickness is high (> 50 km) throughout the eastern Canadian shield. This is supported both by Fourier and wavelet based methods. A weaker region is found north of the Grenville front tectonic zone. It is better seen on the FFT map but there are scan also be seen on the CWT map. In the Grenville province, the rigidity is more isotropic compared to the SE Churchill and the Superior provinces. In the SE Churchill province, the lithosphere is weaker in the direction perpendicular to the structures and faults. In the Superior province, the rigidity is highly anisotropic and maximum in the NE direction. It may be linked with the orientation of the subprovinces or major faults which are NE trending too. We notice that the weak zone near the Torngat orogen and the other north to the Grenville front, present on both map, are coinciding with the location of kimberlite fields of the Torngat and Otish respectively.

Figure 5.1: Elevation map of eastern Canada.

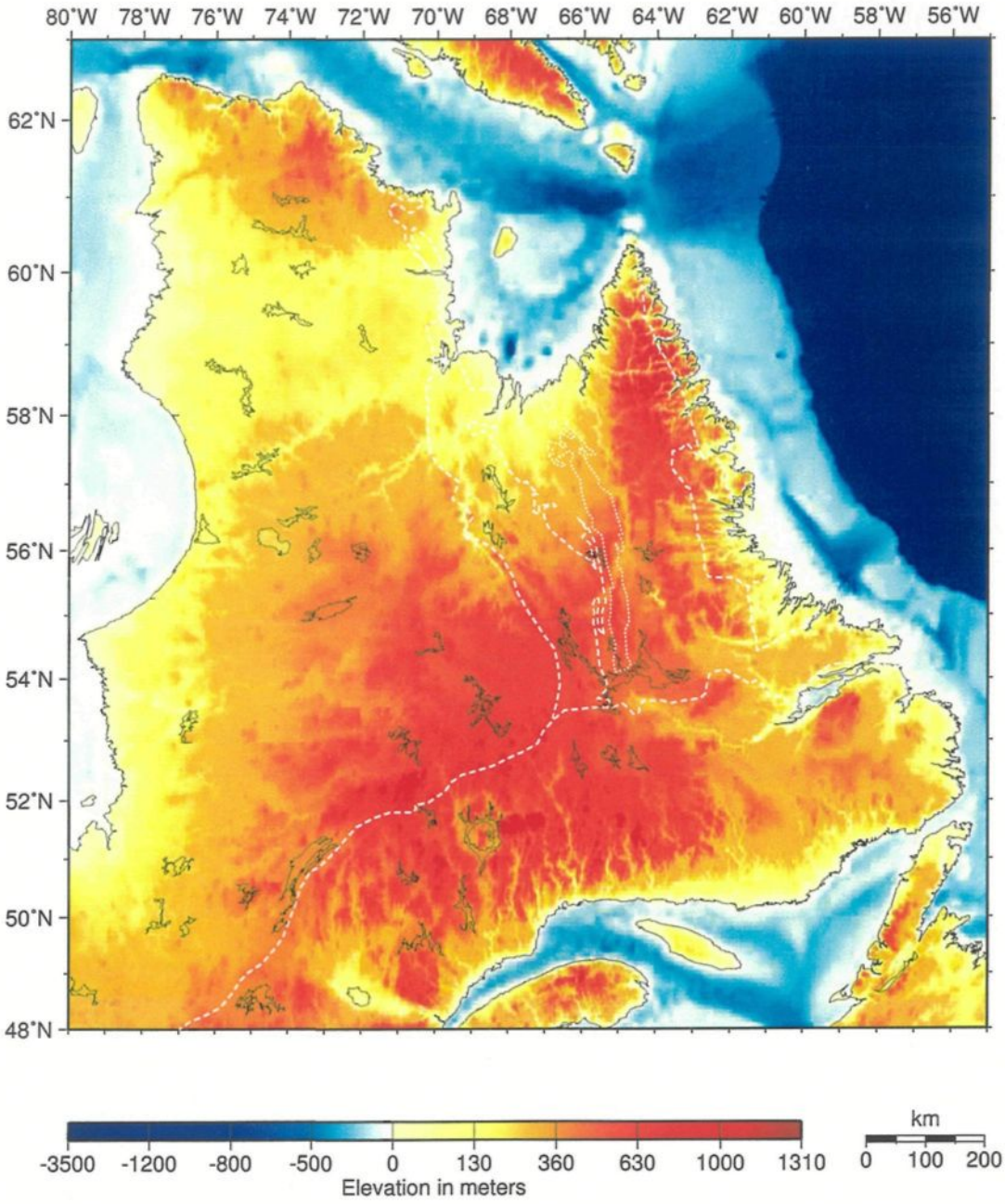
80°W
78°W
76°W
74°W
72°W
70°W
68°W
66°W
64°W
62°W
60°W
58°W
56°W
62°N
60°N
58°N
56°N
54°N
52°N
50°N
48°N
-3500
-1200
-800
-500
0
130
360
630
1000
1310
Elevation in meters
km
0
100
200

Figure 5.2: Elastic thickness map of eastern Canada from FFT results. White circles show the locations of the subgrid centers. Black circles are used to indicate Pilkington's [1991] T_e values.

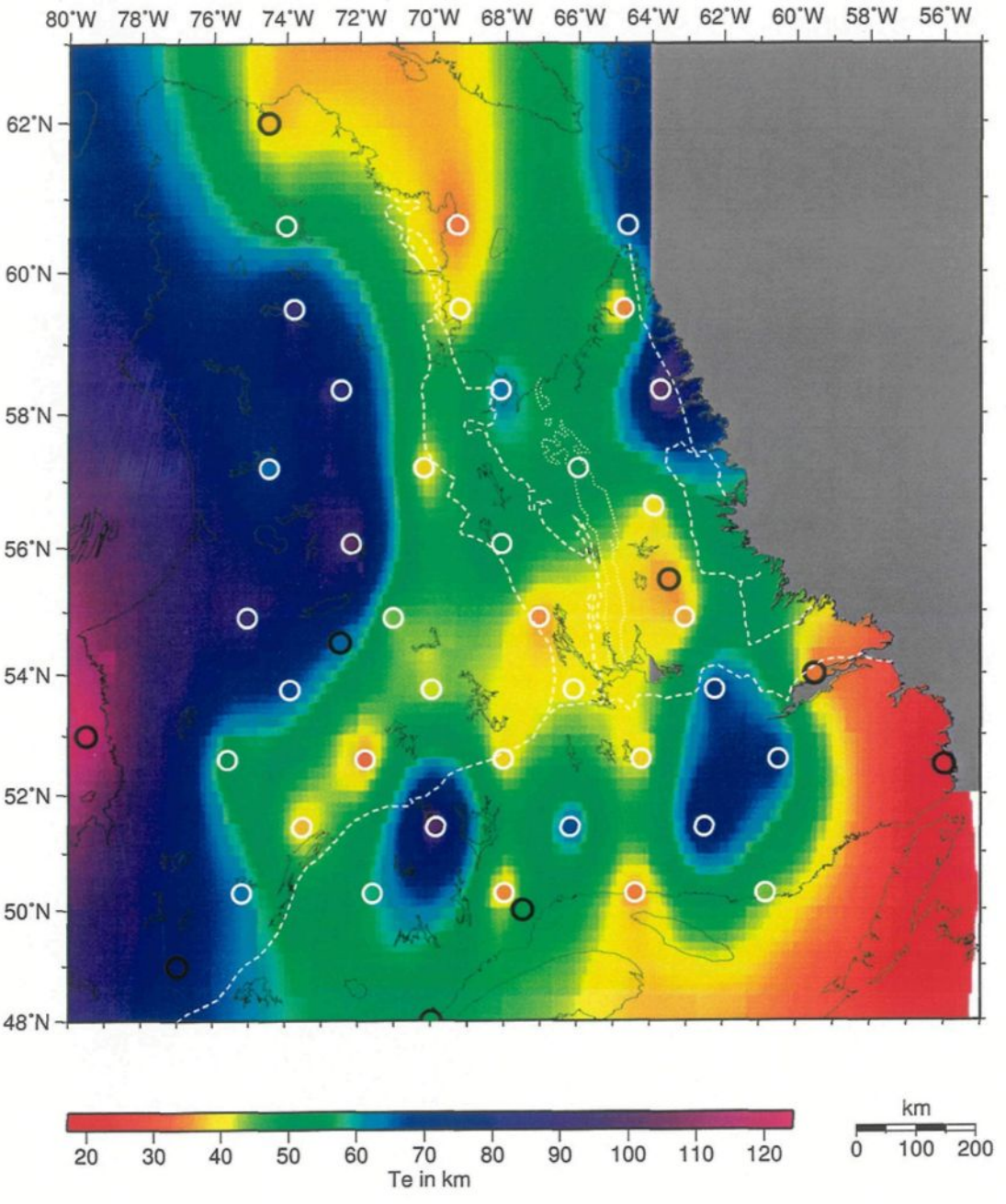
80°W
78°W
76°W
74°W
72°W
70°W
68°W
66°W
64°W
62°W
60°W
58°W
56°W
62°N
60°N
58°N
56°N
54°N
52°N
50°N
48°N
20
30
40
50
60
70
80
90
100
110
120
Te in km
km
0
100
200

Figure 5.3: Transition wavenumber map of eastern Canada from CWT results. Crosses indicate the locations of measurement.

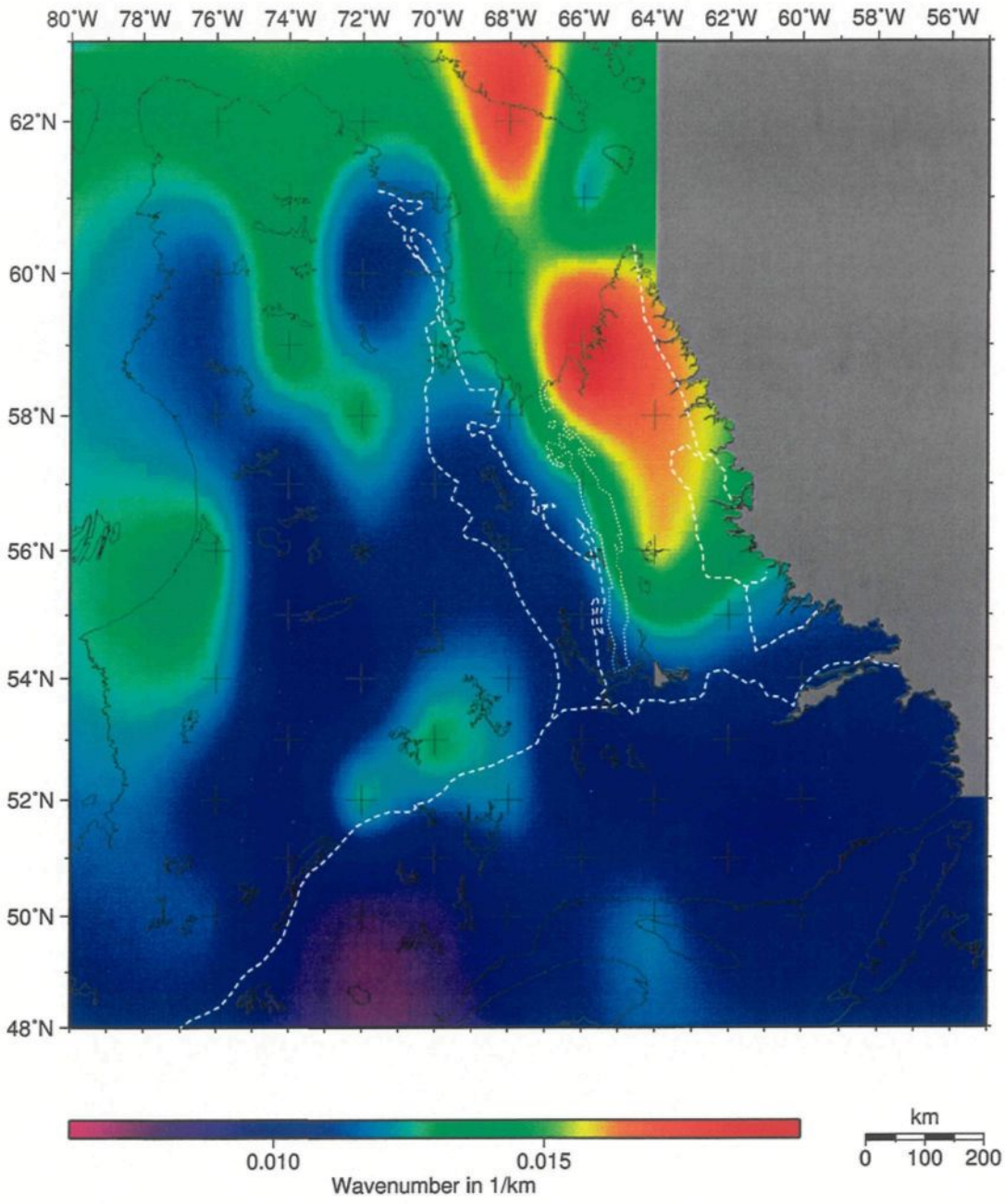
80°W
78°W
76°W
74°W
72°W
70°W
68°W
66°W
64°W
62°W
60°W
58°W
56°W
62°N
60°N
58°N
56°N
54°N
52°N
50°N
48°N
0.010
0.015
Wavenumber in 1/km
km
0
100
200

Figure 5.4: Rose diagrams of transition wavenumbers from compensated to uncompensated topography of CWT coherence. Background map is the Bouguer gravity anomaly used for the calculation.

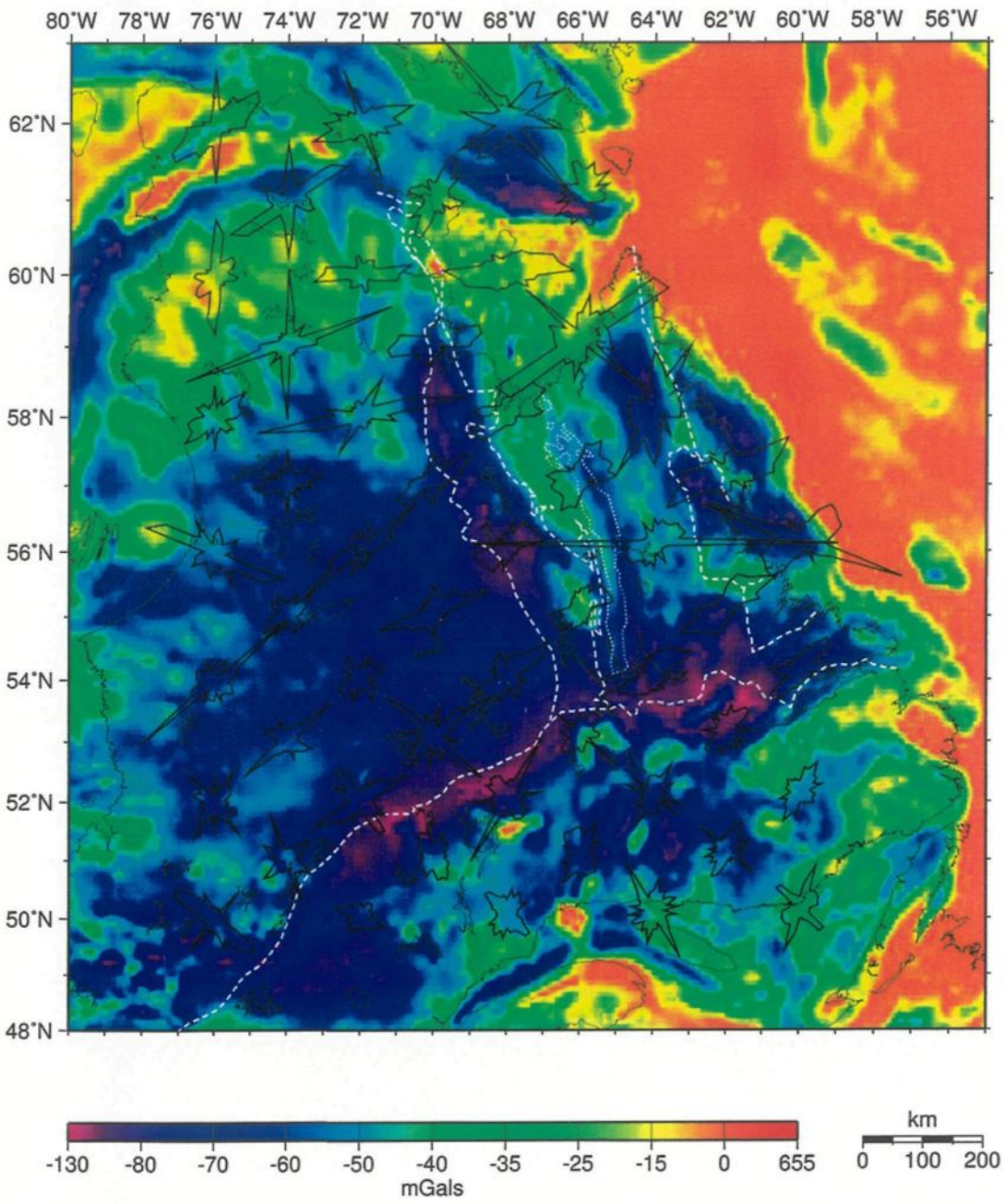
80°W
78°W
76°W
74°W
72°W
70°W
68°W
66°W
64°W
62°W
60°W
58°W
56°W
62°N
60°N
58°N
56°N
54°N
52°N
50°N
48°N
-130
-80
-70
-60
-50
-40
-35
-25
-15
0
655
mGals
km
0
100
200

Chapter 6

Geophysical Correlations in the Ungava Bay Area

Published in CJES. [1]

Abstract

We used gravity and magnetic data to extend geological features, across Ungava Bay and Hudson Strait, from northern Quebec and Labrador to Baffin Island. Tectonic domains identified on land were extended offshore by visual inspection of the

[1] E. Bourlon, J.C. Mareschal, W.R. Roest, and H. Telmat, 2002, Geophysical correlations in the Ungava Bay area, *Canadian Journal of Earth Sciences*, 39(5):625-637.

potential fields. The boundaries identified on colour shaded relief maps were drawn on the original marine magnetic profiles to verify the robustness of the conclusions. Our interpretation in Ungava Bay remains speculative but gives some insight into the architecture of the north-eastern Canadian shield. Onshore, where trends are well marked, the magnetic fabric of the Superior province reappears east of the New Quebec orogen in the western core zone. Geochronology and geochemical data also suggest the affinity of the western core zone with the Superior province. On the gravity map, the New Quebec orogen appears to vanish offshore. A major trend in magnetic and gravity gradients can be followed offshore possibly as far north as Hudson Strait. It has been identified as the extension of the George River and Moonbase shear zones. The de Pas batholith is associated with a linear trend west of this shear zone. To the east, several features appear distinctly on the magnetic map. A narrow NW-trending anomaly can be followed from Quebec all the way to Baffin Island. On land, this feature marks the western limit of the Lake Harbour group. Two wide N-trending bands that can be followed from the Torngat orogen all the way to Baffin island are interpreted as the extensions of the Lac Lomier complex and Tasiuyak domain.

6.1 Introduction

The welding together of several Archean cratons during the Paleoproterozoic was an important step in the final assembly of the Canadian Shield [*Hoffman*, 1988]. In eastern Quebec and Labrador, the Superior and Nain provinces are separated by the southeastern Churchill province (Fig. 6.1). This part of the Churchill province consists of a block of mainly Archean crust, the Core zone, that was trapped between the Superior and the North-Atlantic cratons when they collided together [*Wardle and VanKranendonk*, 1996]. This core zone is sandwiched between two transpressional orogens. The west verging New Quebec orogen (NQO) separates it from the Superior province to the west. A dextral shear zone, the Ashuanapi river shear zone, marks the eastern boundary of the New Quebec orogen in the south; in the north, the Lac Tudor shear zone and the Lac Turcotte thrust are the proposed boundary of the NQO [*Girard*, 1990; *Perreault and Hynes*, 1990]. The doubly verging Torngat orogen separates the core zone from the Nain province to the east. The Torngat is located between two sinistral shear zones: the Abloviak to the east and the Falcoz shear zone to the west. Strong negative Bouguer gravity anomalies are associated with both orogens, suggesting some crustal thickening [*Mareschal et al.*, 1990; *Funck and Louden*, 1999; *Funck et al.*, 2000]. In the core zone, the main tectonic features

are several major shear zones and the de Pas batholith, possibly an Andean type batholith [*Thomas and Kearey*, 1980]. The shear zones are dextral in the western part of the core zone, and sinistral to the east (east of the George River shear zone). The opening of the Labrador sea, at ca. 90 Ma, has separated the Nain province in eastern Canada from the rest of the North Atlantic craton in Greenland.

Rocks exposed in the southern part of Baffin Island, of Archean and Paleoproterozoic ages, presumably belong to the Churchill province and could be related to the Churchill province in north-eastern Quebec and Labrador [*Jackson and Taylor*, 1972; *Hoffman*, 1990].

At the northern tip of Quebec, the Ungava orogen (Cape Smith foldbelt) separates the Superior and Rae Archean provinces. In contrast with the New Quebec orogen, the Ungava orogen contains juvenile Proterozoic crust, possibly formed during the rifting of a microcontinent from the Superior craton [*St-Onge et al.*, 2000]. Many relationships between these different orogens in Labrador, north-eastern and northern Quebec, and on Baffin Island are concealed because geological features cannot be followed beneath Ungava Bay and Hudson Strait.

Marine seismic data were acquired in Ungava Bay and along the coast of Labrador by the eastern Canadian Shield onshore-offshore transect of LITHOPROBE (ECSOOT). The objective of the transect is to determine the tectonic processes that have formed the orogenic structures of the region and the differences between orogens that brought together preexisting Archean blocks and those that incorporated younger material. In order to help in the interpretation of the seismic data obtained in Ungava Bay and their correlation with geological features observed on land, *Telmat et al.* [1999] used gravity data to delineate the offshore continuation of the geological features south of the Ungava Bay, in particular the George River shear zone and the de Pas batholith. In this chapter, we shall use a combination of gravity and magnetic data to extend across Ungava Bay and Hudson Strait some of the main geological features observed to the south, and to try and correlate the different parts of the Churchill province in Labrador, north-eastern Quebec, and Baffin Island.

6.2 Potential field data and processing

Most of the magnetic and gravity data used in this study were provided by the Geological Survey of Canada (GSC). We used satellite derived gravity data from NASA and the European Space Agency (ESA) to supplement the offshore gravity

coverage. Both magnetic and gravimetric data were placed on a 2' (≈4km) grid for processing and imaging.

6.2.1 Magnetics

Regional aeromagnetic data from the National Aeromagnetic Database of the GSC were acquired along flight lines with 800 m spacing and were leveled to an altitude of 305 m. We have also used shipborne magnetic data from the GSC [*Verhoef et al.*, 1996] to cover most of the marine areas. The irregular sampling and the variable depth to the magnetic basement results in variable resolution in the marine data. Near the shores of Ungava Bay, there is a gap between the shipborne and aeromagnetic coverage. This gap was filled by interpolating between the different data sets. This interpolation was performed with an adjustable tension continuous curvature surface gridding algorithm [*Smith and Wessel*, 1990; *Wessel and Smith*, 1995]. The data were put on a 2' grid and low pass filtered to retain wavelengths larger than 10 km and eliminate those shorter than 5 km. A color shaded relief map of the magnetic data set is shown in Fig. 6.2.

6.2.2 Gravity

Gravity data were also obtained from the GSC. We have combined Bouguer gravity data on land with free-air gravity values offshore. Over Ungava Bay, where there is a gap in marine gravity measurements, we have used satellite derived gravity data [*Smith and Sandwell*, 1995]. The satellite data were derived from a combination of the ERS-1 satellite altimeter and the GEOSAT geodetic mission data. These data are provided on a 2' grid although the spatial resolution of the satellite data (≈20 km) is much lower than the grid sampling. With the average distance between data points varying between 10 and 20 km, the resolution of land data is quite variable in this region and lower than grid sampling. The distribution of land is presented by *Telmat and Mareschal* [1996]. We combined and interpolated the data on 2' grid with subroutines that reduce spatial aliasing [*Wessel and Smith*, 1995].

The gravity data are presented as a color image, draped over a shaded relief image of aeromagnetic data (Fig. 6.3). The shaded relief image is generated by calculating a normalized directional horizontal derivative of the magnetic field, here in the N210° azimuthal direction. This gradient is superimposed on the color gravity map by modulating the color saturation with the gradient intensity. The composite map suggests magnetic and gravity correlations which can be associated with geological

features.

6.3 Regional Magnetic field map

6.3.1 Magnetics

Because the magnetic field is a dipole field, it is relatively more sensitive to shallow sources than the gravity field. In addition, short wavelengths are not identified in the gravity data because of the large sampling distance. As a result, the magnetic map contains more short wavelength anomalies and shows more detailed features than the gravity map. Magnetization is principally a function of magnetic mineral content and is affected by metamorphism and alteration. It is not directly related to lithology but we can correlate its patterns with known geology [*Kane and Godson*, 1989]. This is clearly seen by comparing Fig. 6.2 with Fig. 6.1.

On land, the Superior and Churchill provinces (in Quebec and Labrador as well as Baffin Island) have very distinctive magnetic lineations. In Quebec and Labrador, the Tasiuyak domain is clearly identified and coincides with a low NNW trending anomaly. To the west of the Tasiuyak domain, a magnetic high corresponds to the Lac Lomier complex. The three main parts of the Lake Harbour group are well

defined by a magnetic low. The Falcoz and Moonbase shear zones are marked by some shifts in the lineations. The de Pas batholith coincides with a magnetic high in the south. This anomaly vanishes to the north although the batholith remains exposed, possibly because of compositional differences between the north and the south [*Martelin et al.*, 1998]. West of the Core zone and in the NQO, the lithology is poorly correlated with the magnetics but many faults in the NQO are outlined by high amplitude lineations. The pattern of magnetic highs in the western half of the NQO might suggest the presence of Superior basement under the metasediments and the limits of its extension. Between N56.5° and N58° , the magnetic patterns of the Superior province seem to reappear east of the Lac Tudor shear zone in the western core zone. Presence of remobilized Archean crust in this area is confirmed by isotopic analysis [*Isnard et al.*, 1998]. The magnetic lineations seem to support the suggestion that Archean rocks west of the Lac Tudor shear zone represent a block incompletely rifted from the Superior craton at 2.2 Ga [*James and Dunning*, 2000]. An alternative possibility is that rifting occured east of these Superior like fragments and that these distal edges have been thrusted upward and perhaps transported lengthwise during the Rae collision. A similar interpretation for the Cape Smith belt was proposed by *Hoffman* [1985]. North of the exposed NQO, a band of magnetic lows seems to define a continuous boundary on land all the way to the Cape Smith belt. This band might

mark the region where magnetization was reset during peak metamorphism.

The resolution of the magnetic data decreases offshore. This is due in part to the low density of the marine surveys, in part to the greater depth to the magnetic basement in the Bay and Hudson Strait. Nonetheless, several magnetic trends are not affected and are continuous across Hudson Strait.

6.4 Composite Gravity and Magnetic map

On land, the New Quebec orogen, consisting of low-grade sedimentary and mafic volcanic rocks, coincides with the largest and most negative anomaly north of the Grenville Front (with Bouguer gravity values lower than -90 mGal). This anomaly is possibly due to crustal thickening, the lower density of the metasediments, or a combination of these factors [*Kearey*, 1976; *Mareschal et al.*, 1990]. The gravity low appears to vanish to the north at the latitude $\approx$ N60° and it can not be connected with the paired gravity anomaly of the Ungava orogen [*Thomas and Gibb*, 1977].

The western core zone, consisting mostly of Archean paragneisses, is characterized by a relative Bouguer anomaly high (around -30 mGal) interpreted as due to crustal

thinning. Modeling of the gravity profiles shows thickness increases from 38 km in the Superior province to more than 43 km beneath the NQO then decreases to 37 km beneath the western core zone [*Telmat et al.*, 1999]. The Doublet zone, between N55 ° and N56 ° in the eastern part of the NQO, is associated with a one of the highest anomalies in the area (-20 mGal). This zone consists of a volcano-sedimentary pile at least 6 km thick [*Wardle and Bailey*, 1981]. The de Pas batholith does not have a well defined gravity signature. Gravity is higher on the western side of the batholith than on the eastern side. The axis of a gravity low on the eastern boundary coincides with the George River shear zone. This short wavelength north-west trending gravity low can be followed beyond the northern limit of the exposed batholith. The cause for the gravity low on the shear zone is not elucidated yet but the effect of melting during the intense deformation has been evoked [*Telmat et al.*, 1996].

The gravity low associated with the Torngat orogen has often been interpreted as due to crustal thickening [e.g., *Thomas and Kearey*, 1980]. This interpretation is consistent with the seismic interpretation suggesting that a deep crustal root (more than 49 km) has been preserved [*Funck and Louden*, 1999; *Funck et al.*, 2000]. A positive anomaly coincides with the Tasiuyak domain. The Tasiuyak domain has been interpreted as an accretionary prism. Gravity modeling suggests a maximum

thickness of 13 km [*Feininger and Ermanovics*, 1994]. The Abloviak shear zone coincides with a strong gradient along the boundary between the Torngat orogen and the Tasiuyak domain. The gravity high of the Burwell terrane has been interpreted as due to higher crustal density rather than to crustal thinning [*Seguin and Goulet*, 1990].

The gravity anomalies could not be followed offshore further north than Hudson Strait where any north-west trending gravity anomaly is overprinted by an east-west trending very negative free air anomaly. This anomaly is likely due only to the deeper water level and sediment fill. There is no sign of crustal thinning and volcanic activity related to the graben formation during the opening of the Labrador Sea.

6.5 Proposed geological boundaries over Ungava Bay and Hudson Strait

Scott and St-Onge [1998] have suggested that geological boundaries found on both sides of Ungava Bay can be traced with magnetic data beneath the water cover and they have established correlations between geological units on Baffin Island and in eastern Quebec and Labrador. In this section, we intend to examine the detailed

magnetic map that we shall discuss with the original shipborne magnetic data. We shall also use the vertical gravity gradient to delineate some boundaries. This analysis is necessary to ascertain the robustness of the conclusions that can be drawn from the potential field data.

6.5.1 Magnetics

The detailed magnetic map of Ungava Bay, Hudson Strait, and surrounding land regions is shown on Fig. 6.4. We have superposed a few lines to mark a few important tectonic boundaries mapped on land and their extensions beneath the Bay. The westernmost line represents the edge of the Superior province. The eastern limit of the NQO has been traced on land but can not be extended beneath Ungava Bay. It is seen again on land between N60° and N60.5° . East of the NQO, a relatively narrow triangular block is characterized by well defined EW trending magnetic anomalies with a pattern similar to that of the Superior province. The trends take a northerly directions east and west of this "western core zone" block. The similarity in the regional magnetic fabrics east and west of the NQO provides some support for the model by *James and Dunning* [2000]. The EW trending magnetic anomalies can not be followed offshore, which likely results from the insufficient density of the marine magnetic data. Therefore, we can not determine the extent of Superior basement

beneath the western Ungava Bay.

A series of magnetic highs along a NNW trend can be traced to at least N60° and possibly further. This trend might coincide with the northward extension of the George River and Moonbase shear zones. It vanishes North of N61° . The Falcoz shear zone can not be extended beneath Ungava Bay. We have interpreted a linear NW trend of magnetic highs across the Bay as the extension of the Abloviak shear zone. North of 60° , we have identified two branches. On Baffin Island, the westernmost branch marks the eastern edge of the Lake Harbour group that might be continuous across the Bay. The eastern branch marks the eastern limit of exposure of "Narsajuaq Arc" type rocks. This interpretation suggests continuity of the Lake Harbour group between Quebec and Baffin Island. "Narsajuaq Arc" crust is confined between the two branches and does not extend south of Hudson Strait. A wide, north-trending, positive anomaly is also well marked across the Bay. We have interpreted this anomaly as the extension of the Lac Lomier complex, which shows as a prominent positive anomalies in Labrador, that can be followed along the eastern shore of Baffin Island. The interpretation of the wide band of negative anomalies to the east is slightly more ambiguous because of possible effects of the opening of the Labrador Sea. Our interpretation is that the entire band is the northern extension of

the Tasiuyak domain. This band extends northward in the western part of Frobisher Bay. On land, the offset of the Lac Lomier complex and Tasiuyak domain by the Abloviak shear zone is perfectly marked on the magnetic map.

Because the interpretation is based on widely spaced ship tracks, we have verified our interpretation by comparison with the original magnetic profiles (Fig. 6.5). The profiles show clearly that the interpreted lines connect anomalies on different ship tracks. However, the ambiguity regarding the eastern limit of the Tasiuyak domain north of Torngat remains.

6.5.2 Vertical gravity gradient

Over Ungava Bay, the gravity anomaly is slightly higher than onshore (5 to 10 mGal). Note that Bouguer anomalies over the Bay are even more positive than the free-air because of the water cover (less dense than rocks). Some linear trends of the onshore domain can be followed offshore. This is better shown on the vertical gradient map that we have calculated over Ungava Bay to compare with the magnetic interpretation (Fig. 6.6). Gradient maps have been widely used to delineate boundaries between different provinces or terranes. Although the horizontal gravity gradient is used more often [e.g., *Sharpton et al.*, 1988], the vertical gravity gradi-

ent is also sensitive to discontinuities [e.g., *Marson and Klingele*, 1993; *Blakely and Simpson*, 1986]. We prefer the vertical gradient because it is directly comparable to the magnetic field. The vertical gravity gradient anomalies have the same property as the magnetic anomalies that are always highest near discontinuities in magnetization. If magnetization and density were proportional, the vertical gravity gradient map would be identical to the magnetic field as observed at the magnetic pole, i.e., with a vertical magnetization. Vertical derivatives enhance the shorter wavelength anomalies and are more sensitive to sources closer to the surface.

To reduce the effect of the varying resolution on the calculation of the vertical derivatives, we have first applied a band pass filter to the gravity data, eliminating wavelengths shorter than 10 km and larger than 120 km and retaining those between 20 km and 110 km. Although the short wavelengths are enhanced relative to the gravity map, the resolution of the vertical gravity gradient map remains limited by the low density of the gravity data. Nonetheless, discontinuities appear more clearly on the gradient than on the gravity map.

On the gradient map, the major zones of the NQO can be distinguished. The eastern and western borders of the orogen are marked by a positive and negative gra-

dients respectively. Between them, the volcanic belt is outlined sketchily by a positive gradient. In the south-western bay, the gravity gradient defines a series of positive anomalies that can be connected and that we interpret as the extension of the eastern limit of the NQO. On land, the western core zone also appears distinctly on the vertical gradient map. The line following the trend of positive magnetic anomalies appears as joining isolated positive gravity gradient anomalies. Parallel and ≈20 km east of the magnetic trend, a series of negative gravity gradients is clearly defined on the map. This trend was interpreted by *Telmat et al.* [1999] as the extension of the George River and Moonbase shear zones. This interpretation was supported by detailed land gravity measurements made for this purpose [*Telmat et al.*, 1999]. We have retraced the corresponding line on the vertical gradient map. A series of positive anomalies, ≈ 20 km east of the interpreted George River shear zone, defines another northward trend that cannot be followed beyond Hudson Strait.

To the east, some anomalies appear on both sides of Hudson Strait. On land, the Lake Harbour group, the Lac Lomier complex, and the Tasiuyak domain are well marked. The pattern of the vertical gravity gradient in the southeastern region of Ungava Bay, in the eastern part of Baffin Island and in Frobisher Bay is consistent with our interpretation of the magnetic data.

6.6 Conclusions

Most of the differences between evolutionary models for the region lie in the relationship between the core zone and the Superior province. At one extreme, some models consider that Superior crust extends all the way to the Torngat orogen [*James et al.*, 1998]. At the other end, some models consider the core zone as an Archean block independent from the Superior, possibly part of the Rae province [*Hoffman*, 1988, *Wardle and van Kranendonck*, 1996]. In order to summarize our interpretation, we have superposed on the geological map of Ungava Bay and surrounding land regions the shading of the magnetic relief and the main features interpreted from the magnetic and vertical gravity gradient maps (Fig. 6.7). Because our interpretation differs somehow from that of *Scott and St-Onge* [1998], we have also traced their proposed boundaries on the map.

- From the vertical gravity gradient map, we have delineated a series of gravity highs in south-western Ungava Bay. These highs form a trend that can be connected to the eastern edge of the NQO on land. On land, the western core zone has a magnetic fabric similar to that of the Superior province and a well defined signature on the gravity gradient map. Its limits are well marked on the gravity gradient but not so well on the magnetic map. The direction of magnetic

lineations changes east and west of these limits but they do not appear as strong discontinuities on the magnetics. The conventional eastern limit of the NQO is well marked on the gravity gradient but not on the magnetic map that shows no major discontinuity with the western core zone.

- A NNW-trending magnetic high is followed as far north as N60° . It is ≈20 km west of the negative gravity gradient that had been interpreted as the offshore continuation of the George River shear zone [*Telmat et al.*, 1999]. *Scott and St-Onge* [1998] have traced this boundary across Hudson Strait and back to the Cape Smith Belt. Their interpretation might be correct but neither the magnetic, nor the gravity anomalies can be traced across Hudson Strait. The potential field data suggest that this is a major tectonic boundary. *Scott and St-Onge* [1998] assume that this boundary marks the eastern limit of Superior type crust in the core zone and Ungava Bay. Alternatively, from the potential field data, Superior crustal origin could be restricted to the basement of the NQO and the western core zone. This small block, presumably rifted from the Superior province, likely does not extend very far beneath the Bay or eastward of W67° . The origin of the eastern part of the core zone can not be elucidated by the potential field data.

- A well defined and narrow NW trend of magnetic highs crosses the Bay and Hudson Strait. It divides in two branches over Hudson Strait. The west branch connects to the eastern limit of the Lake Harbour group on Baffin Island. The east branch marks the eastern limit of exposure of "Narsajuaq Arc" type rocks. Our interpretation suggests continuity of the Lake Harbour group between Quebec and Baffin Island. "Narsajuaq Arc" crust is confined between the two branches and does not extend south of Hudson Strait. *Scott and St-Onge* [1998] have assumed that magnetic highs on the map coincide with "Narsajuaq Arc" crust and have used a contour line to define the complicated shape of the "Narsajuaq Arc". We believe that their interpretation might be correct but it can not be drawn from the original magnetic profiles. Our interpretation does not address the question of continuity of the Narsuajaq arc from Cape Smith to Baffin Island because it would occur only west of the study area.

- One broad north trending band defined by a positive anomaly connects the Lac Lomier complex in Quebec to eastern Baffin Island.

- In both *Scott and St-Onge*'s [1998] and our interpretations, the Tasiuyak domain is defined by a wide band of strong magnetic lows extending northward under the western part of Frobisher Bay.

Figure 6.1: Generalized geology of the eastern Canadian Shield around the Bay of Ungava, modified after Wheeler et al., 1997. For simplicity, smaller formations were removed, and the Superior province is represented by one color only. The LITHOPROBE seismic profiles are shown as black lines. The two frames indicate the limits of the regional potential field maps (A), and of the detailed maps of Ungava Bay, Hudson Strait and surrounding land (B). BD: Burwell domain; CB: Cumberland batholith; dPB: de Pas batholith; LHG: Lake Harbour group; LLC: Lac Lomier complex; NA: Narsajuaq Arc; NQO: New Quebec orogen; TD: Tasiuyak domain; WCZ: western core zone.

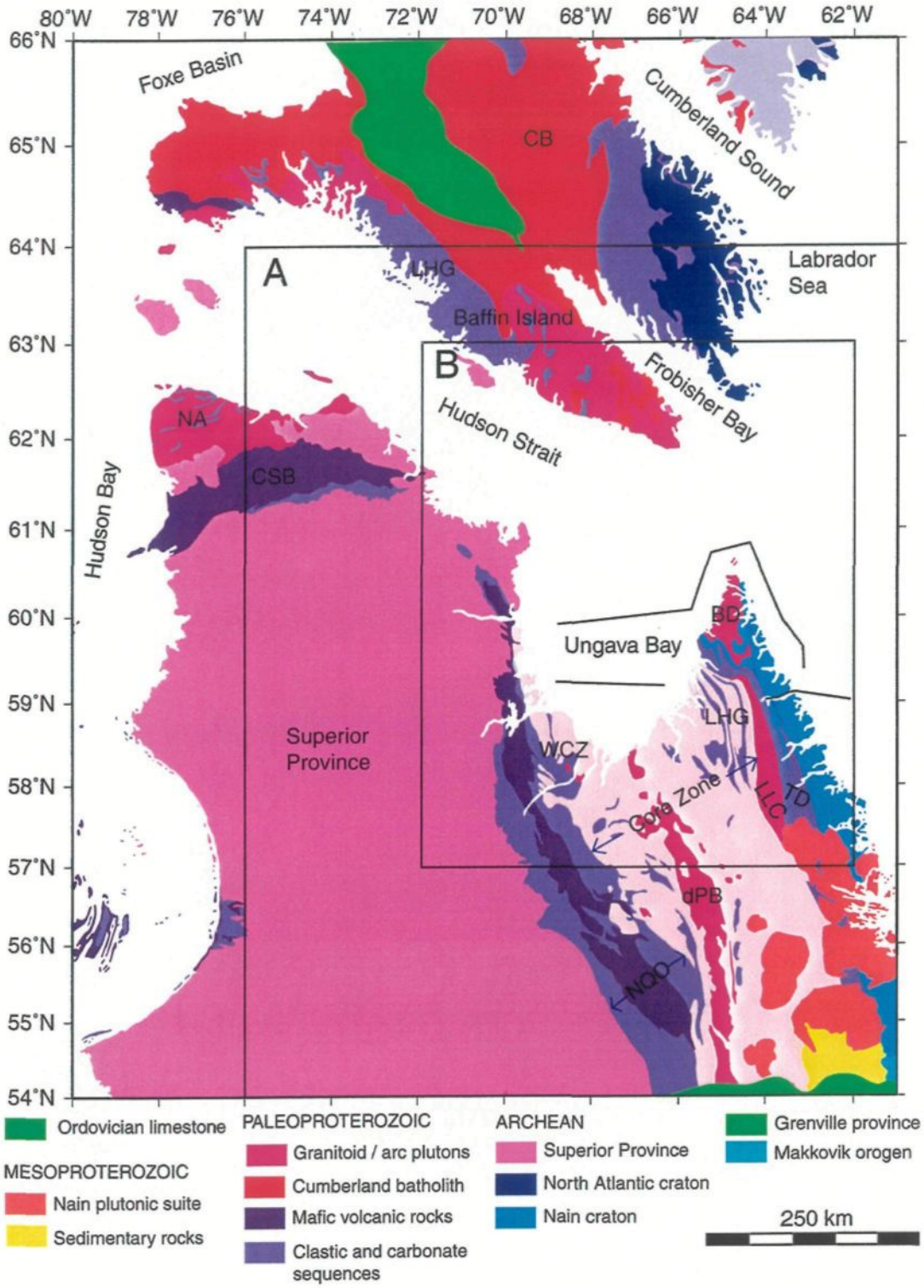
80°W
78°W
76°W
74°W
72°W
70°W
68°W
66°W
64°W
62°W
66°N
65°N
64°N
63°N
62°N
61°N
60°N
59°N
58°N
57°N
56°N
55°N
54°N
Foxe Basin
CB
Cumberland Sound
Labrador Sea
A
LHG
Baffin Island
B
Frobisher Bay
Hudson Strait
NA
CSB
Hudson Bay
Ungava Bay
BD
LHG
WCZ
Core Zone
LLC
TD
Superior Province
dPB
NQO
Ordovician limestone
MESOPROTEROZOIC
Nain plutonic suite
Sedimentary rocks
PALEOPROTEROZOIC
Granitoid / arc plutons
Cumberland batholith
Mafic volcanic rocks
Clastic and carbonate sequences
ARCHEAN
Superior Province
North Atlantic craton
Nain craton
Grenville province
Makkovik orogen
250 km

Figure 6.2: Total magnetic field map based on aeromagnetic and marine magnetic data. On the inset, the lines represent the ship tracks in the offshore areas; the region covered by aeromagnetic surveys is shown in grey. The data were high pass filtered to eliminate wavelengths shorter than 5 km and to retain all wavelengths longer than 10 km. The variable color scale was adjusted to better display geological features. Shading resulting from N210° illumination was superposed to better outline the continuity of some features.

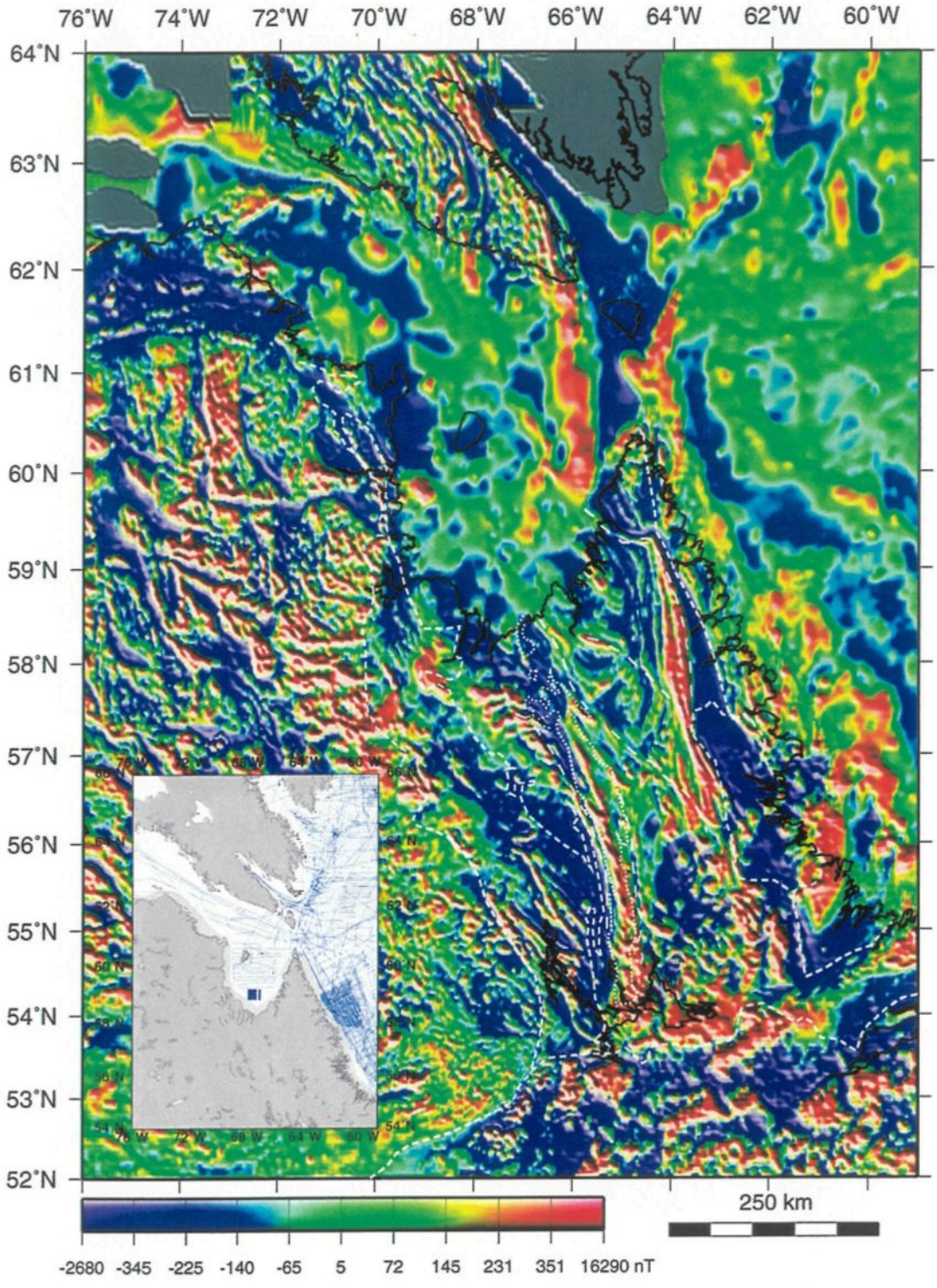
76°W
74°W
72°W
70°W
68°W
66°W
64°W
62°W
60°W
64°N
63°N
62°N
61°N
60°N
59°N
58°N
57°N
56°N
55°N
54°N
53°N
52°N
250 km
-2680 -345 -225 -140 -65 5 72 145 231 351 16290 nT

Figure 6.3: Composite map obtained by superimposing the shaded relief total magnetic field (illuminated from N210°) on the color coded gravity. The gravity map was obtained by combining Bouguer gravity on land with free-air gravity offshore. In the Bay of Ungava, the gravity is derived from satellite measurements of the geoid height. A variable color scaling was used to better display the main geological features. Several contacts are highlighted by the white lines. ASZ: Abloviak shear zone, FSZ: Falcoz shear zone; GRSZ: George River shear zone; LTF: Lac Turcotte fault; LTSZ: Lac Tudor shear zone; MBSZ: Moonbase shear zone; TO: Torngat orogen.

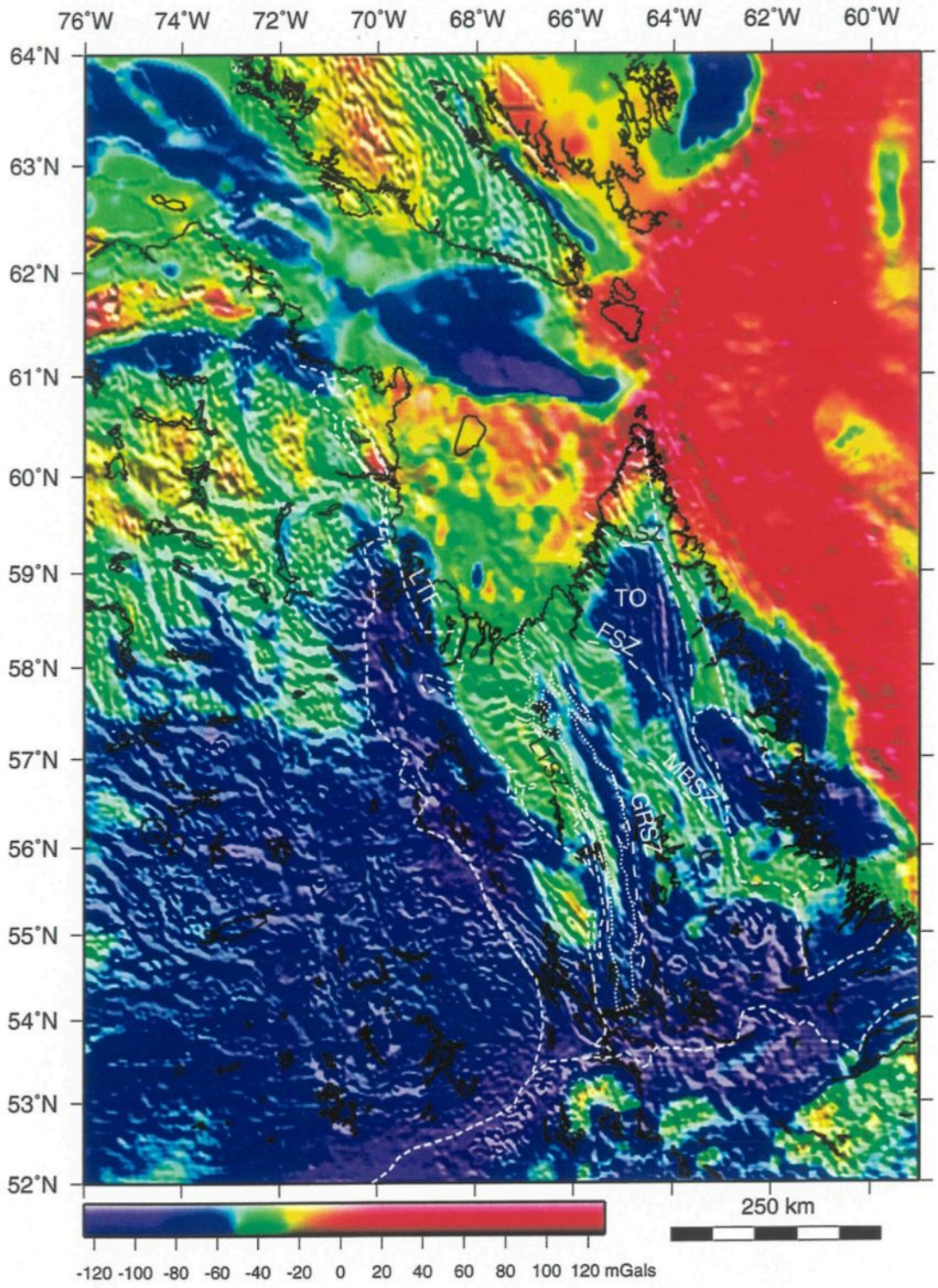
76°W
74°W
72°W
70°W
68°W
66°W
64°W
62°W
60°W
64°N
63°N
62°N
61°N
60°N
59°N
58°N
57°N
56°N
55°N
54°N
53°N
52°N
LTF
TO
FSZ
LSZ
MBSZ
GRSZ
250 km
-120 -100 -80 -60 -40 -20 0 20 40 60 80 100 120 mGals

Figure 6.4: Detailed magnetic map of the region around Ungava Bay and Hudson Strait. We have superimposed our interpretation of the geological boundaries, based on the magnetic anomalies as discontinuous lines. BD: Burwell domain; CB: Cumberland batholith; GRSZ: George River shear zone; LHG: Lake Harbour group; LLC: Lac Lomier complex; NA: Narsajuaq Arc; NQO: New Quebec orogen; TD: Tasiuyak domain; WCZ: western core zone.

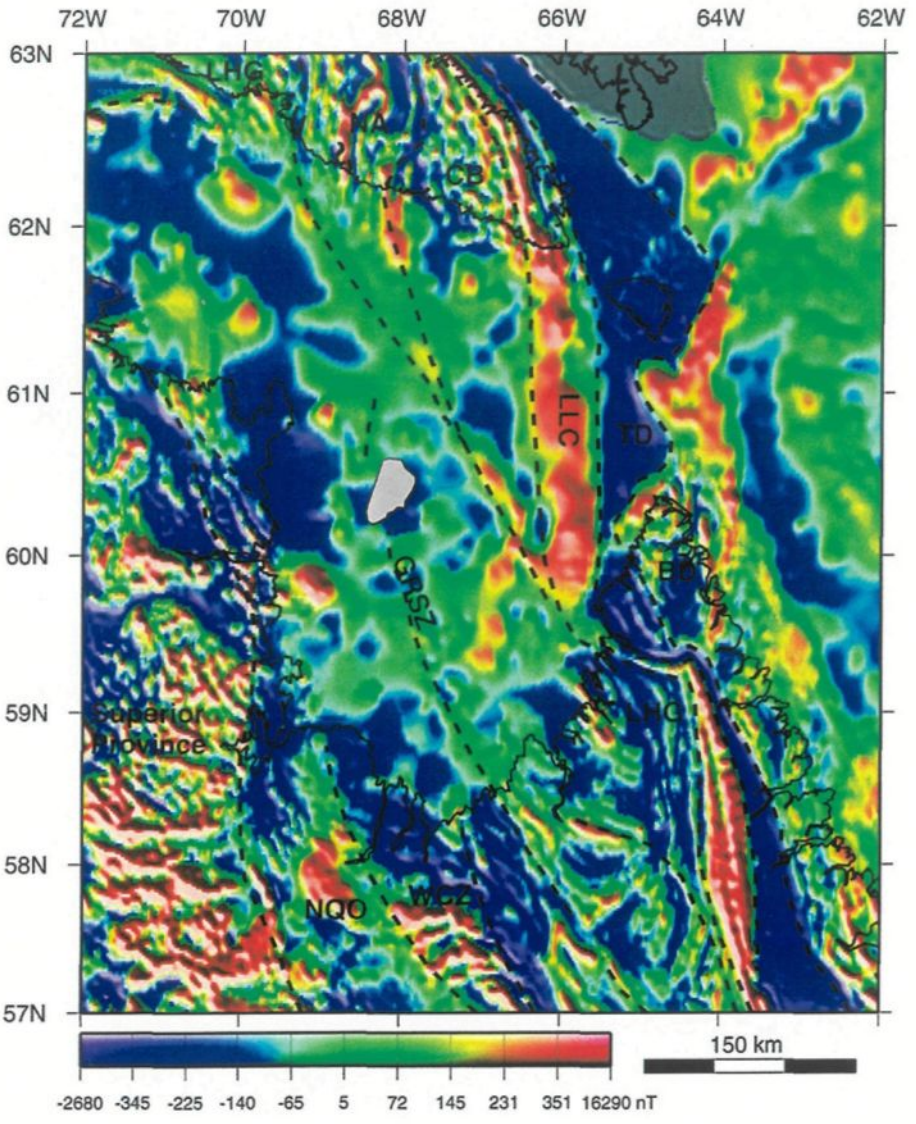
72W
70W
68W
66W
64W
62W
63N
62N
61N
60N
59N
58N
57N
LHC
CB
LLC
FD
GRSZ
BC
LHC
Superior
Province
NQO
WCSZ
150 km
-2680 -345 -225 -140 -65 5 72 145 231 351 16290 nT

Figure 6.5: Marine magnetic profiles over the Bay and the Strait. The positive anomalies are shown in dark grey and negative are in light grey. The interpreted contacts are displayed as discontinuous lines (see Fig. 6.4). BD: Burwell domain; CB: Cumberland batholith; GRSZ: George River shear zone; LLC: Lake Lomier complex; NA: Narsuajaq arc; TD: Tasiuyak domain.

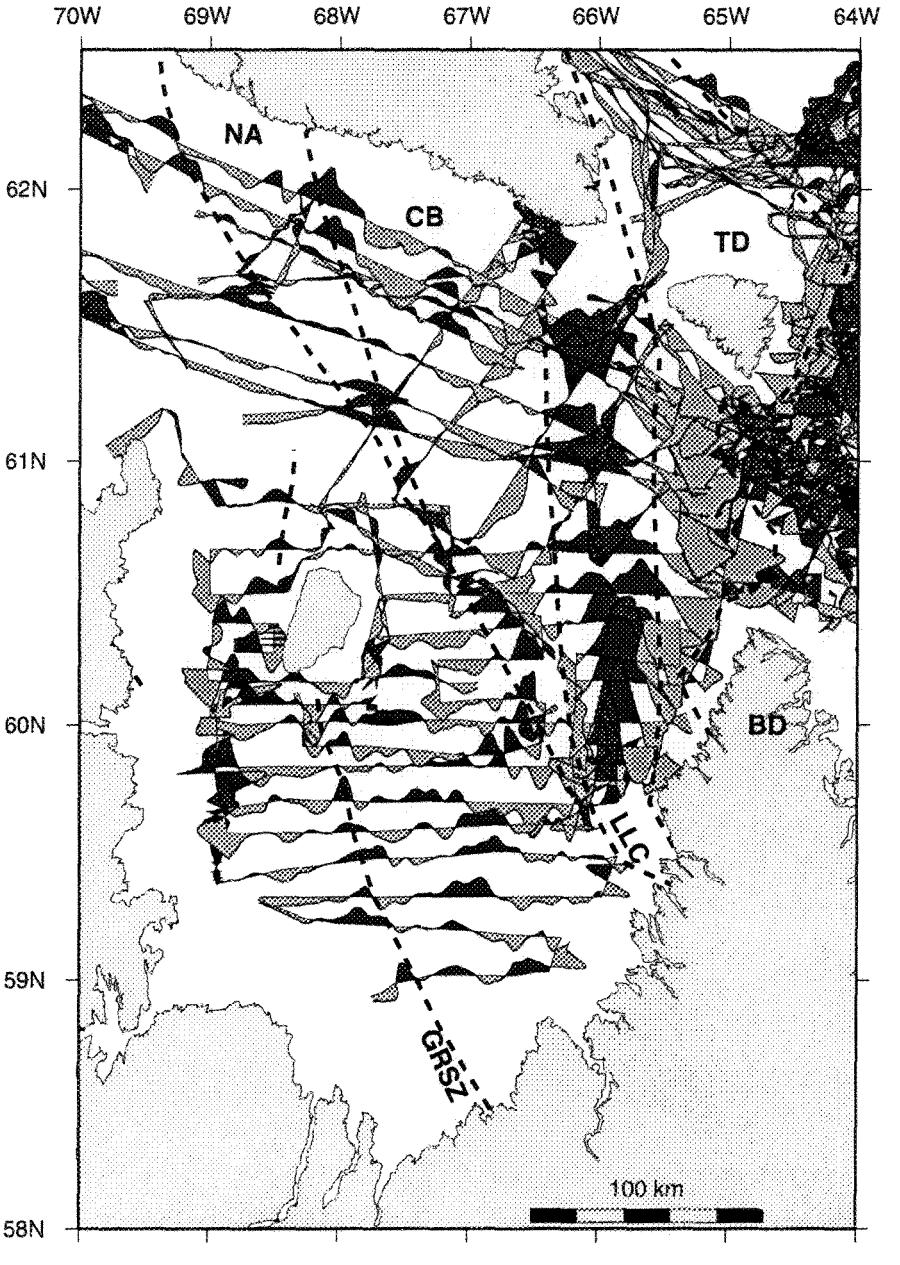
70W
69W
68W
67W
66W
65W
64W
62N
61N
60N
59N
58N
NA
CB
TD
BD
LLC
GRSZ
100 km

Figure 6.6: Detailed map of the vertical gravity gradient over the Ungava Bay and Hudson Strait regions. The interpreted contacts from the magnetics are displayed as discontinuous lines (see Fig. 6.4).The dotted lines are additional discontinuities that we have interpreted from the vertical gravity gradient. BD: Burwell domain; CB: Cumberland batholith; GRSZ: George River shear zone; LHG: Lake Harbour group; LLC: Lake Lomier complex; NA: Narsuajaq arc; NQO: New Quebec orogen; TD: Tasiuyak domain; WCZ: western core zone.

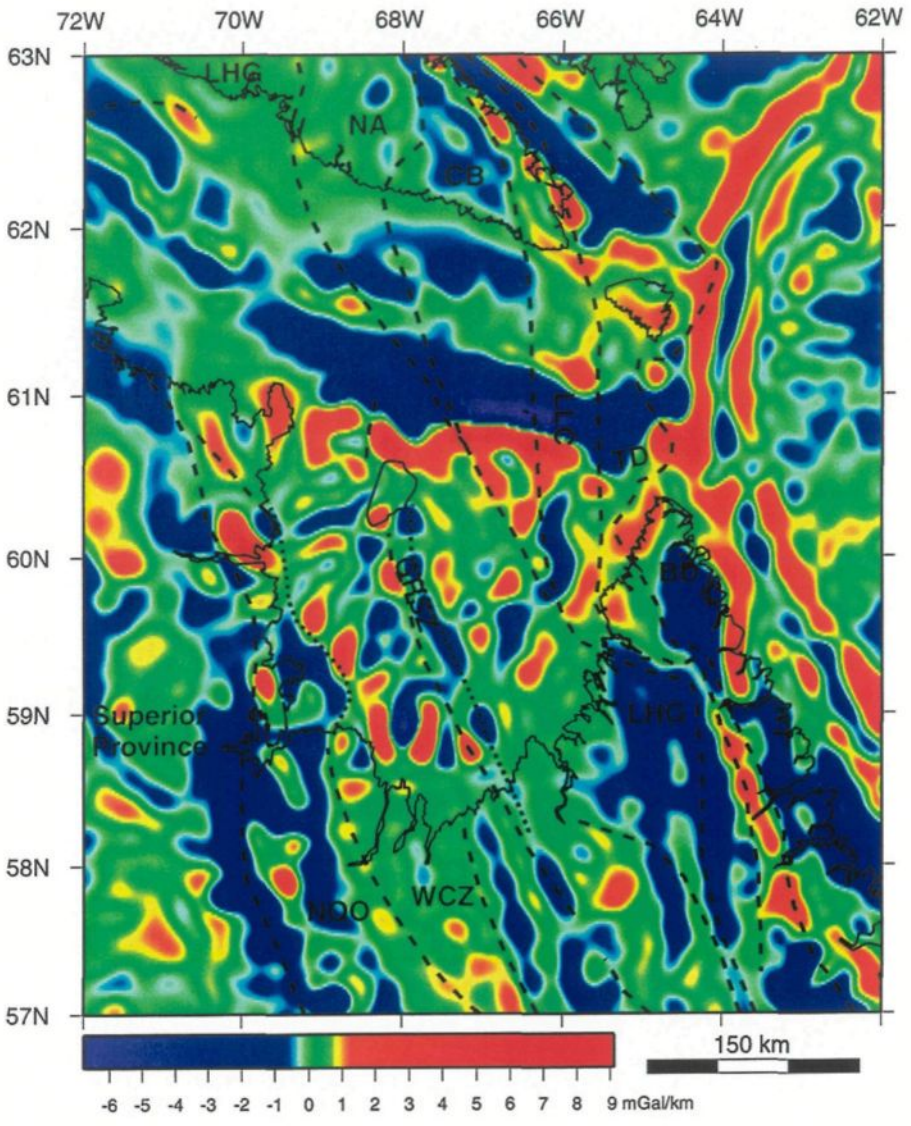
72W
70W
68W
66W
64W
62W
63N
62N
61N
60N
59N
58N
57N
LHG
NA
CB
D
Superior
Province
LHG
NQO
WCZ
150 km
-6 -5 -4 -3 -2 -1 0 1 2 3 4 5 6 7 8 9 mGal/km

Figure 6.7: Geological map with superposed shading of the relief of the total magnetic field on land and offshore. The thick black lines show our proposed interpretation of theboundaries in the Bay inferred from the potential field data. The thin white lines show the interpretation of *Scott and St-Onge* [1998]. The color coding for the geology is the same as in Fig 1.BD: Burwell domain; GRSZ: George River shear zone; LHG: Lake Harbour group; LLC: Lake Lomier complex; NA: Narsuajaq arc; NQO: New Quebec orogen; TD: Tasiuyak domain; WCZ: western core zone.

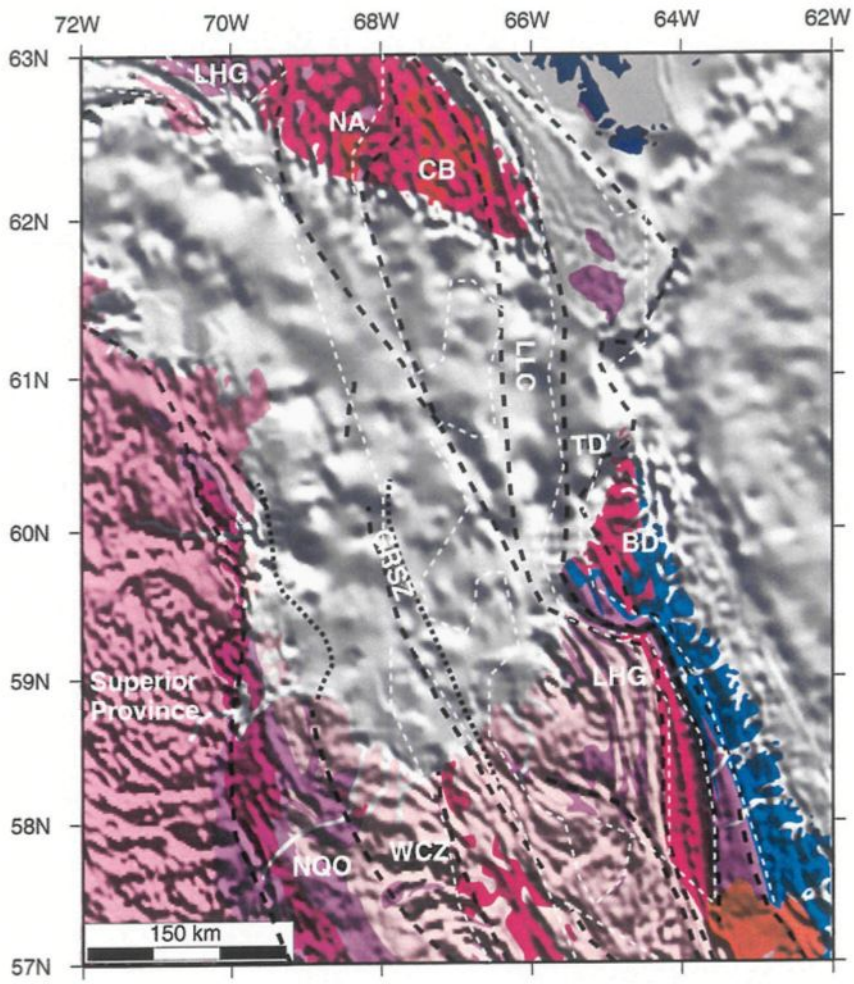
72W
70W
68W
66W
64W
62W
63N
62N
61N
60N
59N
58N
57N
LHG
NA
CB
LTC
TD
BD
ZSRSZ
LHG
Superior
Province
NQO
WCZ
150 km

General conclusions

This thesis has concerned the study of the Canadian shield at a broad scale. The mapping of geophysical data set gives some insights in the general architecture of the shield. We have focussed on three areas: the south-eastern Churchill province under the Ungava Bay, the Trans-Hudson orogen and the western Superior province beneath the sedimentary cover of central Canada. I hope that it will provide a better understanding of the tectonics combined with geochemistry and field indicators.

Interpretation of gravity and magnetic map have shown the complexity of the geology in the Ungava Bay area. Some structures extend from Quebec and Labrador across the Bay to Baffin Island, and others end inside the Bay. We have shown that a small portion presumably rifted from the Superior province is present in the core zone.

The study of elastic thickness in the eastern Canadian shield shows that it is as

rigid as the Central part [*Wang and Mareschal*, 1999]. The values of elastic thickness are similar to those obtained for other cratonic parts in the world. The variations in elastic thickness do not seem to be related to the thermal regime, however they may be related to the differences in the composition of the crust and/or to the presence of major faults (as suggested by *Burov et al.* [1998]). We have shown differences between provinces: the Grenville province has a rigidity more isotropic than the Superior province. The reason is not elucided yet, it may be due to the presence or not of major faults or shear zones. The explanation may be in the formation history of the two provinces.

In another chapter, potential field maps permit to look under the Phanerozoic sedimentary cover in Central Canada. We concluded that the pattern of the Superior subprovinces was truncated by Trans-Hudson orogen. The eastern tectonic features of this orogen extend at least to the U.S. border (the southern boundary of our maps), whereas the western structures end on the Medicine Hat craton to the south. We have not found any signature of the NACP conductivity anomaly on our maps, probably because the sources of this anomaly are not the same ones as those for the gravity and magnetic anomalies.

On a methodological point of view, this thesis shows the application of wavelet-based methods for potential fields data processing. Even if these methods are not illustrated extensively in the application part, their study was the major part of my work. Methods used by *Bergeron et al.* [1999] for seismic anomalies studies or the "worm mapping" of geophysical data of *Hornby et al.* [1999] were tried on different data sets. It gave pretty images, but the question was what does it mean or what kind of additional information arises compared to classical derivative images.

Fortunately other tests were more successful. The application of wavelet in the characterization of the elastic behavior of the lithosphere allows us to have a pretty good idea of the anisotropy of the elastic thickness. It allows us to obtain more local information than with the Fourier method. The problem is what "local information" means when we talk about the lithosphere elastic thickness. I am not sure that the localization brougth by the wavelet transform, as used in this thesis, is really usefull. I think that wavelets may rather be used to compute spectral estimation without the restriction of grid dimension: because the global wavelet spectrum is the (weighted) sum of local wavelet spectra, this allows us to choose the grid points we want to use.

The sources characterization method developed by *Moreau* [1995] has been used

successfully on high resolution magnetic data from Brazil (not presented in this thesis) and on regional gravity data set in Canada. I expect that the modification of the method proposed at the end of the chapter 2 will give better results. Because the procedure of depth estimation is not based on a trail and error process, it may be automatized more easily.

Bibliography

Alexandrescu, M., Gibert, D., Hulot, G., Le Moul, J.-L., Saracco, G., 1995. Detections of geomagnetic jerks using wavelet analysis. *Journal of Geophysical Research*, 100, B7: 12557-12572.

Arneodo, A., Argoul, F., Bacry, E., Elezgaray, J., Muzy, J.F., 1995. Ondelettes, multifractales et turbulence: de l'ADN aux croissances cristallines. *Diderot Editions, Arts et Sciences, Paris.*

Ashton, K.E., Lewry, J.F., 1994. Vergence of the Pelican Slide and Sturgeon-weir Shear Zone. *In* Proceedings, Trans-Hudson Orogen Transect Meeting, *Lithoprobe Report*, 38: 12-17.

Baird, D.J., Knapp, J.H., Steer, D.N., Walters, J.J., Brown, L.D, 1996. Crustal structure and evolution of the Trans-Hudson Orogen: Results from seismic reflection profiling. *Tectonics*, 15: 416-426.

Bechtel, T.D., Forsyth, D.W., Sharpton, V.L. and Grieve, R.A.F, 1990. Variations in effective elastic thickness of the North American lithosphere. *Nature*, 343: 636-638.

Bergeron, S.Y., Vincent, A.P., Yuen, D.A., Tranchant, B.J.S., Tchong, C., 1999. Viewing Seismic Velocity Anomalies with 3-D Continuous Gaussian Wavelets *Geophysical Research Letters*, 26(15): 2311-2314.

Bills, B.G., May, G.M., 1987. Lake Bonneville: Constraints on lithospheric thickness and upper mantle viscosity from isostatic upwarming of Bonneville, Provo and Gilbert stage shorelines. *Journal of Geophysical Research,* 92: 11493-11508.

Blakely, R.J., Simpson, R.W., 1986. Locating edges of source bodies from magnetic and gravity anomalies. *Geophysics*, 51: 1494-1498.

Burov, E.B., Diament, M., 1995. The effective elastic thickness (*Te*) of continental lithosphere: What does it really mean? *Journal of Geophysical Research*, 83: 5989-6004.

Card, K. D., Ciesielski, A., 1986. Subdivisions of the Superior Province of the Canadian Shield. *Geoscience Canada*, 13: 5-13.

Chandler, F. W., Schwarz, E.J., 1980. Tectonics of the Richmond Gulf area northern Quebec - A hypothesis. *Geological Survey of Canada, Ottawa, Current Research*, part C, Pap. 80-1C: 59-68.

Cordell, L., Grauch, V.J.S., 1985. Mapping basement magnetization zones from aeromagnetic data in the San Juan basin, New Mexico. in *Hinze, W. J., Ed., The Utility of Regional Gravity and Magnetic Anomaly maps*, 181-197.

Dallard, T., Spedding, G. R., 1993. 2-D wavelet transforms: generalisation of the

Hardy space and application to experimental studies. *European Journal of Mechanics, Fluids*, 12: 107-134.

Dorman, L.M., Lewis, B.T.R., 1970. Experimental isostasy, 1, theory of the determination of the earth's elastic response to concentrated load. *Journal of Geophysical Research*, 75(17): 3357-3365.

Emilia, D.A., 1973. Equivalent sources used as an analytic base for processing total magnetic field profiles, *Geophysics*, 38: 339-348.

Feininger, T., Ermanovics, I., 1994. Geophysical interpretation of the Torngat orogen along North River - Nutak transect, Labrador, *Canadian Journal of Earth Sciences*, 31: 722-727.

Forsyth, D.W., 1985. Subsurface loading and estimates of the flexural rigidity of continental lithosphere. *Journal of Geophysical Research*, 90(B14): 12,623-12,632.

Funck, T., Louden, K.E., 1998. Wide-angle seismic imaging of pristine Archean crust in the Nain Province, Labrador. *Canadian Journal of Earth Sciences*, 35(6): 672-685.

Funck T., Louden, K.E., 1999. Wide-angle seismic transect across the Torngat Orogen, northern Labrador: Evidence for a Proterozoic crustal root, *Journal of Geophysical Research*, 104: 7463-7480.

Funck, T., Louden, K.E., Wardle, R.J., Hall, J., Hobro, J.W., Salisbury, M.H.,

Muzzatti, A., 2000. Three-dimensional structure of the Torngat orogen (NE Canada) from active seismic tomography. *Journal of Geophysical Research*, 105: 23403-23420.

Gabor, D., 1946. Theory of Communication *Journal of the Institution of Electronical Engineering (London)*,Vol. 93(III) , 26: 429-457.

Gibb, R.A., Thomas, M.D., 1976. Gravity signature of fossil plate boundaries in the Canadian Shield. *Nature*, 262: 199-200.

Gibb, R.A., Walcott, R.I., 1971. A Precambrian suture in the Canadian Shield. *Earth and Planetary Science Letter*, 10: 417-422.

Girard, R., 1990. Les cisaillements latéraux dans l'arrière pays des orogènes du Nouveau-Québec et de Torngat: une revue. *Geosciences Canada*, 17: 301-304.

Grossmann, A., Morlet, J., 1984. Decomposition of Hardy functions into square integrable wavelet of constant shape. *SIAM J. Math. Anal*, 15(4): 723-739.

Hagelberg, C. R., Gamage,N.K.K., 1994. Applications of structure preserving wavelet decompositions to intermittent turbulence: a case study. *In* Foufoula-Georgiou, E., and P. Kumar, eds. *Wavelets in Geophysics. Academic Press, New York*, 45-80.

Hall, J., Wardle, R.J., Gower, C.F., Kerr, A., Keen, C.E., Caroll, P., 1995. Proterozoic orogens of the northeastern Canadian Shield: New information from the Lithoprobe ECSOOT crustal reflection seismic survey. *Canadian Journal*

of Earth Sciences, 32: 1119-1131.

Hanmer, S., Parrish, R., Williams, M., Kopf, C., 1994. Striding-Athabasca mylonite zone: Complex Archean deep-crustal deformation in the East Athabasca mylonite triangle, northern Saskatchewan, *Canadian Journal of Earth Sciences*, 31: 1287-1300.

Hartley, R., Watts, A.B., Fairhead J.D., 1996. Isostasy of Africa. *Earth and Planetary Science Letters*, 137: 1-18.

Hocq, M., Verpaelst, P., Chartran, F., Brisebois, D., Clark, T., Lamothe, D., Brun, J., Martineau, G., 1994. Gologie du Qubec. *Les Publications du Qubec. Gouvernement du Qubec*, M 94-01, 154 pp.

Hoffman, P.F., 1981. Autopsie of Athapuscow Aulacogen: a failed arm affected by tree collisions. *In* Campbell, F.H.A., ed., Proterozoic Basins of Canada: Geological Survey of Canada, Paper 81-10, p. 97-102.

Hoffman, P.F., 1985. Is the Cape Smith Belt (northern Québec) a klippe?. *Canadian Journal of Earth Sciences*, 22: 1361-1369.

Hoffman, P.F., 1988. United Plates of America, The birth of a craton: Early Proterozoic assembly and growth of Laurentia. *Annual Review of Earth and Planetary Sciences*, 16: 543-603.

Hoffman, P.F., 1990. Dynamics of the tectonic assembly of northeast Laurentia in geon 18 (1.9-1.8Ga). *Geoscience Canada*, 17: 222-226.

Holschneider, M., 1995. Wavelets: an analysis tool, *Oxford: Clarendon Press*, 423 pp.

Hornby, P., Boschetti, F., Horowitz, F.G., 1999. Analysis of Potential Field Data in the Wavelet Domain. *Geophysical Journal International*, 137: 175-196.

Isnard, H., Parent, M., Bardoux, M., David, J., Gariépy, C., Stevenson, R.K., 1998. U-Pb, Sm-Nd and Pb-Pb isotope geochimistry of the high-grade gneiss assemblages along the southern shore of Ungava Bay, *In* Eastern Canadian Shield Onshore-Offshore Transect (ECSOOT), Transect Meeting (May 4-5, 1998), *Edited by* R.J. Wardle and J. Hall, The University of British Columbia, LITHOPROBE Secretariat, Report **68:** 67-77.

Jackson, G.D., Taylor, F.C., 1972. Correlation of major Aphebian rock units in the northeastern Canadian Shield. *Canadian Journal of Earth Sciences*, 9: 1650-1669.

James, D.T., Dunning, G., 2000. U-Pb geochronological constraints for Paleoproterozoic evolution of the core zone, southeastern Churchill Province, northeastern Laurentia. *Precambrian Research*, 10: 31-54.

James, D.T., Connelly, J.N., Wasteneys, H.A., Kilfoil, G.J., 1996. Paleoproterozoic lithotectonic divisions of the southeastern Churchill Province, western Labrador. *Canadian Journal of Earth Sciences*, 33: 216-230.

James, D.T., Connelly, J.N., Scott, D., 1998. Core zone of the southeastern Churchill province, western Labrador to Ungava Bay and beyond: the meat of the prob-

lem. *In* Eastern Canadian Shield Onshore-Offshore Transect (ECSOOT), Transect Meeting (May 4-5, 1998), *Edited by* R.J. Wardle and J. Hall, The University of British Columbia, LITHOPROBE Secretariat, Report 68: 92-100.

Jones, A.G., Savage, P.J., 1986. North American Central Plains Conductivity Anomaly Goes East, *Geophysical Research Letters*, 13: 685-688.

Kane, M.F., Godson, R.H., 1989. A crust/mantle structural framework of the conterminous United States based on gravity and magnetic trends. *In* Geophysical framework of the United States, *Edited by* L.C. Pakiser and W.M. Mooney. Geological Society of America. Boulder (CO), pp. 383-403.

Karner, G.D., Watts, A.B., 1983. Gravity anamalies and flexure of the lithosphere at mountain ranges. *Journal of Geophysical Research*, 88(B12): 10449-10477.

Karner, G.D., Watts, A.B., 1982. On isostasy at Atlantic-type continental margins. *Journal of Geophysical Research*, 87(B4):2923-2948.

Kearey, P., 1976. A regional structural model of the Labrador trough, northern Québec, from gravity studies and its relevance to continent collision in the Precambrian. *Earth and Planetary Science Letter*, 28: 371-378.

Kumar, P., Foufoula-Georgiou, E., 1997. Wavelet analysis for geophysical applications. *Review of Geophysics*, 35(4): 385-412.

Lewis, B.T.R, Dorman, L.M., 1970. Experimental isostasy, 2, an isostatic model for the U.S.A derived from gravity and topographic data. *Journal of Geophysical*

Research, 75(17): 3367-3386.

Lewry, J.F., Sibbald T.I.I., 1980. Thermotectonic evolution of the Churchill province in northern Saskatchewan, *Tectonophysics*, 68: 45-82.

Lewry, J.F., Collerson, K.D., 1990. The Trans-Hudson Orogen: Extent, subdivision, and problems, *in* J.F. Lewry, and M.R. Stauffer (eds.), *The Early Proterozoic Trans-Hudson Orogen of North America, Geological Association of Canada Special Paper*, 37:1-14.

Lewry, J. F., Stauffer M.R., 1990. The Early Proterozoic Trans-Hudson Orogen of North America, *Geological Association of Canada,* Special Paper 37.

Lim, J.S., Malik, N.A., 1981. A new algorithm for two-dimensional maximum entropy power spectrum estimation. *IEEE Trans. Acoust. Speech Signal Process.*, 29: 401-413.

Little, S.A., 1994. Wavelet Analysis of Seafloor Bathymetry: An Example. In *Wavelets in Geophysics* E. Foufoula-Georgiou and P. Kumar (EDS), Academic Press, San Diego, Calif., 167-182.

Liu, P.C., 1994. Wavelet Spectrum Analysis and Ocean Wind Waves. In *Wavelets in Geophysics* E. Foufoula-Georgiou and P. Kumar (EDS), Academic Press, San Diego, Calif., 151-166.

Lowry, A.R., Smith, R.B., 1994. Flexural rigidity of the Basin and Range-Colorado Plateau-Rocky Mountain transition from coherence analysis of gravity and to-

pography. *Journal of Geophysical Research*, 99(B10): 20123-20140.

Lucas, S. B., Green, A. G., Hajnal, Z., White, D. J., Lewry, J. F., Ashton, K. E., Weber, W., Clowes, R. M., 1993. Deep seismic profile a Proterozoic collision zone. *Nature*, 363: 339-342.

Lucas, S.B., White, D., Hajnal, Z., Lewry, J., Green, A., Clowes, R., Zwanzig, H., Ashton, K., Schledewitz, D., Stauffer, M., Norman, A., Williams, P., Spence, G., 1994. Three-dimensional collisional structure of the Trans-Hudson Orogen, Canada. *Tectonophysics*, 232: 161-178.

Lyon-Caen, H., Molnar, P., 1983. Constraints on the structure of the Himalaya from an analysis of gravity anomalies and a flexural model of the lithosphere. *Journal of Geophysical Research*, 88: 8171-8192.

Macario, A., Malinverno, A., Haxby, W.F., 1995. On th robustness of elastic thickness estimates obtained using the coherence method. *Journal of Geophysical Research*, 100(B8): 15163-15172.

Mallat, S., Zhong, S., 1992. Characterisation of Signals from Multiscale Edges. *IEEE Transactions On Pattern Analysis And Machine Intelligence*, 14(7):710-732.

Mareschal, J.C., DallaColleta, G., Clevenot, I., Goulet, N., 1990. Gravity profile and crustal structure across the New Québec Orogen. *Geosciences Canada*, 17: 250-254.

Marson, I., Klingele, E.E., 1993. Advantages of using the vertical gradient of gravity

for 3-D interpretation. *Geophysics*, 58: 1588-1595.

Martelet, G., Sailhac, P., Moreau, F., Diament M., 2001. Characterization of geological boundaries using 1D wavelet transform on gravity data: Theory and application to the Himalayas. *Geophysics*, 66(4): 1116-1129.

Martelin, J., Chenevoy, M., Bélanger, M., 1998. Le batholite de de Pas, Nouveau-Québec: infrastructure composite d'un arc magmatique. *Canadian Journal of Earth Sciences*, 35: 1-15.

McKenzie, D., Bowin, C., 1976. The relationship between bathymetry and gravity in the Atlantic ocean. *Journal of Geophysical Research*, 81: 1903-1915.

McKenzie, D., Fairhead, D., 1997. Estimates of the effective elastic thickness of the continental lithosphere from Bouguer and free air gravity anomalies. *Journal of Geophysical Research*, 102(B12): 27523-27552.

McNutt, M.K., Parker, G.D., 1978. Isostasy in Australia and the evolution of the compensation mechanism. *Science*, 199: 773-775.

Meyer Y., 1993 Wavelets: Algorithms and Applications, *SIAM Press, Philadelphia.*

Meyer, M. T., Bickford, M.E., Lewry, J.F., 1992. The Wathaman batholith: an Early Proterozoic continental arc in the Trans-Hudson orogenic belt, Canada. *Geological Society of America Bulletin*, 104: 1073-1085.

Meyer, Y., Roques, S., 1993. Progress in Wavelet Analysis and Applications. *Editions*

Forntières, Gif-sur-Yvette.

Moorhead, J., Perrault, S., Berclaz, A., Sharma, K.N.M., Beaumier, M., Cadieux, A.-M., 2000. Kimberlites et diamants dans le Nord du Qubec. *Ministre des Ressources naturelles, Qubec*,PRO 2000-05, 9 pp.

Moreau, F., 1995. Méthodes de traitement de donnés géophysiques par transformée en ondelettes. *Ph.D. Thesis, Rennes I,* 1521: 177pp

Moreau, F., Gilbert, D., Holschneider, M., Saracco, G., 1997. Wavelet analysis of potential fields. *Inverse Problems*, 13: 165-178.

Moreau, F., Gilbert, D., Holschneider, M., Saracco, G., 1999. Identification of sources of potential fiels with the continuous wavelet transform: Basic theory. *Journal of Geophysical Research*, 104(B3): 5003-5013.

Morlet, J., Arens, G., Fourgeau, I., Giard, D., 1982a. Wave propagation and sampling theory, 1, Complex signal and scattering in multilayered media. *Geophysics*, 47(2):203-221.

Morlet, J., Arens, G., Fourgeau, I., Giard, D., 1982b. Wave propagation and sampling theory, 2, Sampling theory and complex waves. *Geophysics*, 47(2):222-236.

Murenzi, R., 1990. Ondelettes multidimensionnelles et application à l'analyse d'images, PhD thesis, Université catholique de Louvain, Belgique.

Nabighian, M. N., 1972. The analytic signal of two-dimensional magnetic bodies

with polygonal cross-section: its properties and use for automated anomaly interpretation. *Geophysics*, 37(3): 507-517.

Naudy, H., 1971. Automatic determination of depth on aeromagnetic profile, *Geophysics*, 36: 717-722.

Nelson, K. D., Baird, D. J., Waters, J. J., Hauck, M., Brown, L. D., Oliver, J. E., Ahern, J. L., Hajnal, Z., Jones, A. G., Sloss, L. L., 1993. Trans-Hudson orogen and Williston basin in Montana and North Dakota: a new COCORP deep-profiling results. *Geology*, 21: 447-450.

Perrault, S., Hynes, A., 1990. Tectonic evolution of the Kuujjuaq terrane, New Québec Orogen. *Geosciences Canada*, 17: 238-241.

Pilkington, M., 1991. Mapping elastic lithospheric thickness variations in Canada. *Tectonophysics*, 190: 283-297.

Reid, A.B., Allsop, J.M., Granser, H., Millett, A.J., Somerton, I.W., 1990. Magnetic interpretation in three dimensions using Euler deconvolution, *Geophysics*, 55: 80-91.

Roest W.R., Srivastava, S.P., 1989. Sea floor spreading in the Labrador sea: a new reconstruction. *Geology*, 17: 1000-1003.

Royden, L.H., Karner, G.D., 1984. Flexure of the lithosphere beneath the Appennine and the Carpathian foredeep: Evidence for an insufficient topographic load. *AAPG Bulletin*, 68: 704-712.

Sailhac, P., Galdeano, A., Gilbert, D., Moreau, F., Delor, C., 2000. Identification of sources of potential fields with the continuous wavelet transform: Complex wavelets and application to aeromagnetic profiles in French Guiana. *Journal of Geophysical Research*, 105(B8): 19,455-19,475.

Scott, D.J., 1997. Geology, U-Pb, and Pb-Pb geochronology of the Lake Harbour area, southern Baffin Island:implications for the Paleoproterozoic tectonic evolution of the northern Laurentia. *Canadian Journal of Earth Sciences*, 34: 140-155.

Scott, D.J., St-Onge, M.R., 1998. PaleoProterozoic assembly of northeast laurentia revisited: a model based on southward extrapolation of Ungava-Baffin crustal architecture. *In* Eastern Canadian Shield Onshore-Offshore Transect (ECSOOT), Transect Meeting (May 4-5, 1998), *Edited by* R.J. Wardle and J. Hall, The University of British Columbia, LITHOPROBE Secretariat, Report 68: 134-149.

Séguin, M.K., Goulet, N., 1990. Gravimetric transect of eastern Ungava Bay, northern Torngat orogen. *Geosciences Canada*, 17: 273-276.

Sharpton, V.L., Grieve, R.A.F., Thomas, M.D., Halpenny, J.F., 1987. Horizontal gravity gradient: an aid to the definition of crustal structure in North America. *Geophysical Research Letters*, 8: 808-811.

Simons, M., Hager, B., 1997. Localization of the Gravity Field and the Signature of Glacial Rebound. *Nature*, 390: 500-504.

Simons, F.J., Zuber, M.T, Korenaga, J., 2000. Isostatic response of the Australian lithosphere: Estimation of effective elastic thickness and anisotropy using multitaper spectral analysis. *Journal of Geophysical Research*, 105(B8): 19163-19184.

Smith, W.H.F., Sandwell, D.T., 1995. Marine gravity field from declassified Geosat and ERS-1 altimetry. *EOS, Transactions, American Geophysical Union,* 76(46), Fall Meet. Suppl., p. 156.

Smith, W.H.F., Wessel, P., 1990. Gridding with continuous curvature splines in tension. *Geophysics*, 55: 293-305.

Smith, W.H.F., Sandwell, D.T., 1997. Global sea floor topography from satellite altimetry and ship depth soundings. *Science*, 277: 1956-1962.

Stark, C.P., Stewart, J., 1997. Mapping lithospheric strengh and loading using wavelet transform admittance and coherence. *EOS, Transactions, American Geophysical Union,*, 78(46), Fall Meet. Suppl., U41A-8.

Stauffer, M.R., 1984. Manikewan: an Early Proterozoic ocean in central Canada, its igneous history and orogenic closure. *Precambrian Research*, 25: 257-281.

Stauffer, M. R., Lewry, J.F., 1993. The Needle Falls shear zone: its movement history geodynamic significance in the Trans-Hudson Orogen. *Canadian Journal of Earth Sciences*, 30: 1338-1354.

Stewart, J., Watts, A.B., 1997. Gravity anomalies and spatial variations of flexural

rigidity at mountains ranges. *Journal of Geophysical Research*, 102(B3): 5327-5352.

St-Onge, M.R., Lucas, S.B., Parrish, R.R., 1992. Terrane accretion in the internal zone of the Ungava orogen, northern Québec. Part 1: Tectonostratigraphic assemblages and their tectonic implications. *Canadian Journal of Earth Sciences*, 29: 746-764.

St-Onge, M.R., Scott, D.J., Lucas, S.B., 2000. Early partitioning of Quebec: Micro continent formation in the Paleoproterozoic. *Geology*, 28: 323-326

Tanner, J.G., 1967. An automated method of gravity interpretation. *Geophysical Journal of the Royal Astronomical Society*, 13: 339-347.

Telford, W.M., Geldart, L.P., Sheriff, R.E., 1990. *Applied Geophysics, 2nd ed., Cambridge University Press.*

Telmat, H., Mareschal, J.-C., Gariépy, C., 1999. The gravity field over the Ungava Bay region from the satellite altimetry and new land-based data: implications for the geology of the area. *Canadian Journal of Earth Sciences*, 36: 75-89.

Telmat, H., Mareschal, J.-C., 1996. Gravity anomaly maps of Ungava Bay from satellite altimetry and new Bouguer data. *In* Eastern Canadian Shield Onshore-Offshore Transect (ECSOOT), Transect Meeting (March 14-15 1996), *Edited by* R.J. Wardle and J. Hall, The University of British Columbia, LITHOPROBE Secretariat, 57: 204-211.

Thériault, R.J., 1998. Nd and Pb isotopic and geochemical framework of paleoproterozoic southern Baffin Island, and comparisons with other segments of the eastern Trans-Hudson orogen, *In* Eastern Canadian Shield Onshore-Offshore Transect (ECSOOT), Transect Meeting (May 4-5, 1998), *Edited by* R.J. Wardle and J. Hall, The University of British Columbia, LITHOPROBE Secretariat, 68: 170-187.

Thomas, M.D., Gibb, R.A., 1977. Gravity anomalies and deep structure of the Cape Smith foldbelt, northern Ungava, Québec. *Geology*, 5: 169-172.

Thomas, M.D., Kearey, P., 1980. Gravity anomalies, block faulting and Andean type tectonism in the eastern Churchill province. *Nature*, 282: 61-63.

Thompson, D.T., 1982. EULDPH: A new technique for making computer-assisted depth estimates from magnetic data. *Geophysics*, 47(1): 31-37.

Torrence, C., Compo, G.P., 1998. A practical guide to wavelet analysis. *Bulletin of the American Meteorological Society*, 79: 61-78.

Torrence, C., Webster, P.J., 1999. Interdecadal changes in the ENSO-monsoon system. *J. Climate*, 12: 2679-2690.

van Staal, C.R., Dewey, J.F., Mac Niocaill, C., McKerrow, W.S., 1998. The Cambrian-Silurian tectonic evolution of the Northern Appalachians and British Caledonides; history of a complex, west and southwest Pacific-type segment of Iapetus. *In* Lyell; the past is the key to the present, *Edited by* D.J. Blundell and A.C. Scott, Geological Society Special Publications, 143: 199-242.

Verhoef J., Roest W.R., Macnab R., Arkani-Hamed, J., 1996. Magnetic anomalies of the Arctic and North Atlantic Oceans and Adjacent landmasses. CD-ROM and Report, GSC Open File 3215a/b.

Walcott, R.I., 1970. Flexural rigidity, thickness and viscosity of the lithosphere. *Journal of Geophysical Research*, 75: 3941-3954.

Wang, Y., Mareschal, J.-C., 1999. Elastic thickness of the lithosphere in the central Canadian shield. *Geophysical Research Letter*, 26: 3033-3036.

Wardle, R.J., Bailey, D.G., 1981. Early Proterozoic sequences in Labrador. *In* Proterozoic basins of Canada. *Edited by* F.H.A. Campbell. Geological Survey of Canada Paper 81-10. 331-359.

Wardle, R.J., Van Kranendonk, M.J., 1996. The Paleoproterozoic southeastern Churchill Province of Labrador-Québec, Canada: Orogenic development as a consequence of oblique collision and indentation. *In* Precambrian Crustal Evolution in the North Atlantic Region, *Edited by* T.S. Brewer, Special Publications Geological Society London, 112: 137-153.

Watts, A.B., 1978. An analysis of isostasy in the world's oceans, 1, Hawaiian-Emperor Seamount Chain. *Journal of Geophysical Research*, 83: 5989-6004.

Watts, A.B., Lamb, S.H., Fairhead, J.D., Dewey, J.F., 1995. Lithospheric flexure and bending of the Central Andes. *Earth and Planetary Science Letters*, 134: 9-21.

Welch, P.D., 1967. The use of fast Fourier transform for the estimation of power spectra: A method based on time averaging over short, modified periodograms. *IEEE Transactions on Audio and Electroacoustics*, 15(2): 70-73.

Wessel, P., Smith, W.H.F., 1995. The Generic Mapping Tools (GMT) version 3.3.2. Technical Reference & Cookbook, SOEST/NOAA. University of Hawaii, Mauoa.

Wheeler, J.O., Hoffman, P.F., Card, K.D., Davidson, A., Sanford, B.V., Okulitch, A.V., Roest, W.R., 1996. Geological Map of Canada, Map 1860A. Geological Survey of Canada, 1:5 000 000.

Zuber, M.T., Bechtel, T.D., Forsyth, D.W., 1989. Effective elastic thickness of the lithosphere and mechanisms of isostatic compensation in Australia. *Journal of Geophysical Research*, 94: 9353-9367.